University of Alberta

PDE Backstepping Boundary Observer Design with Application to Thermal Management of PCR Process in Lab-on-a-Chip Devices

by

Reza Banaei Khosroushahi

A thesis submitted to the Faculty of Graduate Studies and Research
in partial fulfillment of the requirements for the degree of

Doctor of Philosophy
in
Control Systems

Department of Electrical and Computer Engineering

© Reza Banaei Khosroushahi
Fall 2013
Edmonton, Alberta

Permission is hereby granted to the University of Alberta Libraries to reproduce single copies of this thesis and to lend or sell such copies for private, scholarly or scientific research purposes only. Where the thesis is converted to, or otherwise made available in digital form, the University of Alberta will advise potential users of the thesis of these terms.

The author reserves all other publication and other rights in association with the copyright in the thesis and, except as herein before provided, neither the thesis nor any substantial portion thereof may be printed or otherwise reproduced in any material form whatsoever without the author's prior written permission.

This work is dedicated to my wife, Nilufar, and my parents
for their endless love, support and encouragement

Abstract

In the past two decades, the idea of Lab-on-a-Chip (LOC) devices has received a growing attention from researchers. A Lab-on-a-Chip device can be thought of as a miniaturized biological microchip that integrates several functionalities such as sample pre-treatment, sample transportation, mixing, reaction, separation and detection. Among the important functionalities that have been successfully integrated into a Lab-on-a-Chip device is the Polymerase chain reaction (PCR) process which enables rapid and inexpensive genetic analysis. PCR process relies on a thermal cycling process of repeated heating and cooling to replicate the DNA to a sufficient amount for detection and analysis. However, the PCR process requires precise measurement and control of the reaction temperature that is a challenging problem especially in the miniaturized LOC environment. The challenges associated with the thermal control problem of a PCR process in the LOC environment fall into two categories: first, there is no direct measurement of the temperature inside the reaction chamber and second, the heat distribution equation governing the thermal dynamics inside the microchip naturally leads the modeling and control of the microchip into the distributed parameter systems framework.

This thesis deals with the estimation of the temperature inside the PCR-LOC microchip. Our goal in this thesis has two folds: first to contribute to the backstepping theory for the PDE systems both in the observer design and controller design stages, and second to use this theory for our application, PCR-LOC microchip. PDE Backstepping boundary observer design and its successful implementation involve several challenges, including:

- Solving the PDE equation for the kernel function of the integral transformation in the PDE backstepping design and all of the numerical issues that come along.

- Simulation aspects of the coupled PDE system composed of the PDE observer and the original PDE system.

- Verification aspects, i.e. how to ensure that calibration is correct and the PDE observer actually presents the temperature inside the chamber.

This thesis presents a number of innovative approaches to exclusively deal with each of the aforementioned challenges. The successful implementation of the designed observer and a previously designed controller is also presented.

Acknowledgements

First and foremost, I would like to express my sincere gratitude to my supervisor Dr. Horacio J. Marquez for providing me the opportunity to work on this interesting project, opening my eyes to countless aspects of engineering and science. His support, advices and encouragement has given me the freedom to explore this research field and the opportunity to think independently in my research field. I also thank my PhD committee members, Dr. Qing Zhao and Dr. Mahdi Tavakoli, for their valuable suggestions to improve the contents and presentation of this thesis. My appreciation as well to Dr. Stevan Dubljevic, Dr. Nariman Sepehri and Dr. Vien Van for their constructive suggestions and comments.

I appreciate the financial support of the department of the electrical and computer engineering at the University of Alberta and the Natural Sciences and Engineering Research Council of Canada (NSERC) that made this doctoral program possible. I would like to thank Jose Martinez-Quijada, Somayyeh Poshtiban, Behnam Allahverdi and Dr. Govind Kaigala for their collaboration and occasional discussions, which provided helpful comments and feedback for my research.

Finally, I acknowledge the grace of God and the love, support and encouragement of my wife, Nilufar for seeing me through this endeavour.

Reza Banaei Khosroushahi

Edmonton, AB

September, 2013

Contents

List of Tables

List of Figures

List of Acronyms

DNA	Deoxyribonucleic acid
LOC	Lab-on-a-Chip
PCR	Polymerase chain reaction
AML	Applied Miniaturization Laboratory
CE	capillary electrophoresis
PDMS	Poly-di-methyl-siloxane
Pt	Platinum
TLC	Thermochromic liquid crystal
ODE	Ordinary differential equation
PDE	Partial differential equation
MPC	Model predictive control
LTI	Linear time invariant
MHD	Magnetohydrodynamic
ADC	Analog to digital converter
DAQ	Digital to analog converter
CCD	Charge-Coupled Device
RGB	Red, green, blue
HSV	Hue, saturation, value

Chapter 1

Introduction

Genetic analysis is steadily gaining ground and as a result, significant applications in wide areas of the technology are emerging. Genetic analysis refers to the overall process of studies including identification of genes, inherited disorders and molecular biology [47]. The foundation of genetic analysis goes back to prehistoric times when humans settled down and started growing crops and breeding domesticated animals. Through practice, they observed that selective breeding could improve crops and animals. They also identified that some properties of species are inherent. Modern genetic analysis can be traced back to the works of Gregor Mendel, known as the *father of modern genetics*, whose experiments led to what is now known as Mendel's Laws of Inheritance. Observing various organism, Mendel found that traits were inherited from parents to children while those traits could vary between children. Later, it was found that there are specific units inside each cell responsible for inherited traits. These units are called genes. Nowadays, we know genes as determinants of the inherent properties of species. Genetic traits are governed by proteins that are created by series of amino acids. The specific portion of these series of amino acids are identified as genes. These series build up a double helix structure which is called Deoxyribonucleic acid (DNA). DNA itself is organized into long structures called chromosomes. Figure 1.1 shows how genes are identified within DNA.

Genetic analysis offer endless opportunities for new applications. In forensics, scientists can use DNA collected from a sample found at a crime scene such as

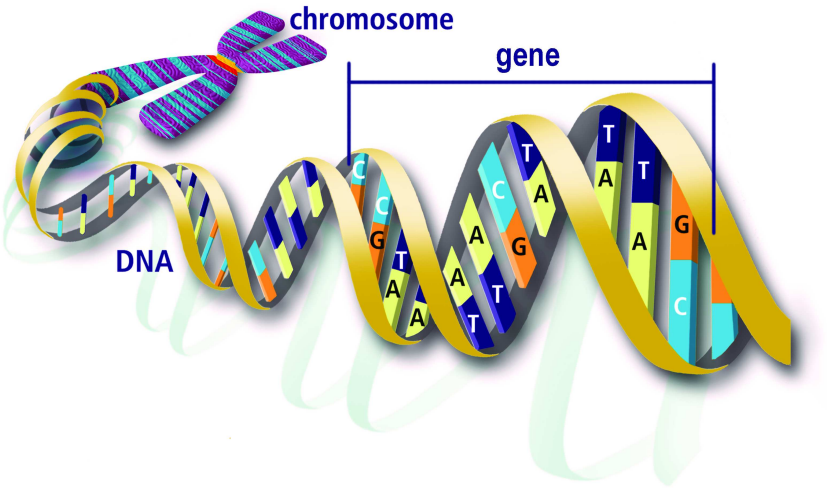

Figure 1.1: Genes, DNA and chromosomes [U.S. Department of Energy]

blood, semen, skin, saliva or hair to identify a matching DNA of an individual. This process which is formally called *DNA profiling*, also known as *genetic fingerprinting*, was developed in 1984 by British geneticist Sir Alec Jeffreys [55] and soon adopted in forensic science since 1988.

DNA profiling can also be used in the diagnosis of the hereditary diseases, detection and diagnosis of infectious diseases and early detection of cancer. By identifying the abnormally working genes in the cancer cells, doctors can diagnose the cancer in its early development stages which consequently increases the chance of treatment. In airports, DNA profiling has the promising potential to offer a quick and inexpensive way in detection of infectious diseases in people arriving by intercontinental flights and help to prevent an outbreak.

However, the amount of the DNA gathered from a sample is usually so small that it is near impossible to directly use it for the genetic analysis purposes. Hence, a technique to duplicate the DNA is required.

In 1983, Kary Mullis while driving down the Highway One in California had a vision that changed forensics and medicine forever [94]. He was thinking about the process by which bacteria continuously double in everyday world, producing millions of copies of their DNA in a single day. The idea he caught was "what if this exponential chain reaction could be harnessed in a test tube, amplifying a few

gene copies into virtually unlimited quantities for easy detection?". He tested and formulated this process using a heat-stable DNA copying enzyme (Taq polymerase). The polymerase chain reaction (PCR) he introduced revolutionized molecular biology [93]. Later in 1993, Mullis was awarded the Nobel Prize in Chemistry for his work on PCR.

The PCR method relies on a thermal cycling process of repeated heating and cooling to replicate the DNA. The PCR process can make billions of copies of the DNA samples which are sufficient for detection. Although PCR is an important part of the genetic analysis, a successful and precise genetic analysis requires other important steps to be carefully followed.

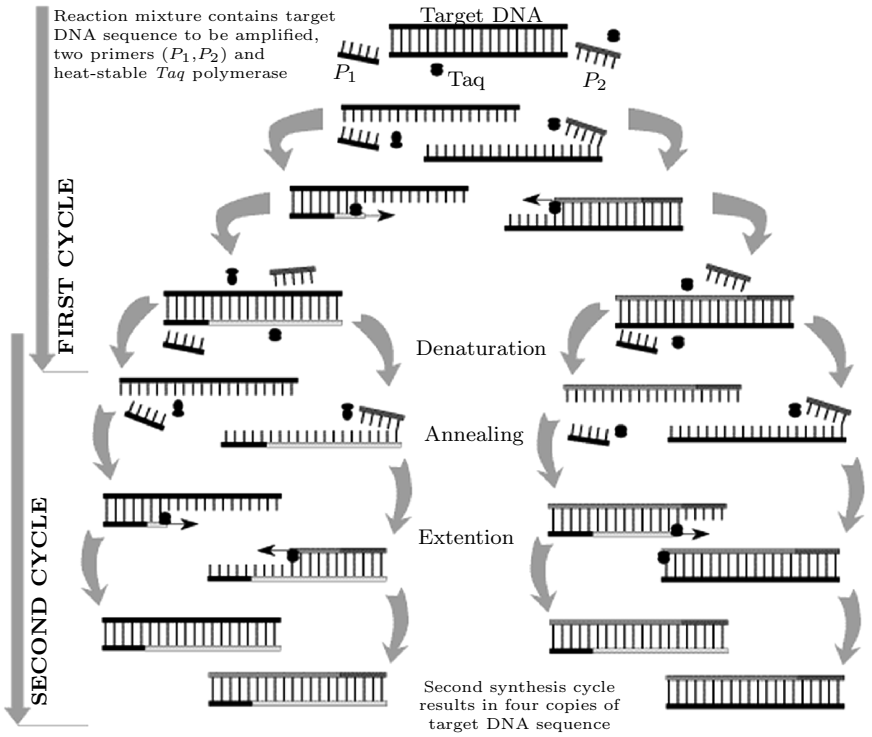

Figure 1.2: PCR Process

Genetic analysis usually consists of three steps: sample preparation, amplification and detection. In the first step the DNA is extracted from a raw sample such as blood. Then, a selected fragment of this DNA is amplified through the PCR process to obtain sufficient DNA copies to perform detection. Next, the amplified region of DNA is labelled with a fluorescent dye and finally is detected through various analysis techniques [59].

Traditionally, PCR thermal cycling is done in laboratories using equipment that requires relatively large volumes of costly reagents and DNA samples. PCR was a lengthy laboratory technique until the concept of lab-on-a-chip (LOC) devices was proposed in the early 1990s [98, 117]. A LOC device can be thought of as a miniaturized chemical or biological workbench that integrates many functionalities (e.g., sample pretreatment, sample transportation, mixing, reaction, separation and detection) that are typically performed in a well equipped laboratory by trained personnel.

Miniaturized LOC systems offer advantages beyond conventional biochemical and clinical laboratories. A distinct benefit of miniaturized LOC systems is the dramatic reduction of the costly reagents consumption. A high degree of automation relieves experimentalists from labor- and time-intensive biochemical characterization processes and hence allows more precise and reproducible analysis. Most significantly, miniaturization improves analysis characteristics, such as achieving shorter analysis time and higher separation performance, and can even achieve innovative applications that are not otherwise attainable.

Microfluidic devices, often used as part of a Lab-on-a-chip (LOC) capable of integrating several laboratory functions in a single chip, have seen a great deal of attention from the research community in recent years. Microfluidic devices were first used to develop inkjet printheads but today they are a central component in a variety of applications, ranging from chemical analysis and water contamination sensors to genetic analysis and point-of-care disease diagnostics [121]. Microfluidic-based LOC devices have the potential to change the way in which healthcare is delivered, by bringing fast, accurate diagnosis directly into the doctor's office which can yield high-throughput patient screening. LOC devices can also be made portable and can be used to detect infectious diseases, common viruses and etc.

1.1 Motivation

Targeting mass production capability, researchers in applied miniaturization laboratory (AML) at the university of Alberta recently developed a scalable and modular LOC-based genetic analysis device [58]. This device, depicted in Fig. 1.3, integrates

two important genetic analysis functionalities, PCR and capillary electrophoresis (CE), into one microchip.

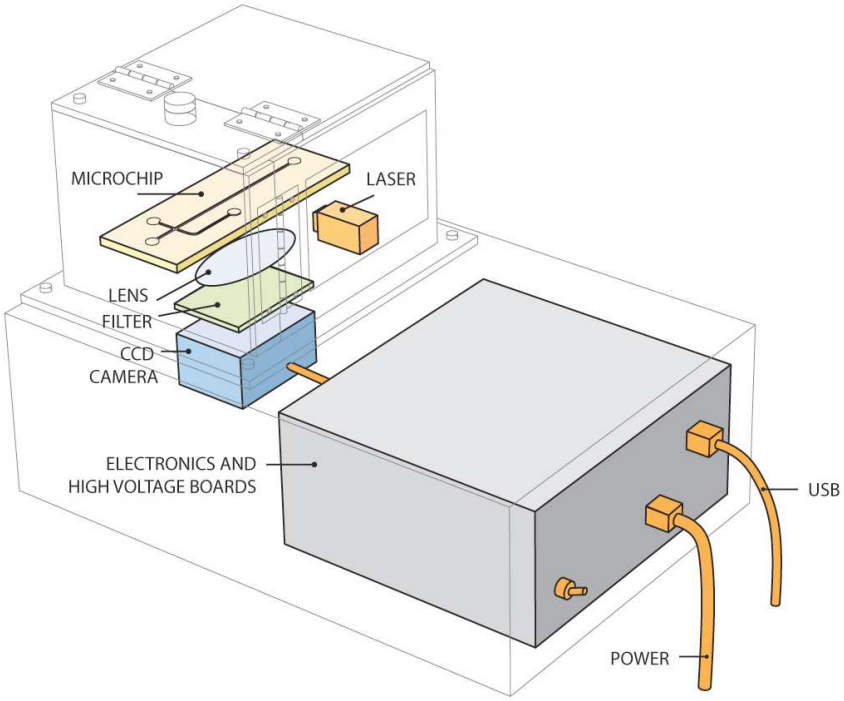

Figure 1.3: Schematic showing major functional blocks of the "shoe-box" sized portable platform (dimensions: 8″x10″x12″) that can perform a complete PCR-CE process [57]

CE is a technique in which high voltage is applied to the genetic information in a microfluidic channel, causing the genetic information to move in the direction of the applied electric field. When radiated with a focused light source, such as a laser beam, the genetic information is excited and emits fluorescence. The fluorescent intensity versus time (or electropherogram) can then be plotted to characterize the genetic information.

The device works such that a laser beam enters from the edge of the microchip, and a fraction of this light is coupled into the sieving matrix-filled CE channel. The DNAs tagged by fluorescent dye under the electrophoretic force migrate through the illuminated region of the channel, and the resulting emitted fluorescent light is focused, filtered and captured by a CCD camera.

The microchip is depicted in Fig. 1.4. The chip consists of a thin layer of Poly-di-methyl-siloxane (PDMS) sandwiched between two Borofloat glass layers. The DNA

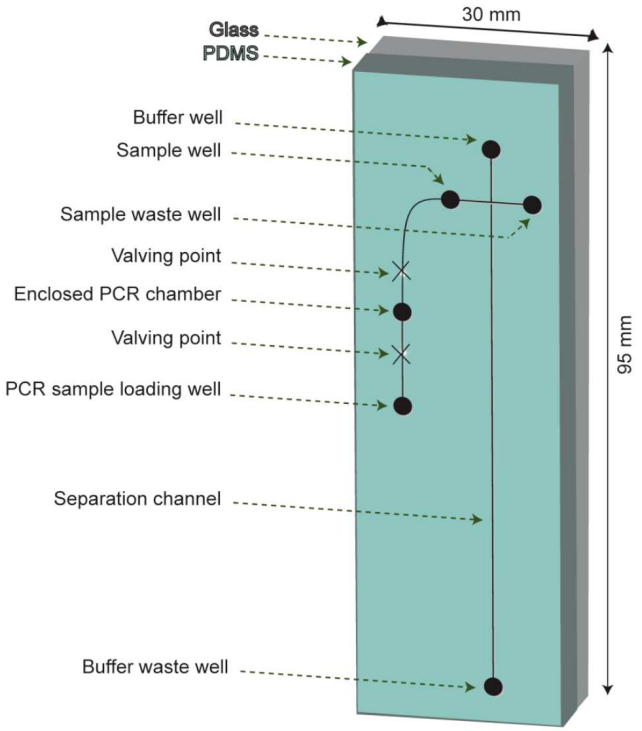

Figure 1.4: The hybrid PDMS-Glass microchip that integrated PCR-CE [57]

sample passes to an enclosed PCR reaction chamber after loading through "PCR sample loading well". The DNA amplification perform in PCR reaction chamber. Next, the amplified sample moves to the sample well and is finally collected in the sample waste well. Travelling through the crossing with separation channel, the amplified portion of the DNA separates down the longer CE channel (the separation channel) under the force of high electric field.

A more detail picture of the microchip is shown in Fig. 1.5. A cylindrical reaction chamber with a total volume of 0.64μL is machined at the bottom side of the top glass layer. The chamber is designed to hold the genetic sample during PCR thermal cycling. The actuator is a circular strip of platinum etched on the top side of the bottom glass layer and centred beneath the chamber.

The PCR method relies on a thermal cycling process of repeated heating and cooling to replicate the DNA. In each cycle, three steps are performed: denaturation (typically in the range of 92°C–96°C), annealing (typically 45°C–65°C), and extension (typically 68°C–74°C). A typical PCR cycling process is illustrated in Fig. 1.6 where N_0 is the number of original templates, n is the number of cycles, e_f is the

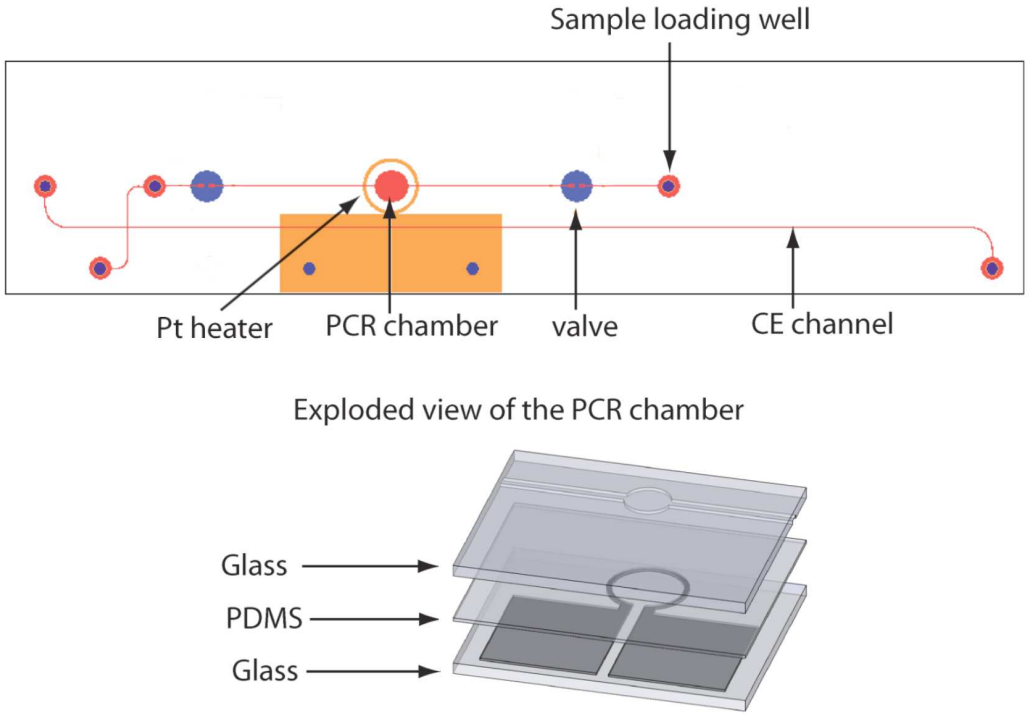

Figure 1.5: The detailed design of the PCR-CE microchip [57]

efficiency factor of the duplication process and N is the number of the final copies.

In an ideal PCR cycle with $e_f = 1$, the total number of the DNAs would be twice the number of the DNA samples before the PCR cycle. Multiple elements govern the properties of the cycling process, but a precise temperature control is a key factor in performing a successful PCR process. Depending upon the DNA sample's sensitivity and complexity, the high amplification efficiency typically requires a $\pm 1°C$ temperature precision at each temperature stage, minimized overshoot and undershoot in transitions and rapid transition time during temperature changes [119].

Regardless of the technology used in the LOC implementation, temperature control is critical to the efficiency of the DNA amplification process. Accurate temperature control, however, requires measuring the temperature inside the reaction chamber before it is fed back to the controller, a process that presents multiple challenges. Indeed, in a typical microfluidic LOC device, the volume of liquid inside the reaction chamber (including the DNA sample and reagents) can be on the order of a few micro litres. Therefore, any sensing device directly in contact with such a small volume will exchange an amount of heat, significant enough to affect the DNA

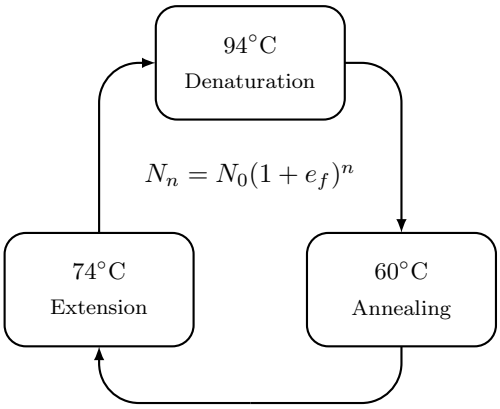

Figure 1.6: DNA amplification by thermal cycling in PCR process

cycling. Implanting a sensing device inside the reaction chamber can also increase the risk of sample contamination with the consequent negative effects on the PCR process. As a result, it is highly desirable, if not mandatory, to have some sort of estimation of the temperature *inside* the chamber, based on *outside* measurements. Depending upon the LOC's geometric construction, the problem can be challenging.

In general, despite the small volumes of liquid involved, the temperature inside the chamber follows a heat distribution law and naturally leads to a distributed parameter system that can be represented using partial differential equations (PDEs).

In summary, the thermal control problem of the particular PCR microchip considered in this research is tied down by following challenges:

- Due to the PDE nature of the heat distribution inside the microchip, the logical choice is to use the theory of the analysis and control of the distributed parameter systems to deal with the problem considered in this thesis.

- The complex structure of the PCR microchip only permits actuation and measurement from its boundaries, in spite of the fact that the control variable is located inside the microchip. Moreover, the actuation and sensing are collocated at a particular trace on the boundary. So the type of the control problem is the boundary control problem.

- The control problem involves certain constraints. For example, the temperature at the actuation boundary must be limited to 200°C to prevent permanent damage to the microchip. Overshoots and undershoots can significantly

degrade the efficiency of the PCR process and should be minimized. Also, similar to many other practical applications, the actuation signal has a maximum limit.

- Considering all the complexities and constraints, the objective of the thermal control problem of the PCR microchip is to minimize the transition times in the PCR thermal cycling process and maintain tight fluctuation limits in each of the temperature stages.

Motivated by the challenges listed above, in this thesis we adopt available techniques and develop new techniques and tools to effectively enhance the thermal management performance for the chosen PCR microchip.

1.2 Background

The applications of the Lab-on-a-Chip technology has been impressively growing since its early demonstration by Burn *et al* [20] integrating DNA amplification and detection in a microchip scale. Although their system was not sufficiently sensitive and flexible for general application, they proved it is feasible to build a lab-on-a-chip system. As the ice of the scepticism toward the feasibility of the LOC technology was broken, new advancements appeared. Consequently, a first portable fully integrated PCR-CE system was introduced by Legally *et al* [72]. Other state-of-the-art LOC systems were later demonstrated by Mathies group [82] and Meagher *et al* [91]. The main problem almost all of these demonstrations shared was the excessive overall cost of the system that prevented the application in point-of-care diagnosis as pointed out in recent reviews[73, 95, 121, 120].

Several technologies capable of handling microfluidic-based PCR-LOC devices have been reported in the literature [106]. The primary differences among these technologies are the thermal heating method and architecture of the LOC which may serve specific purposes. Heating methods which are commonly used include *contact-mode "peltier" modules* [61, 96], *patterned thin-film resistive heaters* [60, 54], *noncontact mode infrared radiation* [45], *laser-mediated heating* [114], and *microwave heating* [108].

The integrated genetic analysis platform that has been developed in the Applied Miniaturization Laboratory (AML) at the University of Alberta is designed based on the patterned thin-film resistive heater technology. This platform is capable of performing complete genetic analysis on a single microfluidic chip [58]. The full potential of this device is hidden under the hood. This potential power could be fully fictionalised by a carefully designed thermal control system.

As pointed out in the previous section, the dominant physical phenomena surrounding the chosen LOC system naturally leads toward the use of distributed parameter systems theory. A PDE system can be represented in a state-space form as a distributed parameter system which presents infinite dimensional states. On the contrary, an ordinary differential equation (ODE) system can be represented as a lumped parameter system which only contains finite number of the states. In contrast to lumped systems, a function of interest in a PDE system not only depends on time but also independently depends on space. In the other word, a PDE system is both temporally and spatially distributed.

The traditional approach dealing with control of PDE systems can be divided into three categories: early lumping approach, late lumping approach and pure PDE design. In the early lumping approach, the system is approximated in the first step by using spatial discretization techniques to a finite dimensional system described by ODEs capturing the dominant modes of the PDE system. The design process is subsequently followed by synthesis of finite dimensional controllers for the resulting system [7, 104, 30].

The early lumped approach, however, often leads to high-dimensional and complex feedback control structures. Many other well-known disadvantages are associated with this approach. For example, fundamental control properties such as controllability and observability which should depend only on the location of the sensors and actuators, may also depend on the discretization method and the number and location of discretization points [104]. Moreover, a closed-loop system may become unstable due to the neglected dynamics [6]. In the late lumping approach, the infinite-dimensional process model is picked at the first step but, later, during the control law design, the equations are discretized. It cannot be denied that in order to practically implement a distributed parameter control system in a real-world

application, lumping should occur at some point either at the early or at final stage of the design.

Early and late lumping approaches are extensively described in many good books covering the theory of the analysis and control of the distributed parameter systems [80, 34, 75, 42, 21, 26]. In [34], Curtain and Zwart presented a state-space theory for infinite-dimensional linear systems using the semi-group theory. Classical state space concepts of input-output controllability, observability, stabilizability, detectability and the transfer function of the infinite dimensional system on a Hilbert space were generalized afterwards. The linear quadratic optimal control problem on a finite and infinite time horizon is also addressed by Fursikov in [42]. Lasiecka and Triggiani in [75] provided a thorough treatment of the theory of infinite dimensional approximation. While the mentioned references provided useful methods for analysis and control synthesis for distributed parameter systems with actuation and measurement distributed inside the spatial domain of the system (in-domain), the boundary control problem for distributed parameter system has remained relatively unexplored. Boundary control PDE systems are those distributed parameter systems in which measurement and control is only possible through their boundaries. Doubtlessly, in many real-world applications the actuation and sensing are present only at the physical boundaries. The complexity in optimal boundary control of the distributed parameter systems comes from the fact that applying semi-group theory to design an optimal boundary controller will usually lead to unsolvable algebraic Riccati operator equations [69].

Very recently, the well-known *backstepping* approach to control design was generalized to systems described by partial differential equations, [69, 109, 110]. An important feature of this approach is the constructive nature of the design, which uses classical Lyapunov stability theory, making the design process relatively straightforward. The basic idea and results of backstepping go back to work of Colton [28] and Seidman [107], where integral transformations were used to solve PDEs and state controllability results. However, those results were not used for the design of feedback laws.

Subsequent attempts were made on PDE backstepping by Krstic and co-workers [9, 16, 15, 17] which relied on spatial discretization. As they point out, their approach

is highly dependent on the discretization scheme and does not yield convergent integral transformation kernels when the size of the discretization grid converges to zero. Interestingly, they observed that the control action signal produced by the same non-convergent kernel is convergent. In [83, 109, 110], they solved this issue by describing the integral transformation kernel by its compact solution and demonstrate their theory on various classes of the PDE systems. Smyshlyaev and Kristic nicely summarized their theory in [69] covering the PDE backstepping design for boundary control and observation.

References [69, 109] and [110], however, deal exclusively with one-dimensional systems. The extension of PDE backstepping boundary design to higher order systems is non-trivial as the complexity of the approach can quickly make the problem intractable. Kristic and Smyshlyaev in [111] provided some general guidelines for special systems in two and three dimensions, but, in general, backstepping control for high order PDE systems remains unsolved.

Observer design for infinite-dimensional systems is also a challenging problem. Research in control and state estimator design for distributed parameter systems can be traced back to the 60s and 70s [3]. Kitamura *et al.* [63], and Gressang and Lamont [46] developed conditions to generalize observer theory to infinite dimensional systems. El Jai and Amouroux [41] showed that because of the distributed nature of the problem, sensor location can have a detrimental effect on the observer existence. Liu and Lapidus [84] incorporated a Lyapunov-based observer design for linear and non-linear distributed-parameter diffusion systems. Yaz *et al.* [118] introduced the receding-window observer that has a structure similar to a Kalman filter and proved its convergence in the presence of bounded noises and parameter perturbation. Miranda *et al.* [92] proposed a sliding-mode observer by adding the sliding-mode term to the PDE backstepping boundary observer. This method is further developed for feedback stabilization [24]. Adaptive observers are discussed in [79, 64, 35, 31, 33, 32].

1.3 Research Goals and Methods

The main objective of this research is *to develop a theoretical framework based on the theory of analysis and synthesis of the distributed parameter systems that can be used to design and implement an advanced thermal management system for the PCR microchip.*

In order to achieve the mentioned objective, we set the following goals:

- The temperature distribution inside the PCR microchip, including the reaction chamber, is a distributed parameter system in which the temperature is spatially and temporally distributed in the space and time. Hence, our first goal is to develop and verify a PDE model describing the dynamics of heat distribution inside the PCR microchip.

- The main control variable in our problem is not accessible for direct measurement, and the system's structure only allows boundary measurement. Our second goal is to design a boundary observer for the PCR microchip to precisely estimate the temperature inside the PCR process chamber.

- Any PDE controller and observer must be spatially discretized at some point to enable its simulation and implementation. Our third goal is to adopt a space discretization method and extend it to be used to calculate interconnected PDE systems.

- Many constraints must be considered in the implementation phase. PDE controllers are in their infancy and many problems are associated with their implementation. Measuring the control variable using the PDE observer makes it possible to use a lumped controller to shape the input signal. Our final goal is to design a controller in order to appropriately satisfy the problem objectives considering all the constraints.

1.4 Thesis Contributions

The major contributions of the research considered and presented in this thesis are listed below:

1. Development of a PDE model and calculated its full solution describing the heat distribution inside the microfluidic DNA analysis microchip.

2. Extension of the characterization method of using thermochromic liquid crystal (TLCs) to dynamic characterization of thermal properties of the PCR-LOC microchip.

3. Extension of the PDE backstepping boundary observer design technique to a 2-D cylindrical domain structure.

4. Simplification of the PDE backstepping boundary observer and controller designs via use of a conformal transformation.

5. Development of a numerical technique based on compact finite difference, enabling the simulation of interconnected PDE systems.

6. Development and implementation of an advanced thermal management system consisting of a model predictive controller and a PDE observer for the PCR-LOC microchip.

1.5 Applications

A major contribution in this thesis is the use of classical complex analysis in the solution of the PDE backstepping theory and especially extension to higher dimensions. It is the author's belief that the same principles are applicable in a wide range of distributed parameter control problems. Some potential applications are the following:

Flexible Structures [5, 68]: Hyperbolic PDE equations govern flexible structures in civil engineering applications, aircraft wings and helicopter rotors, astronomical telescopes, and in nanotechnology devices such as the atomic force microscope. A recent application of distributed control is in active control of cantilever beams in micro-devices with piezoelectric actuators.

Fluids, Aerodynamics, Turbulences, Propulsion, Acoustics: In many applications PDE equations are playing key roles in systems dynamics such as in fluid flows [52, 50, 25], aerodynamics and propulsion applications, acoustic waves [48, 4] and water waves irrigation systems, instabilities in thin film manufacturing and in flame dynamics [78]. In irrigation systems, nonlinear hyperbolic PDEs describe the gravity-based laminar fluid flow in canals and rivers [81, 27]. Distributed parameter control systems have the potential of offering a better performance than the lumped model control of those systems.

Quantum Control [86] : Some compelling applications are identified in chemistry, optical networking, computer science and in the design and implementation of advanced nano-scale technologies.

Delays [12, 67, 66, 105] : Time delay arises in various engineering applications such as process control, mass transport in stirred-tank reactors and heat exchangers, population dynamics and traffic flows. Delays can severely degrade the performance of the control system. Some recent advances reported in the literature involve stabilizing the nonlinear and linear time invariant (LTI) systems with input and state delays using tools coming from the adaptive control of parabolic PDEs.

Magnetohydrodynamic (MHD) Flows [116, 112] : MHD refers to the study of the dynamics of electrically conducting fluids such as plasma, liquid metals and electrolytes. When a moving conductive fluid passes through a magnetic field, electric current is induced in it, which in turn creates forces on the fluid and affects magnetic field as well. MHD is governed by a combination of the Navier-Stokes and Maxwell's equations. MHD has applications in cooling nuclear reactors or computing devices, plasma confinement in fusion reactors, pumping in microfluidic devices, magnetic drug targeting and electromagnetic casting. Feedback control can effectively enhance mixing and heating transfer, prevent instability in tokamak and reduce pumping power in MHD applications.

1.6 Thesis Outline

The rest of the dissertation is organized as follows:

Chapter 2 presents, in detail, the definition of the problem involved in this dissertation. The PCR-LOC microfluidic microchip is fully described and an analytical model is developed describing the dynamics of the heat distribution around the PCR chamber inside the microchip. Next, the PDE equation in the analytical model of the PCR-LOC microchip is fully solved. Having a general solution of the model in hand, the model parameters are optimized to maximize the fit between the model and the actual microchip. The model is fully verified using precise FEM simulations and the experimental characterization of the microchip.

Chapter 3 is concerned with the observer design problem. In section 3.3 we pose the observer design problem in standard backstepping form, which results in a four-dimensional PDE equation. In 3.4 we introduce conformal mapping and provide a step-by-step approach to reduce the original problem into one with a much simpler structure that results in a two dimensional PDE. In section 3.5 we take advantage of the new structure and complete the observer design using the PDE backstepping boundary observer design technique.

In chapter 4, we numerically solve the PDE equation describing the kernel function of the PDE backstepping boundary observer developed in chapter 3. Also, we calculate the observer parameters. To enable performing simulation scenarios on the interconnected system composed of the PDE model and PDE observer, we developed a discretization technique based on the compact finite difference method. The simulation results are presented and discussed. In addition, the observer design is verified using TLC sensors implanted inside the microchip. A signal processing algorithm is developed to use the characterization data in the observer verification process.

Chapter 5 presents the implementation of the thermal management system on the selected PCR-LOC microchip. The experimental setup is illustrated and the interfacing circuit design is discussed in detail. Next, the design of the Model predictive control (MPC) is presented and the simulation results verifying its performance are depicted. Finally, the result of full system implementation, including the PDE

observer and MPC controller, are discussed.

In chapter 6, we present an extension of the PDE backstepping control design to 2-D cylindrical coordinate system. We show that the design goes in parallel with our technique developed and discussed in chapter 3. However, the resulting design presents aggressive control action signals that makes it not a suitable choice to be incorporated into the thermal management of the PCR-LOC device which has certain constraint on control action.

Chapter 7 presents the summary of the research. The major contributions of the thesis are high lighted and future directions are discussed.

Chapter 2

Modeling

2.1 Introduction

In this chapter, we present the development of a mathematical model for the PCR microchip. As briefly introduced in Chapter 1, the PCR microchip that we considered in this dissertation features a thin layer of Poly-di-methyl-siloxane (PDMS) sandwiched between two Borofloat glass layers which results in a multi-domain model structure. Calculating a general solution for a multi-domain PDE problem (or coupled PDEs) is usually either very difficult or non-solvable in most of the cases. Moreover, any later attempt to design a controller or an observer for a multi-domain PDE system would be intractable [74].

In order to account for this problem, we take an innovative approach. In this chapter, we show that it is possible to use a single-domain PDE model to approximate the heat distribution in an important portion of the multi-domain full model which contains the PCR chamber and the heater ring. We provide the general solution for the simplified model that describes both the steady-state and the transient heat distribution inside the domain. Next, we formulate an optimization problem for this model in order to minimize the mismatch between heat distribution in the real system and the heat distribution approximated by the model. In the following section, we inspect the PCR microchip in more detail enabling us to chose a useful modeling framework.

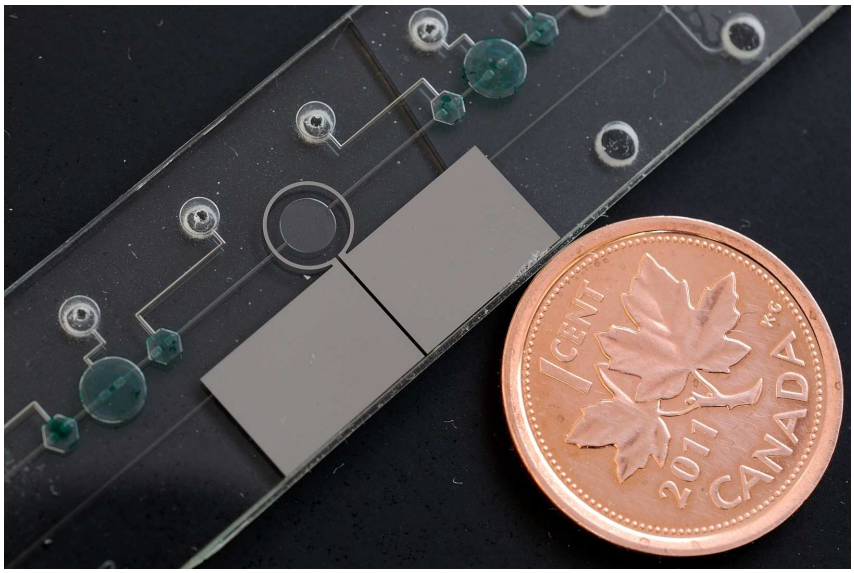

Figure 2.1: PCR-CE microchip developed at the University of Alberta

2.2 Microchip Structure

A pictorial description of the microfluidic chip considered in this work is given in Fig. 2.1 (see also [58] for a complete description). As seen in the figure, the PCR reaction chamber is surrounded by a resistive heater ring. The squares plates in the picture are the heater contact pads.

The microchip consists of a thin layer of Poly-di-methyl-siloxane (PDMS) sandwiched between two Borofloat glass layers. A cylindrical reaction chamber with a total volume of 0.64μL is machined at the bottom side of the top glass layer. The chamber is designed to hold the genetic sample during PCR thermal cycling. The actuator is a circular strip of platinum etched on the top side of the bottom glass layer and centred beneath the chamber. The platinum heater acts both as actuator and sensor and is the only temperature information available from measurement. The temperature inside the chamber must be estimated based on this reading. A copper heat-sink with a circular opening in its centre is placed underneath the microchip to improve the cooling rate during thermal cycling [51]. The fluid flow microchannels, microvalves and micro pumps are not considered in our analysis as they are placed relatively far from the reaction chamber and their effect on heat distribution in the neighbouring chamber is negligible. The previous version of this microchip had a different structure where a Peltier actuator was used to provide active cooling to

improve the cooling rate. Complete modeling and controller design for a previous version of the microchip are presented in [56].

We are mostly interested in heat transfer dynamics around the reaction chamber and heater-sensor ring. The chamber, heater/sensor and heat-sink opening are circular and share the same axis. This suggests that we should look for an axisymmetric cylindrical structure for our model. Fig. 2.2 shows the half cross-section view of the chip along a vertical plane parallel to the smaller side and passing through the center of the chip. Due to the axysimmetric geometry of the chip, only half of the chip is shown. The axis of symmetry is along the left vertical side. A circular hole is cut in the middle of the heatsink to provide thermal insulation under the heater and chamber. Heat is lost by free convection on the top and by conduction through the heatsink.

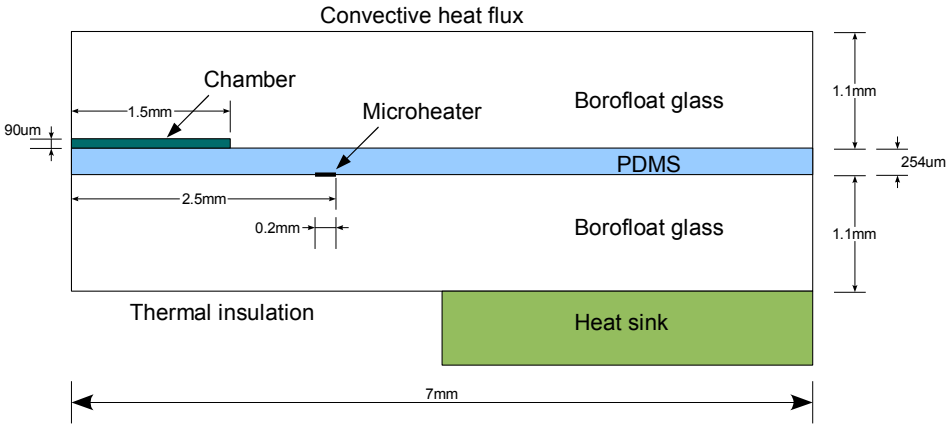

Figure 2.2: Cross-section view and dimensions of the PCR-LOC microchip [51]

Figure 2.3 depicts the heat distribution in the PCR microchip after applying one Watt of power to the heater. The calculation was performed using finite element model analysis. As shown, the coolest part of the microchip is its boundary with heat-sink experiencing a temperature of 22°C and the hottest part is the heater with a temperature of 104.38°C.

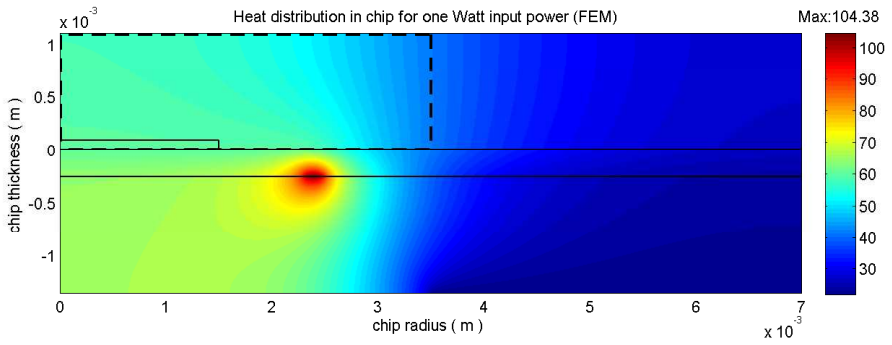

Figure 2.3: Heat distribution in PCR chip (FEM model)

2.3 Modeling Framework

The irregular and multi-layer multi-material structure of the PCR microchip is not suitable to form a set of solvable analytic equations and additional simplifications are needed. To find a simplified model describing the dynamics of the chip where the heater and chamber are located, we first consider the temperature profile around the heater and chamber area. Fig. 2.4 depicts the temperature profile along the chip thickness for some selected distances from the center of the chip, ranging from 2.5mm to 5.0mm. Referring to Fig. 2.4, the temperature profile along the thickness of the chip at the upper glass layer (1.354mm to 2.454mm from the bottom of the chip) shows a semi linear trend. Each curve shows the temperature along a vertical line that crosses through the chip. Such a line is placed at a defined distance from the centre. The legend shows the radial distance in millimetres. The horizontal axis represents the vertical distance from the bottom to the top of the chip, which is 2.454mm thick. As the distance from the center increases from 2.5 to 5mm the curves flatten down towards 22°C. The temperature along the vertical distance inside the top glass plate (right side of the curves) is almost constant. By choosing the radius of 3.5mm from the center of the chip, the slope is negligible, as the temperature varies less than 0.8°C, which is within the acceptable error for the chamber temperature during PCR thermal cycling.

Therefore, with reasonable approximation, we can consider a constant temperature wall as the boundary, where this boundary is positioned at a distance of 3.5mm from the center of the chip. These calculations, in addition to several other

FEM simulations, have been performed using **COMSOL Multiphysics 3.5a** on a comprehensive FEM model of the chip that describes its layered geometry, material properties and boundary conditions with a high degree of accuracy. More

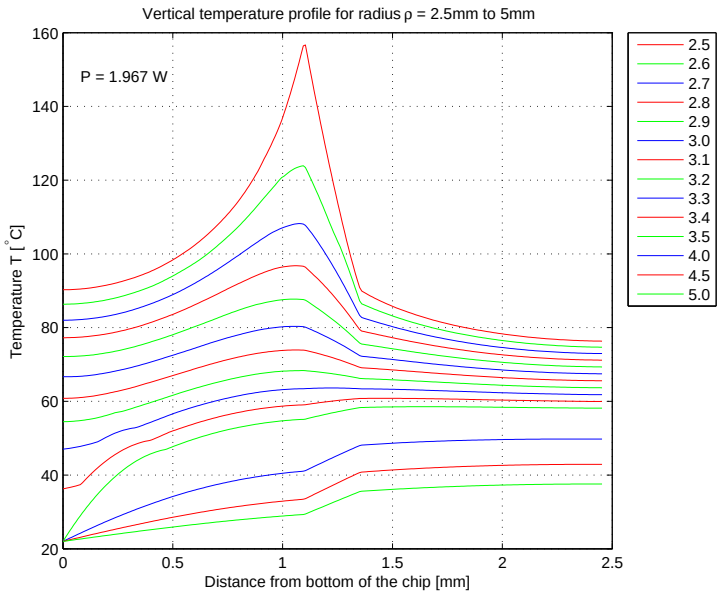

Figure 2.4: Vertical temperature profile of the PCR microchip at steady-state

FEM simulations show some other important facts about this chip which can be summarized as follows:

1. The amount of heat going to the upper portion of the chip through the PDMS and top glass layer has an approximately constant ratio to the total heat being dissipated by the heater.

2. If we consider a disk-shape bounded volume at the center of the chip, the amount of heat lost by natural convection in air through the upper surface of the disk is negligible compared to the amount of heat lost by conduction through the wall.

3. If the PDMS layer were replaced by a glass layer, only a small percentage of the dynamic temperature distribution would be affected, due to the alteration of thermal properties (thermal conductivity and specific heat capacity). This small effect on the dynamics can be compensated later by using a correction factor.

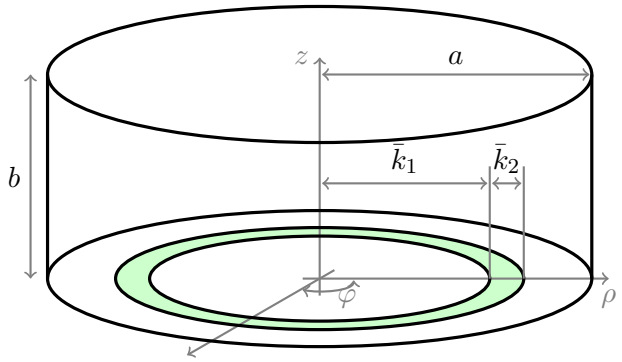

Figure 2.5: Model structure of the PCR microchip

4. The vertical temperature profile in the top glass layer at a distance of 3.5mm from the center is approximately constant.

Using these observations we can conclude that by picking a single layer glass disk, we can model the temperature distribution at a closed disk in the upper side of the chip with a good level of approximation relative to the temperature accuracy of $\pm 1°$C demanded by the PCR process. This model structure is shown in Fig. 2.5 where the heater is defined by the circular strip at the bottom surface with k_2 width and k_1 distance to the vertical axis.

It is worth noting that our model only approximates the heat distribution in the area of interest in the chip, and we have put aside the rest of the chip. We will later optimize the dimensions of this model to arrive to a least-error approximation of the heat distribution. The rational in choosing this scenario is to arrive to a model structure that is simple enough to find its analytical solution but accurate enough to characterize the actual thermal process. The FEM model by itself was verified by extensive experiments, wherein thermochromic liquid crystals (TLCs) sensitive to different temperatures were deposited in the chamber to read the temperature within its volume in steady-state.

2.4 Analytical Formulation

The heat diffusion inside the model structure, depicted in Fig. 2.5, is governed by the heat equation, [19]:

$$\kappa \nabla^2 u = \frac{\partial u}{\partial t}, \tag{2.1}$$

where $u(\rho, \varphi, z, t)$ is the temperature of every point of the domain at any given time t, and κ is thermal diffusivity. Thermal diffusivity for any substance is defined by

$$\kappa = \frac{K}{\bar{\rho}\,\mathcal{C}}, \tag{2.2}$$

where K is thermal conductivity, $\overline{\rho}$ is density and $\mathcal{C}$ is specific heat capacity of that particular substance. In our case, the Borofloat glass is the substance that builds up the domain. The Laplace operator in a cylindrical coordinate system is defined as follows:

$$\nabla^2 u = \frac{\partial^2 u}{\partial \rho^2} + \frac{1}{\rho}\frac{\partial u}{\partial \rho} + \frac{1}{\rho^2}\frac{\partial^2 u}{\partial \varphi^2} + \frac{\partial^2 u}{\partial z^2}.$$

Since the model features axial symmetry, the temperature in the cylinder does not depend on φ. This means that $\frac{\partial u}{\partial \varphi} = 0 = \frac{\partial^2 u}{\partial \varphi^2}$. Therefore the Laplace operator can be written in the following 2-D form:

$$\nabla^2 u = \frac{\partial^2 u}{\partial \rho^2} + \frac{1}{\rho}\frac{\partial u}{\partial \rho} + \frac{\partial^2 u}{\partial z^2}, \tag{2.3}$$

The definition of the chosen domain implies that ρ and z are limited to $0 \leq \rho \leq a$ and $0 \leq z \leq b$. The initial and boundary conditions are given by

$$u(\rho, z, 0) = u_0(\rho, z) \tag{2.4}$$

$$u(a, z, t) = T_w \tag{2.5}$$

$$u_\rho(0, z, t) = 0 \tag{2.6}$$

$$u_z(\rho, b, t) = 0 \tag{2.7}$$

$$u_z(\rho, 0, t) = -f(\rho), \tag{2.8}$$

where $u_0(\rho, z)$ is the initial distribution of temperature. T_w is the temperature of the outside wall of the cylinder. The boundary condition (2.6) comes from the axisymmetrical cylindrical structure of the model. The boundary condition (2.7) is based on the assumption that the upper surface of the chip is isolated. $f(\rho)$ describes the geometric distribution of the control action signal at the bottom surface, which is defined by the heater location. A general solution of (2.1) can be found by adding the solution of homogeneous and non-homogeneous equations describing the steady-state and a transient temperature distribution, respectively:

$$u(\rho, z, t) = \hat{u}(\rho, z, t) + \bar{u}(\rho, z). \tag{2.9}$$

Substituting (2.9) in (2.1) we get

$$\begin{aligned}\frac{1}{\kappa}\hat{u}_t &= \hat{u}_{\rho\rho} + \bar{u}_{\rho\rho} + \frac{1}{\rho}\hat{u}_\rho + \frac{1}{\rho}\bar{u}_\rho + \hat{u}_{zz} + \bar{u}_{zz} \\ &= \left(\hat{u}_{\rho\rho} + \frac{1}{\rho}\hat{u}_\rho + \hat{u}_{zz}\right) + \left(\bar{u}_{\rho\rho} + \frac{1}{\rho}\bar{u}_\rho + \bar{u}_{zz}\right).\end{aligned} \tag{2.10}$$

Without loss of generality, we can assume that $\bar{u}_{\rho\rho} + \frac{1}{\rho}\bar{u}_\rho + \bar{u}_{zz} = 0$, as we defined $\bar{u}(\rho, z)$ to describe the steady-state temperature. By applying (2.9) to the initial condition (2.4) and boundary conditions (2.5), (2.6), (2.7) and (2.8), we arrive at two PDEs:

$$\frac{1}{\kappa}\hat{u}_t = \hat{u}_{\rho\rho} + \frac{1}{\rho}\hat{u}_\rho + \hat{u}_{zz}, \tag{2.11a}$$

subject to

$$\hat{u}(\rho, z, 0) = \hat{u}_0(\rho, z) \tag{2.11b}$$

$$\hat{u}(a, z, t) = 0 \tag{2.11c}$$

$$\hat{u}_\rho(0, z, t) = 0 \tag{2.11d}$$

$$\hat{u}_z(\rho, b, t) = 0 \tag{2.11e}$$

$$\hat{u}_z(\rho, 0, t) = 0, \tag{2.11f}$$

and

$$\bar{u}_{\rho\rho} + \frac{1}{\rho}\bar{u}_\rho + \bar{u}_{zz} = 0, \tag{2.12a}$$

subject to

$$\bar{u}(a, z) = T_w \tag{2.12b}$$

$$\bar{u}_\rho(0, z) = 0 \tag{2.12c}$$

$$\bar{u}_z(\rho, b) = 0 \tag{2.12d}$$

$$\bar{u}_z(\rho, 0) = -f(\rho). \tag{2.12e}$$

Equation (2.11a) is an initial value problem with homogeneous boundaries, while (2.12a) is a non-homogeneous boundary value problem.

2.4.1 Solution of the Analytical Model

Steady-state

To solve (2.12a), we employ the method of separation of variables [19]. We assume that the steady-state heat distribution defined by (2.12a) cab be written as follows:

$$\bar{u}(\rho, z) = P(\rho)Z(z) + T_w, \tag{2.13}$$

where P, Z are functions of ρ, z respectively. The constant part in (2.13) is used to normalize the boundary conditions and achieve the homogeneous boundary conditions. Substituting (2.13) in (2.12a) and dividing it by $P(\rho)Z(z)$, we arrive to

$$\frac{P''(\rho)}{P(\rho)} + \frac{1}{\rho}\frac{P'(\rho)}{P(\rho)} = -\frac{Z''(z)}{Z(z)}.$$

The left side contains functions of ρ alone, while the right side contains functions of z alone. Since this equality must hold for all ρ and z in the given interval, the common value of the two sides must be a constant, say $-\lambda^2$, varying neither with ρ nor with z.

$$\frac{P''(\rho)}{P(\rho)} + \frac{1}{\rho}\frac{P'(\rho)}{P(\rho)} = -\lambda^2 = -\frac{Z''(z)}{Z(z)}.$$

The constant here is chosen as a negative value to avoid a trivial solution [19]. Now we have two ODEs for the two factor functions:

$$\rho P'' + P' + \lambda^2 \rho P = 0, \tag{2.14}$$

and

$$Z'' - \lambda^2 Z = 0. \tag{2.15}$$

Taking account of (2.13), the boundary conditions (2.12b) to (2.12e) results in:

$$P(a) = 0 \tag{2.16}$$

$$P'(0) = 0 \tag{2.17}$$

$$Z'(b) = 0 \tag{2.18}$$

$$P(\rho)Z'(0) = -f(\rho). \tag{2.19}$$

The solutions of (2.14) and (2.15) are given by [19],

$$P = c_1 J_0(\lambda\rho) + c_2 Y_0(\lambda\rho), \tag{2.20}$$

and

$$Z = c_3 \cosh \lambda(b-z) + c_4 \sinh \lambda(b-z), \tag{2.21}$$

respectively, where J_0 is the Bessel function of the first kind of order 0 and Y_0 is the Bessel function of the second kind of order 0. The Bessel functions of the first kind, J_n, and the Bessel functions of the second kind, Y_n, both of order n, are given by:

$$J_n(x) = \sum_{r=0}^{\infty} \frac{(-1)^r}{r!\,\Gamma(n+r+1)} \left(\frac{x}{2}\right)^{n+2r}$$

and

$$Y_n(x) = \begin{cases} \frac{J_n(x)\cos n\pi - J_{-n}(x)}{\sin n\pi} & n \neq 0, 1, 2, 3, \cdots \\ \lim_{p\to n} \frac{J_p(x)\cos p\pi - J_{-p}(x)}{\sin p\pi}, & n = 0, 1, 2, 3, \cdots \end{cases}$$

where Γ is the gamma function defined by

$$\Gamma(n) = \int_0^{\infty} x^{n-1}\, e^{-x} dx.$$

When n is a positive integer, the gamma function is defined by

$$\Gamma(n) = (n-1)!.$$

From the boundedness condition at $\rho = 0$, stated by (2.17), we must have $c_2 = 0$ because Y_0 is unbounded at zero. Thus the solution (2.20) becomes

$$P = c_1 J_0(\lambda\rho). \tag{2.22}$$

From the boundary condition (2.18) and the fact that

$$Z'(z) = -\lambda \left(c_3 \sinh \lambda(b-z) + c_4 \cosh \lambda(b-z)\right) \tag{2.23}$$

we have

$$Z'(b) = -\lambda c_4 = 0,$$

which implies $c_4 = 0$, so the solution (2.21) becomes

$$Z(z) = c_3 \cosh \lambda(b-z). \tag{2.24}$$

The boundary condition (2.16) can be employed to determine λ:

$$P(a) = c_1 J_0(\lambda a) = 0,$$

which is satisfied only if $J_0(\lambda a) = 0$ so that

$$a\,\lambda = r_1, r_2, r_3, \cdots, r_m, \cdots$$

where $r_m (m = 1, 2, 3, \cdots)$ is the mth positive root of $J_0(x) = 0$. Thus λ's can be expressed as

$$\lambda_m = \frac{r_m}{a} \quad , \quad m = 1, 2, 3, \cdots . \tag{2.25}$$

So a solution satisfying the boundary conditions is

$$\bar{u}(\rho, z) - T_w = P_m(\rho) Z_m(z) = A J_0(\frac{r_m}{a}\rho) \cosh \frac{r_m}{a}(b - z),$$

where $m = 1, 2, 3, \cdots$ and $A = c_1 c_3$. The general solution of (2.12a) can be obtained by employing the superposition principle [19]. By replacing A with A_m and summing over all eigenfunctions it follows that

$$\bar{u}(\rho, z) = T_w + \sum_{m=1}^{\infty} A_m J_0(\frac{r_m}{a}\rho) \cosh \frac{r_m}{a}(b - z). \tag{2.26}$$

From

$$\frac{\partial \bar{u}}{\partial z} = \sum_{m=1}^{\infty} -A_m \frac{r_m}{a} J_0(\frac{r_m}{a}\rho) \sinh \frac{r_m}{a}(b - z) \tag{2.27}$$

and the last boundary condition (2.19) we can write:

$$\sum_{m=1}^{\infty} \left(A_m \frac{r_m}{a} \sinh \frac{r_m\, b}{a} \right) J_0(\frac{r_m}{a}\rho) = f(\rho). \tag{2.28}$$

The right side of (2.28) is the Bessel series expansion of $f(\rho)$ with coefficients equal to $\left(A_m \frac{r_m}{a} \sinh \frac{r_m\, b}{a}\right)$ [19], so we get,

$$A_m = \frac{2}{a r_m \sinh(\frac{r_m\, b}{a})\; J_1^2(r_m)} \int_0^a \rho J_0(\frac{r_m}{a}\rho) f(\rho) d\rho. \tag{2.29}$$

Transient

We employ the separation of variables again to solve (2.11a),

$$\hat{u}(\rho, z, t) = P(\rho) Z(z) T(t), \tag{2.30}$$

where P, Z, T are functions of ρ, z, t respectively. Following the same procedure as the steady-state part, and defining μ, ν and λ as eigenvalues for P, Z and T respectively, we arrive at the following ODEs:

$$\rho P'' + P' + \mu^2 \rho P = 0 \tag{2.31}$$

$$Z'' - \nu^2 Z = 0 \tag{2.32}$$

$$T' + \kappa\lambda^2\, T = 0, \tag{2.33}$$

where $\nu^2 = \mu^2 - \lambda^2$. Taking account of (2.30), the boundary conditions (2.11c) to (2.11f), result as

$$P(a) = 0 \tag{2.34}$$

$$P'(0) = 0 \tag{2.35}$$

$$Z'(b) = 0 \tag{2.36}$$

$$Z'(0) = 0. \tag{2.37}$$

The solutions of (2.31), (2.32) and (2.33) are given by

$$P = c_1 J_0(\mu\rho) + c_2 Y_0(\mu\rho) \tag{2.38}$$

$$Z = c_3 \cosh\nu(b-z) + c_4 \sinh\nu(b-z) \tag{2.39}$$

$$T = c_5 e^{-\kappa\lambda^2 t}. \tag{2.40}$$

From the boundedness condition at $\rho = 0$ expressed by (2.35), we must have $c_2 = 0$. Thus the solution of (2.38) becomes

$$P(\rho) = c_1\ J_0(\mu\rho). \tag{2.41}$$

From the boundary condition (2.36) we have

$$Z'(b) = -\nu c_4 = 0$$

which implies $c_4 = 0$, so the solution (2.39) becomes

$$Z(z) = c_3\ \cosh\nu(b-z). \tag{2.42}$$

From boundary condition (2.34), we can determine μ.

$$P(a) = c_1\ J_0(\mu a) = 0 \tag{2.43}$$

so we have

$$\mu_m = \frac{r_m}{a} \tag{2.44}$$

where $r_m (m = 1, 2, 3, \cdots)$ is the mth positive root of $J_0(x) = 0$. A solution of (2.31) satisfying the boundary conditions is

$$P_m(\rho) = c_1 \; J_0(\frac{r_m}{a}\rho) \tag{2.45}$$

where $m = 1, 2, 3, \cdots$. From the boundary condition (2.37), we can determine ν. We have

$$Z'(0) = -\nu c_3 \sinh \nu b = 0,$$

which can be satisfied only if $\sinh \nu b = 0$ or

$$\nu = \frac{k\pi i}{b} \qquad k = 0, 1, 2, \cdots . \tag{2.46}$$

Using (2.46) in (2.42), and considering the fact that

$$\cosh ix = \cos x,$$

then, the solution (2.39) becomes

$$Z_k(z) = c_3 \; \cos \frac{k\pi}{b}(b - z). \tag{2.47}$$

Now from (2.46) and (2.44), it follows that

$$\lambda^2 = \mu^2 - \nu^2 = (\frac{r_m}{a})^2 - (\frac{k\pi i}{b})^2 = \frac{r_m^2}{a^2} + \frac{k^2\pi^2}{b^2}. \tag{2.48}$$

So a solution satisfying all boundary conditions is given by

$$\hat{u}(\rho, z, t) = A \, e^{-\kappa(\frac{r_m^2}{a^2} + \frac{k^2\pi^2}{b^2})t} \; J_0(\frac{r_m}{a}\rho) \; \cos \frac{k\pi}{b}(b - z) \tag{2.49}$$

where $A = c_1 c_3 c_5$, $k = 0, 1, 2, 3, \cdots$ and $m = 1, 2, 3, \cdots$. Replacing A with A_{km} and summing over k and m, we obtain the solution by the superposition principle

$$\hat{u}(\rho, z, t) = \sum_{k=0}^{\infty} \sum_{m=1}^{\infty} A_{km} \, e^{-\kappa(\frac{r_m^2}{a^2} + \frac{k^2\pi^2}{b^2})t} \; J_0(\frac{r_m}{a}\rho) \; \cos \frac{k\pi}{b}(b - z). \tag{2.50}$$

From the initial condition (2.11b), general solution (2.9) and (2.50), we have

$$\left\{ \sum_{k=0}^{\infty} \sum_{m=1}^{\infty} A_{km} \, J_0(\frac{r_m}{a}\rho) \; \cos \frac{k\pi}{b}(b - z) \right\} = u_0(\rho, z) - \bar{u}(\rho, z). \tag{2.51}$$

Using (2.50) in (2.51), we have

$$\begin{aligned} \sum_{k=0}^{\infty} \sum_{m=1}^{\infty} A_{km} \, J_0(\frac{r_m}{a}\rho) \; \cos \frac{k\pi}{b}(b - z) &= (u_0(\rho, z) - T_w) \\ &+ \sum_{m=1}^{\infty} -A_m J_0(\frac{r_m}{a}\rho) \cosh \frac{r_m}{a}(b - z) \end{aligned} \tag{2.52}$$

where A_m is defined by (2.29). To simplify the equation, without loss of accuracy, we consider that $u_0(\rho, z) = T_w$ which is a reasonable assumption, because we start the experiment when the system is in a uniform temperature distribution. Then (2.52) becomes

$$\sum_{m=1}^{\infty} \left\{ \sum_{k=0}^{\infty} A_{km} \cos \frac{k\pi}{b}(b-z) \right\} J_0(\frac{r_m}{a}\rho) = \sum_{m=1}^{\infty} \left\{ -A_m \cosh \frac{r_m}{a}(b-z) \right\} J_0(\frac{r_m}{a}\rho). \tag{2.53}$$

Clearly, because of the orthogonality of the Bessel functions, the coefficients of the two sides of (2.53) must be equal, i.e,

$$\sum_{k=0}^{\infty} A_{km} \cos \frac{k\pi}{b}(b-z) = -A_m \cosh \frac{r_m}{a}(b-z). \tag{2.54}$$

Equation (2.54) can be written in standard form as follows:

$$A_{0m} + \sum_{k=1}^{\infty} A_{km} \cos \frac{k\pi}{b}(b-z) = -A_m \cosh \frac{r_m}{a}(b-z). \tag{2.55}$$

Recalling the *Fourier cosine series expansion* [19], the left side of (2.55) is the Fourier cosine series expansion of the right side with respect to $b-z$. Thus, by substituting $b-z$ with x and replacing A_{0m} and A_{km} with $\frac{a_0}{2}$ and a_k respectively, we have

$$\frac{a_0}{2} + \sum_{k=1}^{\infty} a_k \cos \frac{k\pi}{b}x = -A_m \cosh \frac{r_m}{a}x. \tag{2.56}$$

The coefficients a_k, for $k = 0, 1, 2, \cdots$ are given by

$$a_k = \frac{2}{b} \int_0^b \left(-A_m \cosh \frac{r_m}{a}x \right) \cos \frac{k\pi}{b}x \, dz. \tag{2.57}$$

Equation (2.57) can be written as

$$a_k = -\frac{2}{b} A_m \int_0^b \cosh \frac{r_m}{a}x \ \cos \frac{k\pi}{b}x \, dz, \tag{2.58}$$

and solving the integral we have

$$a_k = -\frac{2}{b} A_m \frac{ab}{a^2k^2\pi^2 + b^2{r_m}^2} \Big(ak\pi \cosh(\frac{r_m}{a}b) \sin(k\pi) + br_m \cos(k\pi) \sinh(\frac{r_m}{a}b) \Big). \tag{2.59}$$

Since k takes only positive integers, we can simplify (2.59) and arrive to

$$a_k = 2\, A_m \frac{r_m}{a\, b} \frac{(-1)^{k+1}}{\frac{{r_m}^2}{a^2} + \frac{k^2\pi^2}{b^2}} \sinh(\frac{r_m}{a}b). \tag{2.60}$$

Thus we have

$$A_{0m} = \frac{a_0}{2} = -A_m \frac{a}{b\, r_m} \sinh(\frac{r_m}{a} b), \tag{2.61}$$

and A_{km} is defined by (2.60) as

$$A_{km} = a_k = 2\, A_m \frac{r_m}{a\, b} \frac{(-1)^{k+1}}{\frac{{r_m}^2}{a^2} + \frac{k^2\pi^2}{b^2}} \sinh(\frac{r_m}{a} b), \tag{2.62}$$

where $k = 1, 2, \cdots$. Hence, it follows that the complete solution to the problem is given by (2.9), (2.26) and (2.50), where their coefficients are defined by (2.29), (2.61) and (2.62).

PDE Model Including Heater Configuration

In the previous section, we calculated the general solution to the Initial-Boundary PDE problem describing the PCR microchip. The general solution, (2.9), is given as the summation of the steady-state, (2.26), and the transient part, (2.50), of the heat distribution inside the PCR microchip. The solutions (2.26) and (2.50) are in the form of the infinite series where their coefficients are given by (2.29), (2.61) and (2.62).

The effect of heat flux transferred from the heater to the system is present as $f(\rho)$ in (2.29), the definition of A_m. According to what we chose in the model configuration, the definition of $f(\rho)$ is given by

$$f(\rho) = \begin{cases} \frac{q}{K} & \text{if} \quad k_1 < \rho < (k_1 + k_2) \\ 0 & \text{otherwise,} \end{cases} \tag{2.63}$$

with

$$\begin{aligned} 0 < (k_1, k_2) \leq a \\ 0 < k_1 + k_2 \leq a, \end{aligned} \tag{2.64}$$

where q is the heat flux from the heater to the chip and K is the thermal conductivity. For discontinuities, we have $f(k_1) = f(k_1 + k_2) = \frac{q}{2K}$.

Using the definition of $f(\rho)$, (2.63) and (2.63), in (2.29), for the A_m we can write

$$A_m = \frac{2\, q}{a\, K\, r_m \sinh(\frac{r_m\, b}{a})\, J_1^2(r_m)} \int_{k_1}^{k_1+k_2} \rho J_0(\frac{r_m}{a}\rho) d\rho. \tag{2.65}$$

We have the following equation for q,

$$q = \frac{P}{A}, \tag{2.66}$$

where P is the amount of the power transferred from the heater to the chip and A is the area of the heater which can be calculated as

$$\begin{aligned} A &= \pi(k_1+k_2)^2 - \pi k_1^2 \\ &= \pi k_2(2k_1+k_2) \end{aligned}$$

Recalling the *Recurrence Relations* for the Bessel function [19], we have

$$\frac{d}{dx}\left[x^n J_n(x)\right] = x^n J_{n-1}(x) \qquad (n = 1, 2, \cdots). \tag{2.67}$$

Equation (2.67) can be written as follows:

$$\int x^n J_{n-1}(x)dx = x^n J_n(x) + c \qquad (n = 1, 2, \cdots). \tag{2.68}$$

By setting $n = 1$ in (2.68), we obtain

$$\int x J_0(x)dx = x J_1(x) + c. \tag{2.69}$$

Using a change of variable, $x = \frac{r_m}{a}\rho$, for the integral part of the A_m in (2.29), we can write

$$\int_{k_1}^{k_1+k_2} \rho J_0(\frac{r_m}{a}\rho)d\rho = \left(\frac{a}{r_m}\right)^2 \int_{\frac{r_m}{a}k_1}^{\frac{r_m}{a}(k_1+k_2)} x J_0(x)dx. \tag{2.70}$$

Using (2.69) in (2.70) we get

$$\int_{k_1}^{k_1+k_2} \rho J_0(\frac{r_m}{a}\rho)d\rho = \left(\frac{a}{r_m}\right)^2 \left[x J_1(x)\right]\Big|_{\frac{r_m}{a}k_1}^{\frac{r_m}{a}(k_1+k_2)}, \tag{2.71}$$

which is calculated as,

$$\int_{k_1}^{k_1+k_2} \rho J_0(\frac{r_m}{a}\rho)d\rho = \frac{a}{r_m}\left((k_1+k_2)J_1(\frac{r_m}{a}(k_1+k_2)) - k_1 J_1(\frac{r_m}{a}k_1)\right). \tag{2.72}$$

Using (2.66) and (2.72) in (2.29), we arrive at the following equation for A_m

$$A_m = \frac{2\,P\,\left((k_1+k_2)J_1(\frac{r_m}{a}(k_1+k_2)) - k_1 J_1(\frac{r_m}{a}k_1)\right)}{\pi k_2(2k_1+k_2)K\; r_m^2\; \sinh(\frac{r_m\, b}{a})\; J_1^2(r_m)}. \tag{2.73}$$

The value of the parameters and constants introduced in our model of the chosen microchip are listed in Table 2.1 [1]. We assume $T_w = 22°\mathrm{C}$ and that an input power of one Watt is being applied to the heater in our simulations.

[1] These parameters are flexible and their values depends on the chosen portion of the real microchip. In section 2.5 we will optimize these parameters to get the least error in simplification

Table 2.1: Parameter Values of the simplified PCR microchip model

Parameter	Symbol	Value	Unit
Cylindrical portion radius[1]	a	3.5	mm
Cylindrical portion thickness[1]	b	1.1	mm
Heater power[1]	P	1	W
Inner radius of heater	k_1	2.3	mm
Heater trace width	k_2	200	μ m
Thermal conductivity of Borofloat glass	K	1.11	W/ (m.K)
Density of Borofloat glass	$\overline{\rho}$	2200	Kg/ m^3
Thermal capacity of Borofloat glass	$\mathcal{C}$	830	J/ K

Finally, we summarize that the solution of the heat equation for our configuration is given by

$$\boxed{u(\rho,z,t) = u_{tr}(\rho,z,t) + u_{ss}(\rho,z)} \tag{2.74}$$

where $u_{tr}(\rho,z,t)$ and $u_{ss}(\rho,z)$ are transient and steady-state responses respectively, given by

$$\boxed{u_{tr}(\rho,z,t) = \sum_{m=1}^{\infty}\sum_{k=0}^{\infty}\left(A_{km}\, e^{-\kappa(\frac{r_m^2}{a^2}+\frac{k^2\pi^2}{b^2})\,t}\; J_0(\frac{r_m}{a}\rho)\;\cos\frac{k\pi}{b}(b-z)\right)} \tag{2.75}$$

and

$$\boxed{u_{ss}(\rho,z) = T_w + \sum_{m=1}^{\infty} A_m J_0(\frac{r_m}{a}\rho)\cosh\frac{r_m}{a}(b-z)} \tag{2.76}$$

where $r_m (m = 1, 2, 3, \cdots)$ is the mth positive root of $J_0(x) = 0$. The coefficients A_{0m}, A_{km} and A_m are defined by

$$\boxed{A_{0m} = -A_m\,\frac{a}{b\,r_m}\;\sinh(\frac{r_m}{a}b)} \tag{2.77}$$

$$\boxed{A_{km} = 2\,A_m\,\frac{r_m}{a\,b}\,\frac{(-1)^{k+1}}{\frac{r_m{}^2}{a^2}+\frac{k^2\pi^2}{b^2}}\sinh(\frac{r_m}{a}b)} \tag{2.78}$$

and

$$\boxed{A_m = \frac{2\,P\;\left((k_1+k_2)J_1(\frac{r_m}{a}(k_1+k_2)) - k_1 J_1(\frac{r_m}{a}k_1)\right)}{\pi k_2(2k_1+k_2)K\;r_m^2\;\sinh(\frac{r_m\,b}{a})\;J_1^2(r_m)}} \tag{2.79}$$

2.4.2 Model Verification

In this section, we verify the solution (2.74)-(2.79) which we calculated for the PDE model (2.1) subject to initial and boundary conditions (2.4)-(2.8) by comparing it to

the FEM simulations for both steady-state and transient responses. The FEM simulations are performed by choosing very fine meshes in the COMSOL Multiphysics software package.

Choosing a Limit for Calculating Infinite Series

For the numerical calculation of (2.76) and (2.75), it is necessary to choose a limit for the infinite series calculation. Choosing a limitation for the m and k values means that we want to use finite sets of eigenvalues and eigenfunctions to approximate (2.76) and (2.75), which are the infinite dimensional equations. These series are in the form of the Bessel and Fourier series with respect to the ρ and z variables, and will converge to the actual response at infinity.

To evaluate the Bessel function approximation and to choose a suitable finite series approximation limit, we calculate and plot the Bessel function expansion of $f(\rho)$ in (2.72) which is used in the calculation of Am coefficients. Recalling (2.28):

$$\sum_{m=1}^{\infty} \left(A_m \frac{r_m}{a} \sinh \frac{r_m\, b}{a} \right) J_0(\frac{r_m}{a}\rho) = f(\rho), \tag{2.80}$$

replacing the term enclosed in the parenthesis with a coefficient, say B_m, we have:

$$\sum_{m=1}^{\infty} B_m\, J_0(\frac{r_m}{a}\rho) = f(\rho), \tag{2.81}$$

with

$$\begin{aligned} B_m &= A_m \frac{r_m}{a} \sinh \frac{r_m\, b}{a} \\ &= \frac{2}{a^2\, J_1^2(r_m)} \int_0^a \rho J_0(\frac{r_m}{a}\rho) f(\rho) d\rho, \end{aligned} \tag{2.82}$$

which is exactly the Bessel series expansion of $f(\rho)$. Using (2.79), B_m can be found as:

$$B_m = \frac{2\,P\, \left((k_1+k_2) J_1(\frac{r_m}{a}(k_1+k_2)) - k_1 J_1(\frac{r_m}{a}k_1) \right)}{a\,\pi k_2 (2k_1+k_2) K\; r_m\, J_1^2(r_m)}. \tag{2.83}$$

The simulation of the Bessel series expansion for $f(\rho)$ given by (2.83) for different sets of m is depicted in Fig. 2.6. It shows that choosing a maximum value of 500 for m will provide a fair approximation of the heater configuration defined by $f(\rho)$. Choosing values bigger than the selected value will significantly increase the required computational resources in the numerical calculation.

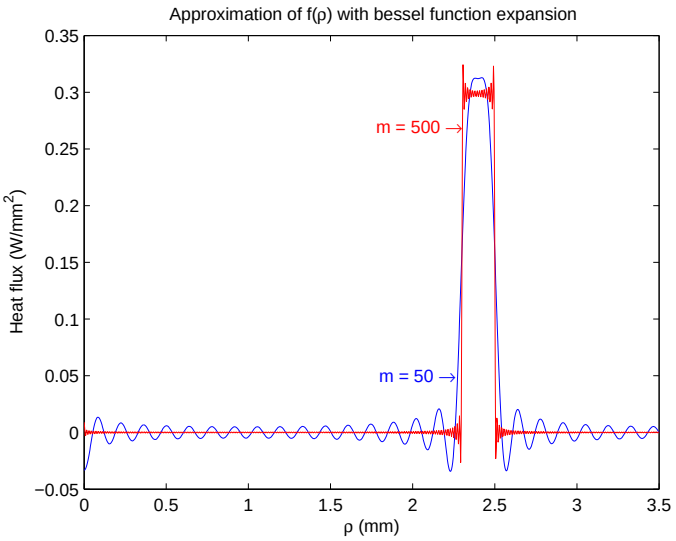

Figure 2.6: Approximation of $f(\rho)$ using Bessel series

To select a limit for k in the infinite sum, we can take a closer look at (2.75). The sum index, k, in (2.75) affects the coefficient A_{km}, the term $\cos\frac{k\pi}{b}(b-z)$, and the time constant $e^{-\kappa(\frac{r_m^2}{a^2}+\frac{k^2\pi^2}{b^2})t}$.

The cosine term, $\cos\frac{k\pi}{b}(b-z)$, takes a value between -1 and 1. The values of the coefficient A_{km} for different values for k and m are calculated and shown in Table 2.2.

Table 2.2: Values of A_{km}

	m_1	m_2	m_3	m_4	m_5
k=1	7.8102	-13.8381	5.3073	5.9620	-9.1475
k=2	-2.0361	4.1947	-1.9550	-2.6446	4.7434
k=3	0.9122	-1.9407	0.9524	1.3721	-2.6317
k=4	-0.5145	1.1075	-0.5543	-0.8198	1.6212
k=5	0.3297	-0.7136	0.3606	0.5403	-1.0854
k=6	-0.2291	0.4974	-0.2527	-0.3813	0.7731
k=7	0.1684	-0.3663	0.1866	0.2829	-0.5769
k=8	-0.1290	0.2808	-0.1434	-0.2180	0.4463
k=9	0.1019	-0.2221	0.1136	0.1731	-0.3551
k=10	-0.0826	0.1800	-0.0922	-0.1406	0.2891

The coefficient A_{km} significantly decreases as k increases. We chose the limit of $k = 30$ in our calculations. Choosing a larger limit for k did not produce a significant change in the simulation results.

Heat Distribution in Steady-State

In this section, we calculate the steady-state heat distribution given by (2.76) inside the domain. Next, we verify the accuracy of the calculation by comparing it with results from the FEM simulation. Heat distribution found by the FEM simulation is depicted as a color map in Fig. 2.7.

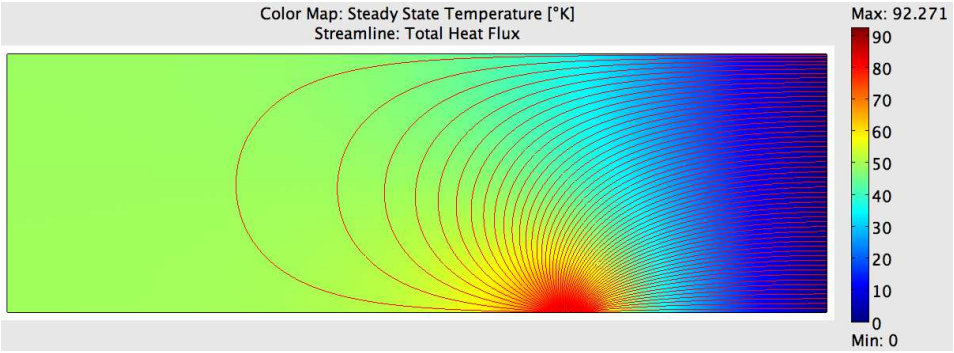

Figure 2.7: Steady-state temperature distribution, FEM Simulation

The next figure, Fig. 2.8, presents the heat distribution that results from calculating the PDE model.

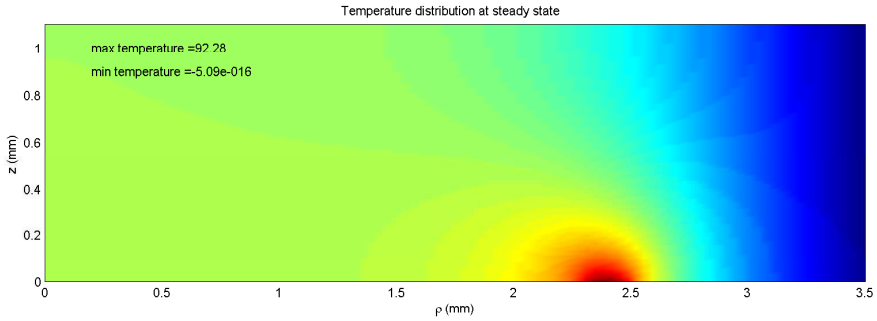

Figure 2.8: Steady-state temperature distribution, PDE simulation

A stencil of 100×100 points is used to calculate the heat distribution in Fig. 2.8.

For a closer comparison, we calculated the temperature profile along the ρ axis for five different vertical distances starting from the base at $z = 0$ up to the top boundary at $z = 1.1mm$. The results of the FEM and the PDE model simulations are depicted in Fig. 2.9a and Fig. 2.9b, respectively.

It can be seen from the figure that there is an excellent match between the two results.

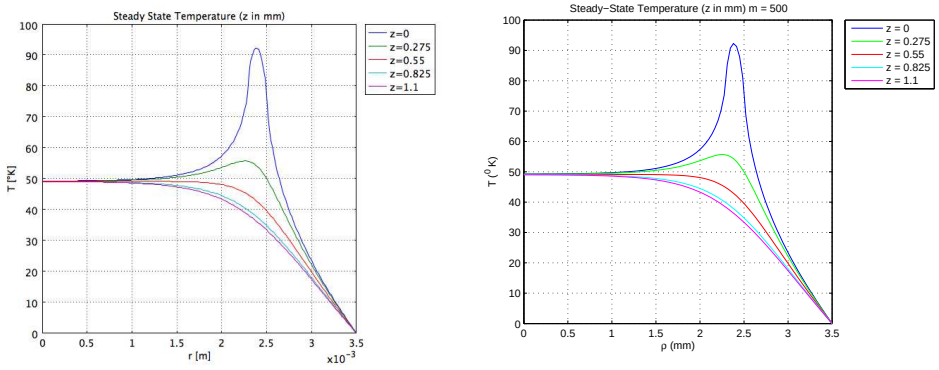

(a) FEM simulation (b) PDE model

Figure 2.9: Steady-state temperature for different z

Transient Temperature Distribution in the PCR Microchip

In this section, we verify the solution of the transient heat-distribution inside the model structure. To do so, we use the same spatial profile presented in Fig. 2.9 and calculate the heat distribution after applying one Watt of power to the heater for the following times: $t = 2.5s$, $t = 5s$, $t = 7.5s$, $t = 10s$, $t = 15s$ and $t = 20s$. We assume that the chip was initially at rest with a temperature of zero degree at $t = 0$. The result of both the FEM and the PDE model simulations are presented in Fig. 2.10a through Fig. 2.15b.

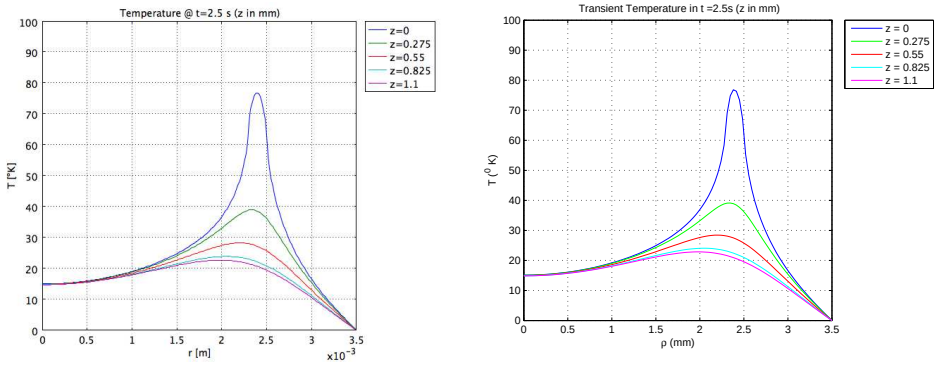

(a) FEM simulation (b) PDE model

Figure 2.10: Temperature at t = 2.5s for five different distances from the base

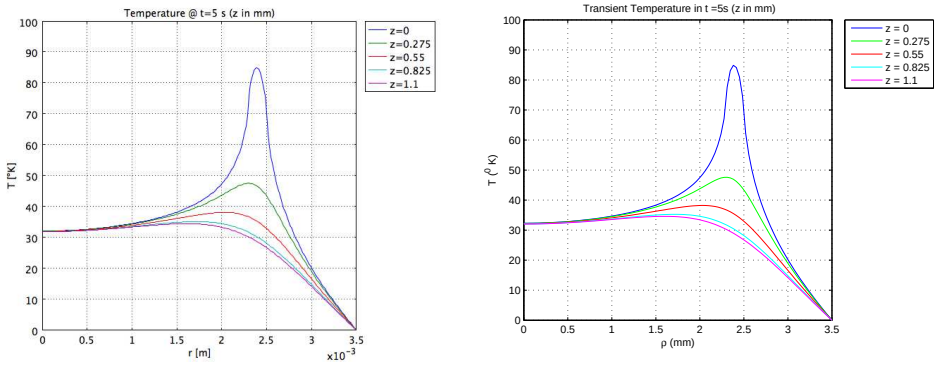

(a) FEM simulation (b) PDE model

Figure 2.11: Temperature at t = 5s for five different distances from the base

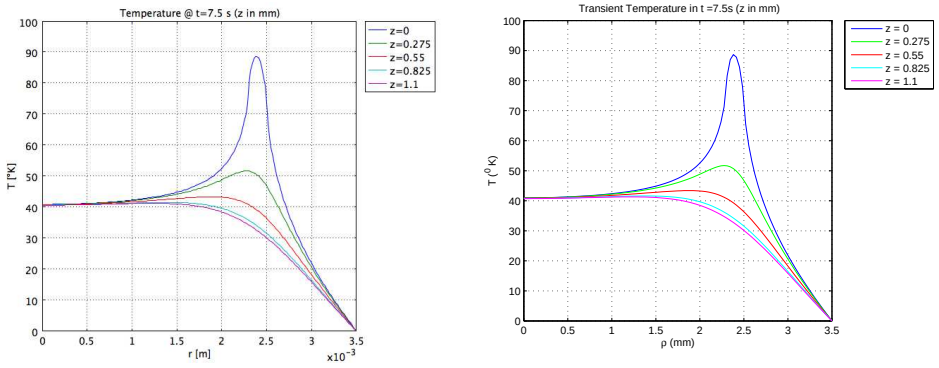

(a) FEM simulation (b) PDE model

Figure 2.12: Temperature at t = 7.5s for five different distances from the base

In another interesting simulation, we calculate the transient temperature for a particular point inside the chip. The chosen spatial point at $\rho = 0$ and $z = 0.55mm$ is located inside the chamber. The results of this simulation, depicted in Fig. 2.16, shows the transient chamber temperature in response to a step input of one Watt.

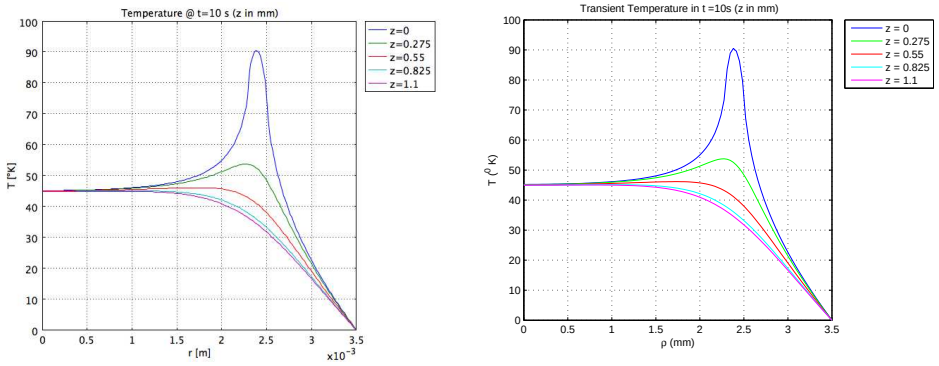

(a) FEM simulation (b) PDE model

Figure 2.13: Temperature at t = 10s for five different distances from the base

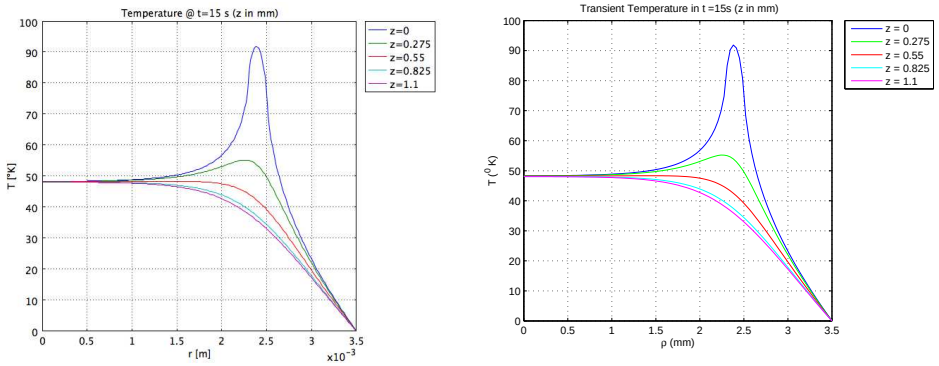

(a) FEM simulation (b) PDE model

Figure 2.14: Temperature at t = 15s for five different distances from the base

Correlation Analysis Between FEM Simulation and PDE Model Simulation Data Sets

A correlation analysis was performed between sets of data resulting from the simulation of the temperature value for a predefined point in the spatial domain. Five and 10 equally distanced points were selected for the z and ρ axes, respectively. Therefore, for every analysis we obtained five sets of data with 10 values in each set. The correlation analysis between the data from the PDE model calculation and the data from the FEM simulation provided a 1 by 5 vector according to each chosen z. The analysis was repeated for both the steady-state and the transient responses. The results are given in Table 2.3.

The FEM and PDE model simulation results are strongly correlated. Upon further inspection, the difference between the temperature found by both methods

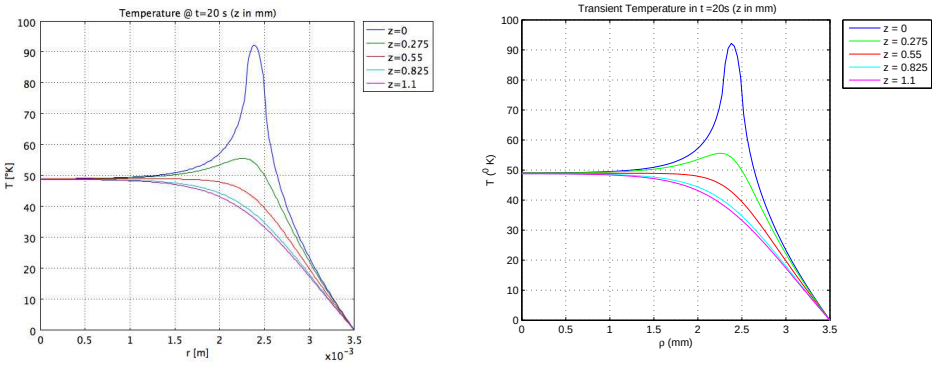

(a) FEM simulation (b) PDE model

Figure 2.15: Temperature at t = 20s for five different distances from the base

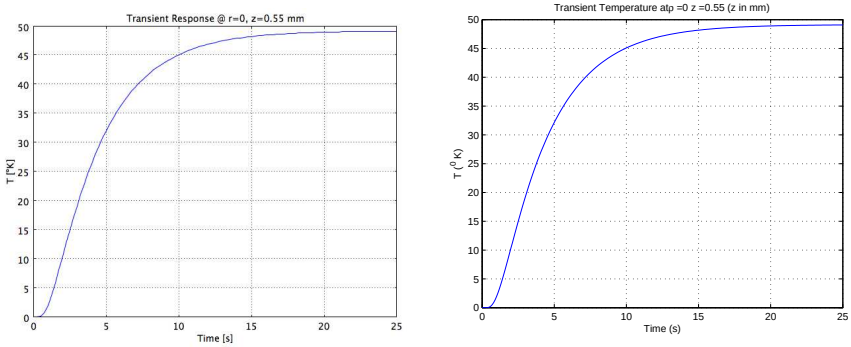

(a) FEM simulation (b) PDE model

Figure 2.16: Transient temperature at the spatial point $\rho = 0$, $z = 0.55$mm

was calculated and is given in Table 2.4. The same spatial points used for the correlation analysis are used again and the maximum absolute value of difference between each set of data from the FEM and PDE model simulations was calculated.

The maximum absolute difference of about 0.2°C in Table 2.4 verifies the validity of the PDE model solution.

Table 2.3: Correlation Analysis

	$z = 0$mm	$z = 0.275$mm	$z = 0.55$mm	$z = 0.825$mm	$z = 1.1$mm
$t = 2.5$s	1.0000	1.0000	1.0000	1.0000	1.0000
$t = 5$s	1.0000	1.0000	1.0000	1.0000	1.0000
$t = 7.5$s	1.0000	1.0000	1.0000	1.0000	1.0000
$t = 10$s	1.0000	1.0000	1.0000	1.0000	1.0000
$t = 15$s	1.0000	1.0000	1.0000	1.0000	1.0000
$t = 20$s	1.0000	1.0000	1.0000	1.0000	1.0000
$t = \infty$	1.0000	1.0000	1.0000	1.0000	1.0000

Table 2.4: Maximum Absolute Difference

	$z = 0$mm	$z = 0.275$mm	$z = 0.55$mm	$z = 0.825$mm	$z = 1.1$mm
$t = 2.5$s	0.1772	0.1764	0.1763	0.1763	0.1762
$t = 5$s	0.1939	0.1737	0.1737	0.1737	0.1737
$t = 7.5$s	0.1067	0.0865	0.0865	0.0865	0.0865
$t = 10$s	0.0624	0.0423	0.0423	0.0423	0.0423
$t = 15$s	0.0302	0.0101	0.0101	0.0101	0.0101
$t = 20$s	0.0225	0.0024	0.0024	0.0024	0.0024
$t = \infty$	0.0201	0.0000	0.0000	0.0000	0.0000

2.5 Optimization of the PDE Model

In the previous section, we verified the accuracy of the analytical solution derived for the introduced model structure. The proposed model has a simplified domain structure which simplifies the analytical solution, however, it is still a simplified model of the whole PCR microchip structure. Here, the question is, how well does this model represent the heat distribution in the area of interest of the actual PCR microchip?

To answer this question, we investigate the accuracy of the derived analytical model by comparing its results with the heat distribution in an actual PCR microchip (calculated by extensive FEM simulations). In addition, we look for options to improve this accuracy as much as possible. We calculate the effect of the variation within the parameters of the analytical model on the model fitting accuracy resulting by comparing the analytical model with the FEM simulation of an actual PCR microchip. Next, we propose an optimization problem targeting the optimization of the parameters of the analytical model. This is done to arrive at the best fit between the analytical model and the actual PCR microchip. We pay special attention to

heat distribution in the chamber area where an accuracy of $\pm 1°C$ is required for a successful PCR experiment.

The analytical model consists of a cylindrical glass domain with carefully selected boundary conditions. These conditions resemble the heat distribution in a cylindrical domain inside the PCR chip where the chamber is located. To prevent multi-domain structure, the presence of the PDMS layer, bottom glass layer, heatsink, the property of the chamber and heat convection at the upper surface are not considered in the simplified analytical model. These simplifications in the analytical model can result in a significant approximation error of the heat distribution inside the actual chip.

Heat distribution in the actual model was provided by precise FEM simulation using the COMSOL Multiphysics software package. Here and afterwards we will call the actual PCR microchip the FEM model and the analytical model the PDE model. Because of axisymmetric structure of both models, we need only to compare the heat distribution in a half cut side view of the chip. Fig. 2.17 and Fig. 2.18 depict the heat distribution in the FEM and PDE model, respectively, after applying one Watt of power to the heater.

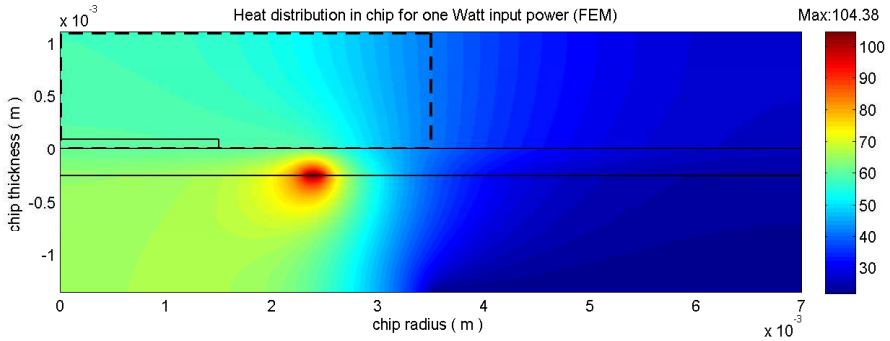

Figure 2.17: Heat distribution in PCR chip (FEM model)

The selected portion for comparing these two models is enclosed by dash lines. The radius of the portion is optimized to obtain an approximately constant temperature in the portion's right side in the FEM model. The chamber is located in the bottom left corner of the selected portion.

We define area error,$e_{ap}(\rho, z)$, as the difference between the temperature in the PDE model and the temperature in the FEM model in any given point at the selected

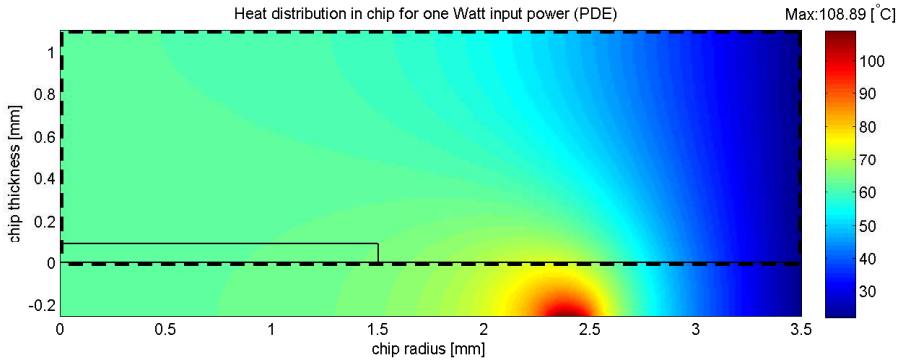

Figure 2.18: Heat distribution in simplified chip (PDE model)

portion, as follows:

$$e_{ap}(\rho, z) = u_{PDE}(\rho, \bar{z}) - u_{FEM}(\rho, z) \quad , \quad \rho, z \in \mathcal{D}_1,\ \bar{z} = z + 254\mu m$$

where $\mathcal{D}_1 = \{\rho, z : 0 \leq \rho \leq 3.5mm, 0 \leq z \leq 1.1mm\}$ describes the selected portion. Next, we define the chamber error, $e_{ch}(\rho, z)$, as the difference of the temperature in the chamber area between the PDE model and the FEM model, as follows:

$$e_{ch}(\rho, z) = u_{PDE}(\rho, \bar{z}) - u_{FEM}(\rho, z) \quad , \quad \rho, z \in \mathcal{D}_2,\ \bar{z} = z + 254\mu m$$

where $\mathcal{D}_2 = \{\rho, z : 0 \leq \rho \leq 1.5mm, 0 \leq z \leq 90\mu m\}$ describes the chamber location. We calculated the values of e_{ap} and e_{ch} when one Watt input was applied to the heater in both models. We depicted the results in Fig. 2.19 and Fig. 2.20 respectively.

To obtain a quantitative measure of the error in the selected portion, we defined the following parameters:

- Absolute average error in portion: $\bar{e}_{ap} \doteq |\frac{1}{A_1} \int_{A_1} e_{ap} dA_1|$
- Maximum absolute error in portion: $|e_{ap}|_{max} \doteq max|e_{ap}(\rho, z)|$
- Uniformity of error in portion: $U_{ap} \doteq max(e_{ap}(\rho, z)) - min(e_{ap}(\rho, z))$

where $\rho, z \in \mathcal{D}_1$ and A_1 is the area of the portion specified by $\mathcal{D}_1$. The values of the defined measures for a system after applying a power of one Watt to the heater are calculated and presented in Table 2.5.

Now we focus on the chamber area, which is critically important in our analysis. Fig. 2.20 shows the error between the PDE model and the FEM model in the chamber area when one Watt of input power is applied to the heater.

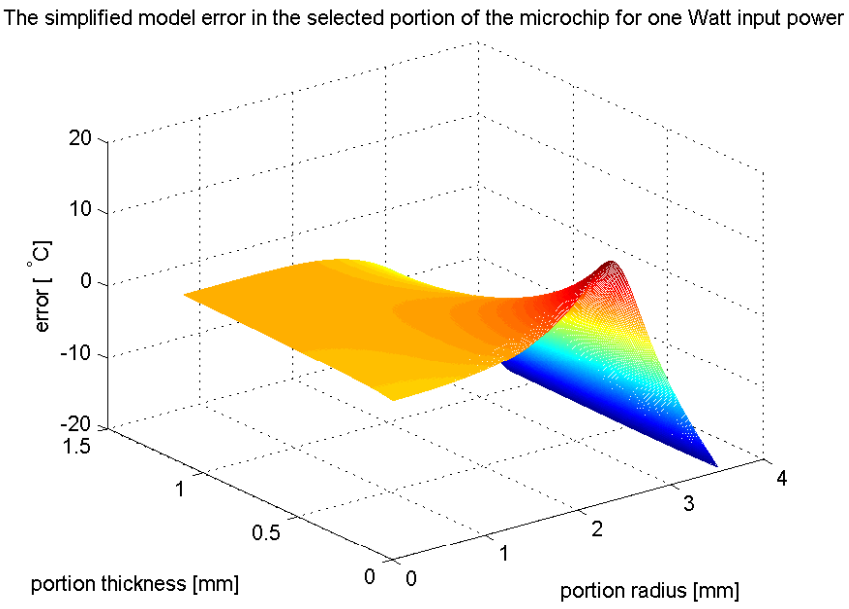

Figure 2.19: The approximation error in the selected portion

Table 2.5: Error measures for Fig. 2.19

Measure	Value
$\bar{e}_{ap}$	0.38° C
$\|e_{ap}\|_{max}$	19.5° C
U_{ap}	32.9° C

We define similar quantitative measures for the error in the chamber area:

- Absolute average error in chamber: $\bar{e}_{ch} \doteq |\frac{1}{A_2} \int_{A_2} e_{ch} dA_2|$
- Maximum absolute error in chamber: $|e_{ch}|_{max} \doteq max|e_{ch}(\rho, z)|$
- Uniformity of error in chamber: $U_{ch} \doteq max(e_{ch}(\rho, z)) - min(e_{ch}(\rho, z))$

where $\rho, z \in \mathcal{D}_2$ and A_2 is the area specified by $\mathcal{D}_2$. Table 2.6 shows the values of these measures after applying one Watt of power to the heater.

Clearly, the resulting error does not satisfy our criteria.

2.5.1 Effect of Variation in the PDE Model Parameters

The heat distribution in the PDE model is affected by the model parameters and change in the model parameters will affect the error measures that we defined. We

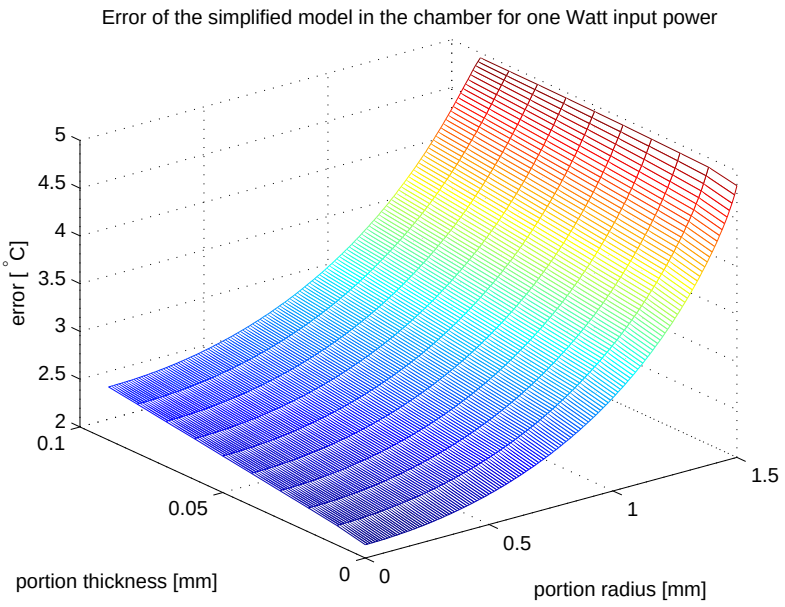

Figure 2.20: Error in the chamber

Table 2.6: Error measures for Fig. 2.20

Measure	Value
$\bar{e}_{ch}$	3.05° C
$\|e_{ch}\|_{max}$	4.9° C
U_{ch}	2.8° C

selected three parameters of the PDE model representing chip thickness, chip radius and input power as the manipulated variables. These variables and their notations are listed in Table 2.7.

We are interested in seeing how our quantitative error measures are effected by changes in the manipulated parameters defined in Table 2.7.

The effect of variations in chip thickness, b, on the absolute average error and the uniformity measures for both the selected portion and chamber area are shown in Fig. 2.21.

As can be seen, the uniformity measure passes a minimum when chip thickness changes between 2mm and 2.4mm , but the location where the least amount of changes occurs differs for the areas of interest where we defined our measures.

Fig. 2.22 shows the effect of changing the chip radius, a, on the absolute average

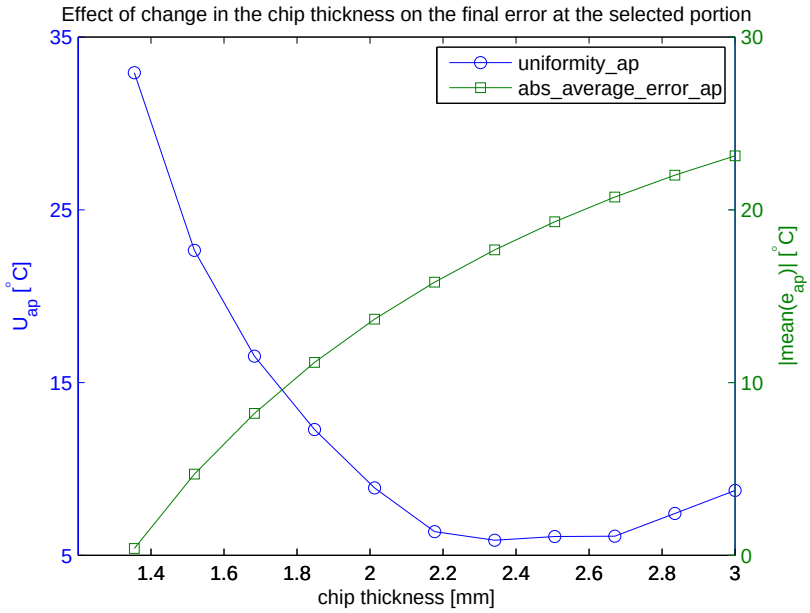

(a) portion

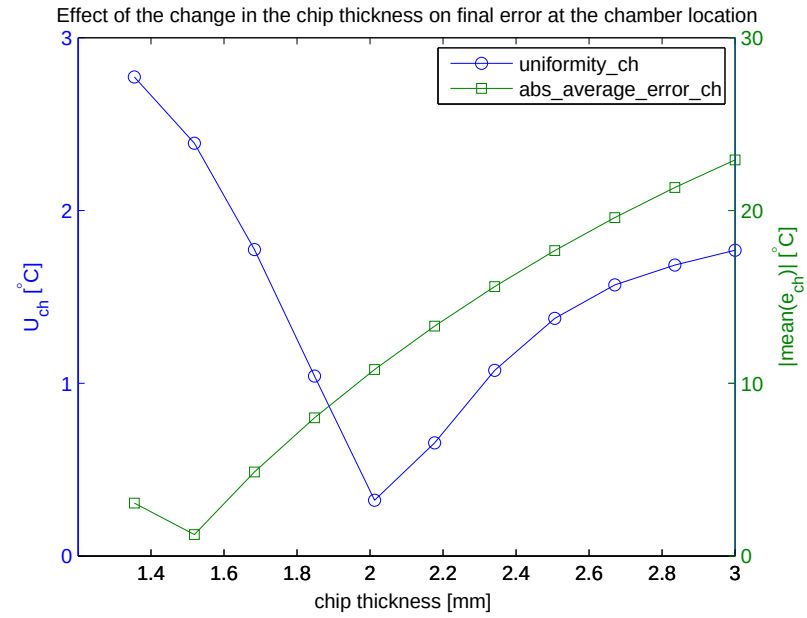

(b) chamber

Figure 2.21: Effect of changing chip thickness

Table 2.7: Manipulated variables for PDE model

Parameter	Description
a	chip radius
b	chip thickness
P	input power

error and uniformity measures for both the selected portion and chamber area. An exponential trend in relation between the error uniformity and the chip radius can be seen in both the selected portion and chamber area.

The graphs in Fig. 2.23, show how changing input power affects the absolute average error and the uniformity measures in both the selected portion and the chamber area.

2.5.2 Optimization

Problem Formulation

In this section, we formulate the problem of finding proper values for the manipulating variables to obtain acceptable error measures in the form of a standard optimization problem. We define a weighted-sum objective function including the $\mathbb{L}_2$ norm of the error at the chamber location, the uniformity measure at the chamber location and the uniformity measure at the selected portion as follows:

$$J = w_1 \frac{1}{A_2} \int_{A_2} {e_{ch}}^2 dA_2 + w_2 U_{ch} + w_3 U_{ap}, \tag{2.84}$$

where w_1, w_2 and w_3 are the weight coefficients. Next, we define a set, $\mathbf{S}$, representing the lower bands and upper bands of the manipulating variables as follows:

$$\mathbf{S} = \{a, b, P : a, b, P \in \mathbb{R}, 0.0035 \leq a \leq 0.007,\ 0.0013 \leq b \leq 0.004,\ 0.1 \leq P \leq 2.5\}. \tag{2.85}$$

Optimization Results

We use MATLAB to solve the optimization problem defined by (2.84) and (2.85). After comparing the results of optimization with different values of the weighting coefficients, a good selection for w_1, w_2 and w_3 can be obtained. We obtained the

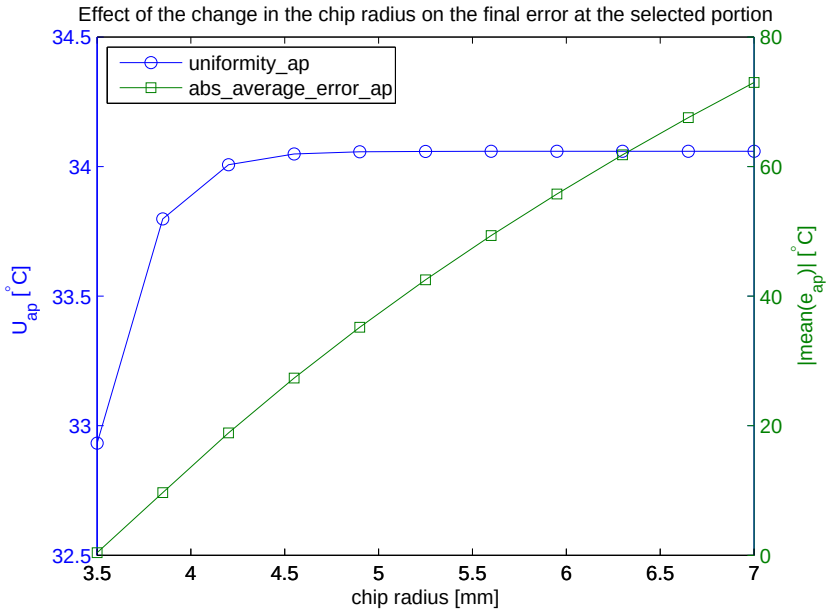

(a) portion

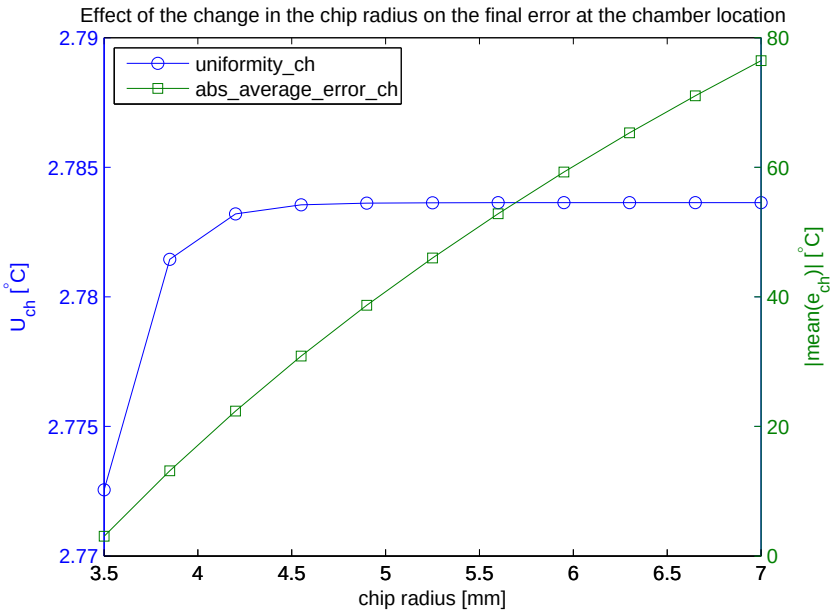

(b) chamber

Figure 2.22: Effect of changing chip radius

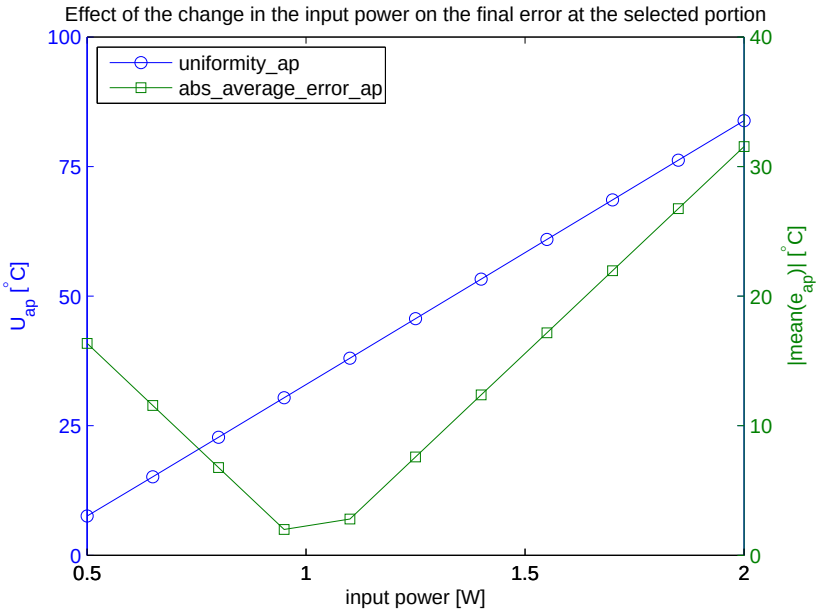

(a) portion

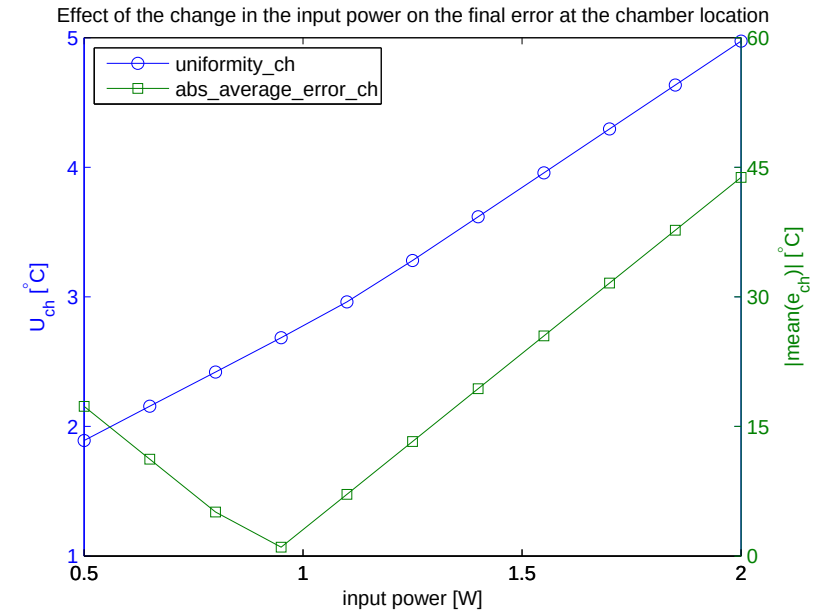

(b) chamber

Figure 2.23: Effect of changing heater power

best results by choosing weighting coefficients as $w_1 = 10$, $w_2 = 1$ and $w_3 = 0.1$. Optimized values for the manipulated variables are given in Table 2.8.

Table 2.8: Optimized parameter for PDE model

Parameter	Description	optimized value
a	chip radius	$4.9362mm$
b	chip thickness	$2.1015mm$
P	input power	$0.76981Watt$

By using the optimized parameters in the PDE model, we expect to get smaller error measures. Table 2.9 shows the amount of the error measures after employing optimized parameters.

Table 2.9: Error measures for optimized PDE model

Measure	Value in optimized system	Value in not optimized system
$\bar{e}_{ch}$	7.7×10^{-6}° C	3.05° C
$\|e_{ch}\|_{max}$	0.14° C	4.9° C
U_{ch}	0.28° C	2.8° C
$\bar{e}_{ap}$	1.14° C	0.38° C
$\|e_{ap}\|_{max}$	3.6° C	19.5° C
U_{ap}	3.7° C	32.9° C

These results show significant improvement in approximating the heat distribution in the actual system. The distribution of the error in the selected portion and the chamber locations for the optimized PDE system are shown in Fig. 2.24 and Fig. 2.25 respectively. According to values of the measures in Table 2.9, this approximation satisfies our criteria of the maximum error of ± 1°C.

Relationship to Input Power

The input power in the simplified model spread into a much smaller structure than the real PCR microchip. In section 2.3, we reasoned that the amount of heat going to the upper portion of the chip through the PDMS and top glass layer has an approximately constant ratio to the total heat being dissipated by the heater. Now the questions are: does the optimization results in the same previous values for the

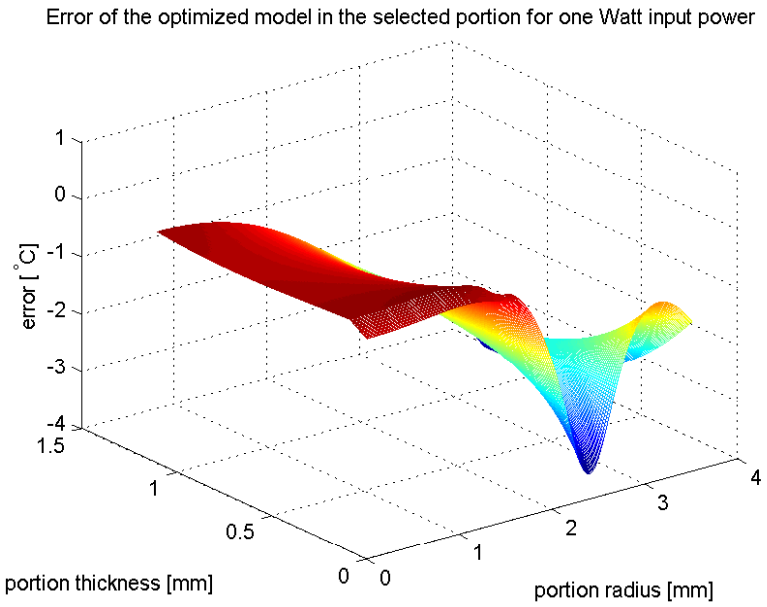

Figure 2.24: Error in selected portion

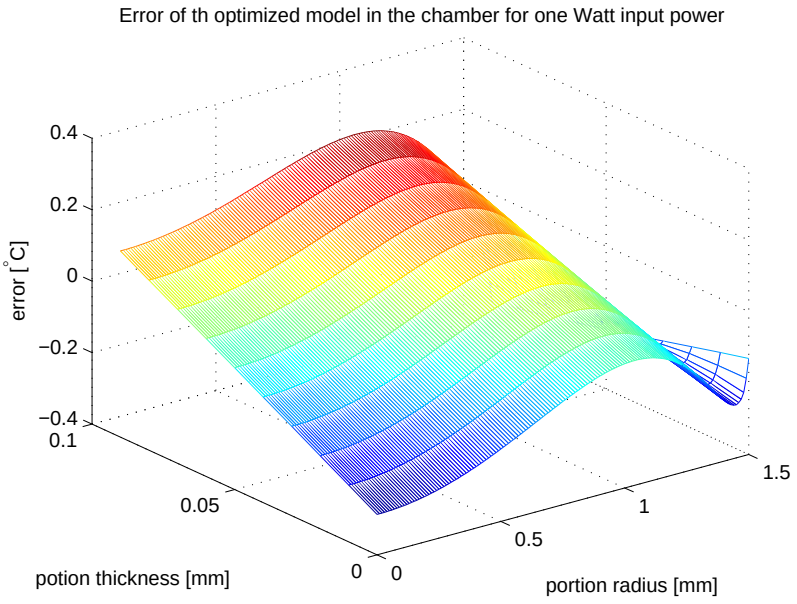

Figure 2.25: Error in chamber

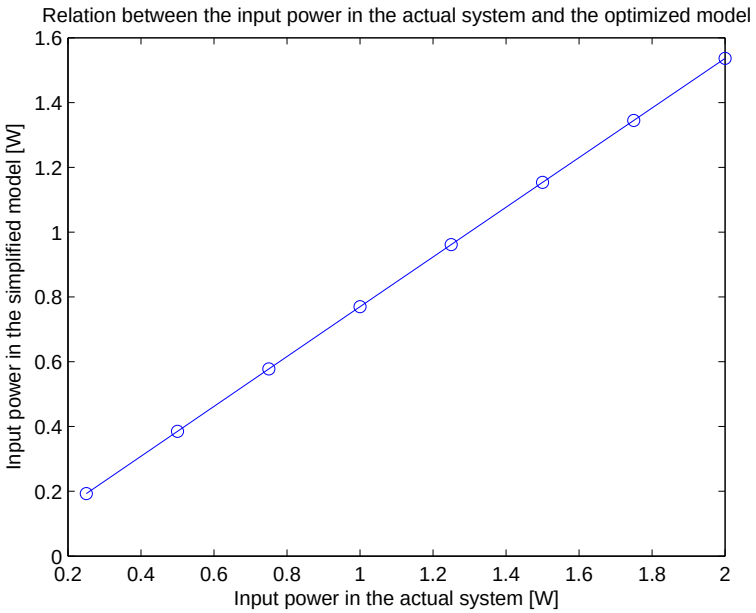

Figure 2.26: Relationship between applied power in actual system and simplified model

chip thickness, b and the chip radius, a, if the input power be altered? and what is the relation between input power in the simplified model to the input power in the real system?

In order to answer these questions, we solve the optimization problem of finding optimum values of chip thickness, b and chip radius, a, separately for a set of eight different input powers ranging from 250mW up to 2W. As we expect, the optimized values for the chip thickness,b, and the chip radius,a, converge to the same amount that we calculated for the input power of one Watt. The only difference in the results is in the optimized values calculated for the input power P in the PDE model.

Therefore, we fix the parameters a and b with the previously obtained optimized values, and initiate another optimization problem to find optimized values of P on eight different data sets calculated by the FEM simulation for the selected input powers. The optimized values for P versus actual input power are depicted in Fig. 2.26.

Clearly, the relationship between the input power in the optimized PDE model and the input power in the FEM model is linear. Using least square approximation,

we approximate this relationship in a compact form using the following equation:

$$P = 0.76772\bar{P} + 1.5595 \times 10^{-3}, \tag{2.86}$$

where $\bar{P}$ is the actual power considered in the FEM simulation and P is the input power considered in the PDE model. Table 2.10 presents the variation in the error measures when we use the optimized values of a and b from Table 2.8 along with the values of P calculated using (2.86). The last three lines of the Table 2.10 confirms that for the whole operational range of the input power, the error in the chamber location would be stay far below the acceptable error of $\pm 1°$C.

Table 2.10: Error measures for the optimized PDE model, complete range

$\bar{P}$	250mW	500mW	750mW	1W	1.25W	1.5W	1.75W	2W
$\bar{e}_{ap}$	0.29	0.57	0.86	1.14	1.43	1.71	1.99	2.27
$\|e_{ap}\|_{max}$	0.89	1.78	2.67	3.56	4.46	5.35	6.25	7.15
U_{ap}	0.92	1.84	2.78	3.70	4.63	5.56	6.49	7.42
$\bar{e}_{ch}$	6.6×10^{-5}	7.8×10^{-5}	1.1×10^{-4}	7.7×10^{-6}	0.0012	0.0012	0.0011	0.0011
$\|e_{ch}\|_{max}$	0.036	0.073	0.109	0.145	0.183	0.222	0.261	0.301
U_{ch}	0.070	0.140	0.209	0.279	0.351	0.423	0.496	0.570

2.6 Summary

The PDE model described by the model structure in Fig. 2.5, with the optimized parameters presented in Table 2.8 and the analytical solution given in (2.74) to (2.79), can be used as an accurate enough approximation of the heat distribution in the PCR microchip. The calculation of the error proves that the error between the optimized mathematical model and the actual system is much less than the amount of the maximum acceptable error of $\pm 1^{\circ}$C in the chamber area.

The heat distribution in the PCR microchip was previously attainable only by calculating the extensive and time consuming FEM simulations defined on the complicated multi-domain structure. The superiority of the obtained PDE model to the FEM model is the fact that is does not need huge amount of the computational resources and as a result it can perform the dynamic simulations in a much shorter time. We conclude that the obtained model not only can be used for the controller design purposes but also it can be used for the analysis of the closed loop system response.

Chapter 3

Observer Design

3.1 Introduction

The observer design problem deals with estimating the states of a dynamical system. For the lumped parameter systems, an observer such as a Luenberger observer [85] can estimate the temporally distributed states, e.g. $x(t)$. On the other hand, a distributed parameter observer is able to estimate states of a distributed parameter system which are distributed both temporally and spatially, e.g. $u(\rho, t)$.

In Chapter 1, we introduced a PCR-LOC microchip which with the addition of a well-designed thermal management system is capable of impacting the healthcare system by offering an inexpensive and portable platform for genetic tests. The main challenge associated with the thermal control problem of the PCR-LOC microchip is the necessity of measuring the PCR chamber temperature, which is necessary for feedback but is out of access for direct measurement. The only available measurement in this system is the temperature of the heater. The governing phenomenon of heat distribution inside the PCR-LOC microchip can be expressed by partial differential equations (PDEs) which naturally leads us to look for a PDE model to describe the dynamics of the heat distribution in the microchip.

In Chapter 2, we constructed a single domain PDE model in a cylindrical coordinate system and verified that our model provides the heat distribution dynamics in an area surrounding the chamber with an acceptable accuracy. Our PDE model features the collocated boundary actuation and sensing architecture, i.e. the heater and the sensor are both located on the same boundary.

In the absence of direct temperature measurement inside the reaction chamber, we turn our attentions to the design of an observer that can provide an estimate of the chamber temperature, based on other variables. We briefly surveyed the observers for distributed parameter systems in Chapter 1. One of the most recent developments in this regard is the PDE backstepping boundary observer introduced by Krstic *et al* [69]. The inspiration for PDE backstepping boundary observer is connected to a work of Krener *et al* [65] in which a backstepping observer is proposed for nonlinear ODE systems. The PDE backstepping observer design process starts with introducing a Luenberger-like observer structure which resembles the PDE formulation of the original system. The next step is to define an integral transformation that takes the observer error system to an exponentially stable system with a desired convergence speed. The observer design problem is to find the observer parameters which are fully achievable after calculating the kernel of the integral transformation. We choose the PDE backstepping boundary observer approach for our design.

The concept of a distributed parameter boundary observer for a thermal system is illustrated in Fig. 3.1. In general, a distributed parameter observer is able to

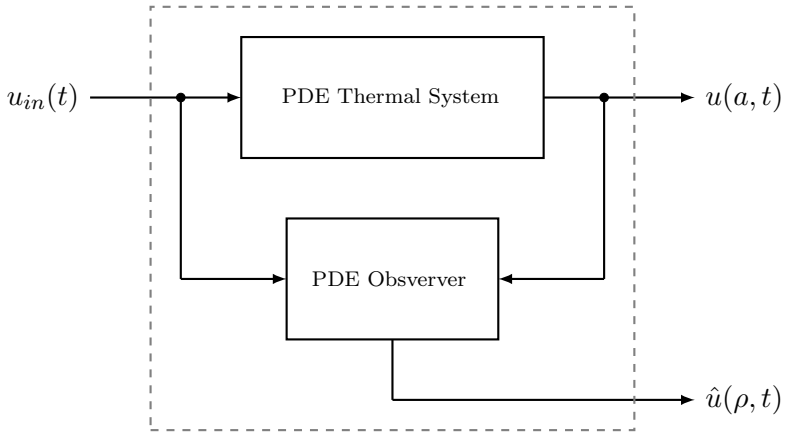

Figure 3.1: Block digram illustration of a distributed parameter observer

estimate all of the distributed states by only reading the inputs and outputs of a PDE system. Those inputs and outputs could be anywhere in the domain or in the boundaries.

In this chapter, we design a PDE backstepping boundary observer for the PCR-LOC microchip described by the PDE model introduced in Chapter 2. The PDE backstepping boundary observer design process can be followed by more refined

mathematical equations if the PDE system is normalized in the first place. Therefore, the first step towards designing the PDE backstepping boundary observer in Section 3.2, is to normalize our model.

In Section 3.3, we design a PDE backstepping boundary observer for our PDE model by extending the standard approach to the 2-D cylindrical coordinate system. However, as we will discuss later in this chapter, the resulting PDE equation for the kernel of the integral transformation describing the observer is very difficult to solve either numerically or analytically.

The novel approach introduced in Section 3.4 is to use classical complex analysis theories to transform the domain of the problem to a new coordinate system where the observer design approach results in a more tractable kernel equation for the integral transformation. To the best of our knowledge, our work is the first demonstration of the application of conformal transformation in the PDE backstepping problem. The design approach in Section 3.5 will complete the observer design.

The block diagram in Fig. 3.2 shows how an observer designed in a transformed and normalized space can be used on the original PDE system.

3.2 Preliminaries

3.2.1 Normalizing the PDE system

Recalling the PCR microchip model introduced in Chapter 2, The following PDE equation describes dynamic heat distribution inside the microchip:

$$\frac{1}{\kappa} v_t(\rho, z, t) = v_{\rho\rho}(\rho, z, t) + \frac{1}{\rho} v_\rho(\rho, z, t) + v_{zz}(\rho, z, t), \tag{3.1}$$

subject to the initial and the boundary conditions given by

$$v(\rho, z, 0) = v_0(\rho, z) \tag{3.2}$$

$$v(a, z, t) = T_w \tag{3.3}$$

$$v_\rho(0, z, t) = 0 \tag{3.4}$$

$$v_z(\rho, b, t) = 0 \tag{3.5}$$

$$v_z(\rho, 0, t) = -f(\rho)\, U(t), \tag{3.6}$$

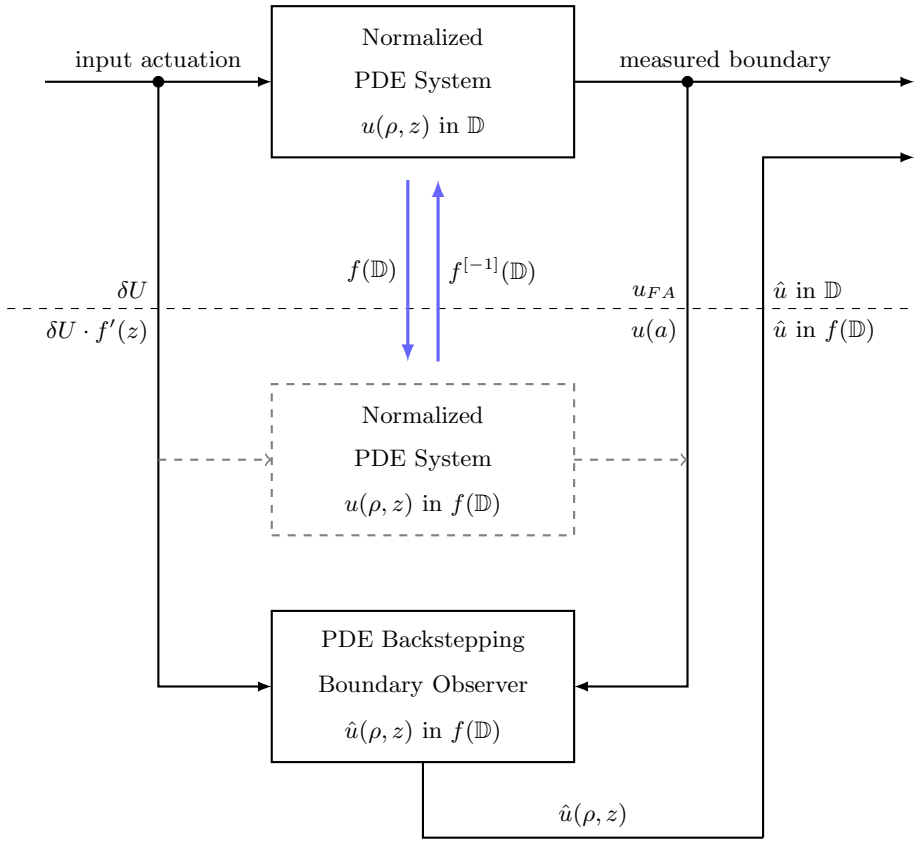

Figure 3.2: Interconnection between the observer designed for the transformed PDE system and the original normalized PDE system

where $v(\rho, z, t)$ is the temperature of every point inside the domain at any given time t, and κ is thermal diffusivity. $v_0(\rho, z)$ is the initial heat distribution and T_w is the temperature of the outside wall of the cylinder (ambient temperature). $f(\rho)$ describes the geometric distribution of the control action signal at the bottom surface which is defined by the heater pattern and location and $U(t)$ is the amount of the external power applied to the heater. ρ and z are limited to $0 \leq \rho \leq a$ and $0 \leq z \leq b$. The geometric distribution of the control action signal, $f(\rho)$, is as follows:

$$f(\rho) = \begin{cases} \frac{q}{K} & \text{if} \quad k_1 < \rho < (k_1 + k_2) \\ \frac{q}{2K} & \text{if} \quad \rho = k_1 \text{ or } \rho = (k_1 + k_2) \\ 0 & \text{otherwise,} \end{cases}$$

where $0 < k_1 \leq a$, $0 < k_2 \leq a$ and $0 < k_1 + k_2 \leq a$.

We start the normalization of the spatial space by scaling ρ and z axes:

$$\begin{aligned} \overline{\rho} &= \frac{\rho}{a} \\ \overline{z} &= \frac{z}{b}. \end{aligned} \tag{3.7}$$

In the scaled spatial space, the PCR model described by (3.1) to (3.6) is written as:

$$\frac{a^2}{\kappa} v_t(\overline{\rho}, \overline{z}, t) = v_{\overline{\rho}\overline{\rho}}(\overline{\rho}, \overline{z}, t) + \frac{1}{\overline{\rho}} v_{\overline{\rho}}(\overline{\rho}, \overline{z}, t) + \frac{a^2}{b^2} v_{\overline{z}\overline{z}}(\overline{\rho}, \overline{z}, t), \tag{3.8}$$

with the following initial and boundary conditions:

$$v(\overline{\rho}, \overline{z}, 0) = \overline{v}_0(\overline{\rho}, \overline{z}) \tag{3.9}$$

$$v(1, \overline{z}, t) = T_w \tag{3.10}$$

$$v_{\overline{\rho}}(0, \overline{z}, t) = 0 \tag{3.11}$$

$$v_{\overline{z}}(\overline{\rho}, 1, t) = 0 \tag{3.12}$$

$$v_{\overline{z}}(\overline{\rho}, 0, t) = \overline{f}(\overline{\rho})\ (U_0 + \delta U(t)), \tag{3.13}$$

where $\overline{v}_0(\overline{\rho}, \overline{z})$ and $\overline{f}(\overline{\rho})$ are initial heat distribution and the geometric distribution of the control action signal in the scaled spatial space, respectively. Next, we scale time to normalize the thermal diffusivity

$$\overline{t} = \frac{\kappa}{a^2} t$$

and introduce the following variable

$$\eta = \frac{a^2}{b^2}$$

So (3.8) to (3.13) become

$$v_t(\overline{\rho}, \overline{z}, \overline{t}) = v_{\overline{\rho}\overline{\rho}}(\overline{\rho}, \overline{z}, \overline{t}) + \frac{1}{\overline{\rho}} v_{\overline{\rho}}(\overline{\rho}, \overline{z}, \overline{t}) + \eta\, v_{\overline{z}\overline{z}}(\overline{\rho}, \overline{z}, \overline{t}) \tag{3.14}$$

with

$$v(\overline{\rho}, \overline{z}, 0) = \overline{v}_0(\overline{\rho}, \overline{z}) \tag{3.15}$$

$$v(1, \overline{z}, \overline{t}) = T_a \tag{3.16}$$

$$v_{\overline{\rho}}(0, \overline{z}, \overline{t}) = 0 \tag{3.17}$$

$$v_{\overline{z}}(\overline{\rho}, 1, \overline{t}) = 0 \tag{3.18}$$

$$v_{\overline{z}}(\overline{\rho}, 0, \overline{t}) = \overline{f}(\overline{\rho})(U_0 + \delta \overline{U}(\overline{t})), \tag{3.19}$$

where $1 \ll \eta$ because $b \ll a$. Introducing a new function,

$$u = v - \overline{v},$$

where $\overline{v}$ is the steady-state profile and is a solution to the boundary value PDE

$$\overline{v}_{\overline{\rho}\overline{\rho}}(\overline{\rho}, \overline{z}) + \frac{1}{\overline{\rho}} \overline{v}_{\overline{\rho}}(\overline{\rho}, \overline{z}) + \eta \, \overline{v}_{\overline{z}\overline{z}}(\overline{\rho}, \overline{z}) = 0, \tag{3.20}$$

with the following boundary conditions

$$\overline{v}(1, \overline{z}) = T_w \tag{3.21}$$

$$\overline{v}_{\overline{\rho}}(0, \overline{z}) = 0 \tag{3.22}$$

$$\overline{v}_{\overline{z}}(\overline{\rho}, 1) = 0 \tag{3.23}$$

$$\overline{v}_{\overline{z}}(\overline{\rho}, 0) = \overline{f}(\overline{\rho}) \; U_0. \tag{3.24}$$

Finally we obtain,

$$u_{\overline{t}}(\overline{\rho}, \overline{z}, \overline{t}) = u_{\overline{\rho}\overline{\rho}}(\overline{\rho}, \overline{z}, \overline{t}) + \frac{1}{\overline{\rho}} u_{\overline{\rho}}(\overline{\rho}, \overline{z}, \overline{t}) + \eta \, u_{\overline{z}\overline{z}}(\overline{\rho}, \overline{z}, \overline{t}) \tag{3.25}$$

with the following boundary condition

$$u(\overline{\rho}, \overline{z}, 0) = v_0(\overline{\rho}, \overline{z}) - \overline{v}_0(\overline{\rho}, \overline{z}) \doteq u_0(\overline{\rho}, \overline{z}) \tag{3.26}$$

$$u(1, \overline{z}, \overline{t}) = 0 \tag{3.27}$$

$$u_{\overline{\rho}}(0, \overline{z}, \overline{t}) = 0 \tag{3.28}$$

$$u_{\overline{z}}(\overline{\rho}, 1, \overline{t}) = 0 \tag{3.29}$$

$$u_{\overline{z}}(\overline{\rho}, 0, \overline{t}) = \overline{f}(\overline{\rho}) \; \delta\overline{U}(\overline{t}) \tag{3.30}$$

For the sake of readability, we use the same notation ρ, z and t that we used for the original space instead of the scaled spatial and temporal variables $\overline{\rho}$, $\overline{z}$ and $\overline{t}$. Obviously, the normalized system is expressed in the normalized spatial and temporal spaces and the backward calculations are necessary before continuing with any attempt to implement the results.

To summarize this section, the normalized PDE equation describing dynamic heat distribution in PCR microchip is given by:

$$u_t(\rho, z, t) = u_{\rho\rho}(\rho, z, t) + \frac{1}{\rho} u_{\rho}(\rho, z, t) + \eta \, u_{zz}(\rho, z, t) \tag{3.31}$$

where u is temperature, ρ and z are normalized spatial variables, $0 \leq \rho \leq 1$ and $0 \leq z \leq 1$. $\eta = \frac{a^2}{b^2}$ and $1 \ll \eta$. Initial condition and boundary conditions for the normalized model are as follows:

$$u(\rho, z, 0) = u_0(\rho, z) \tag{3.32}$$

$$u(1, z, t) = 0 \tag{3.33}$$

$$u_\rho(0, z, t) = 0 \tag{3.34}$$

$$u_z(\rho, 1, t) = 0 \tag{3.35}$$

$$u_z(\rho, 0, t) = f(\rho)\ \delta U(t) \qquad \text{(boundary actuation)} \tag{3.36}$$

where $\delta U(t)$ is the normalized input power and $f(\rho)$ describes the spatial distribution of the actuator at the bottom boundary as follows:

$$f(\rho) = \begin{cases} 1 & \text{if } \frac{k_1}{a} < \rho < \frac{(k_1+k_2)}{a} \\ 0.5 & \text{if } \rho = \frac{k_1}{a} \text{ or } \rho = \frac{(k_1+k_2)}{a} \\ 0 & \text{otherwise.} \end{cases} \tag{3.37}$$

To simplify our notation, we will drop the dependence on time, t, from our equations. Thus, we write, $u(\rho, z)$, instead of $u(\rho, z, t)$, etc.

3.2.2 Overview of Mathematical Background

The following formulas are repeatedly used in this chapter and throughout the chapter 4 [102].

Leibniz Integral Rule

$$\frac{d}{d\alpha}\int_{a(\alpha)}^{b(\alpha)} f(x,\alpha)dx = \frac{db(\alpha)}{d\alpha}f(b(\alpha),\alpha) - \frac{da(\alpha)}{d\alpha}f(a(\alpha),\alpha) + \int_{a(\alpha)}^{b(\alpha)} \frac{\partial}{\partial\alpha}f(x,\alpha)dx \tag{3.38}$$

Integration by Parts

$$\int_a^b f(x)g'(x)dx = \Big(f(x)g(x)\Big|_a^b - \int_a^b f'(x)g(x)dx \tag{3.39}$$

3.3 PDE Backstepping Boundary Observer Design

For the PDE system described by (3.31) to (3.36), the PDE backstepping boundary observer has the following form [69] :

$$\hat{u}_t(\rho,z) = \hat{u}_{\rho\rho}(\rho,z) + \frac{1}{\rho}\hat{u}_\rho(\rho,z) + \eta\,\hat{u}_{zz}(\rho,z) + \ell(\rho,z)\,(u(\rho,0) - \hat{u}(\rho,0)), \tag{3.40}$$

along with the following boundary conditions:

$$\hat{u}(1,z) = 0 \tag{3.41}$$

$$\hat{u}_\rho(0,z) = 0 \tag{3.42}$$

$$\hat{u}_z(\rho,1) = 0 \tag{3.43}$$

$$\hat{u}_z(\rho,0) = f(\rho)\,\delta U + \ell_a\,(u(\rho,0) - \hat{u}(\rho,0)), \tag{3.44}$$

where $\ell(\rho,z)$ and ℓ_a are the observer parameters. Introducing the observer error $\tilde{u}(\rho,z) = u(\rho,z) - \hat{u}(\rho,z)$, calculating the PDE equation of the observer error dynamics results in:

$$\tilde{u}_t(\rho,z) = \tilde{u}_{\rho\rho}(\rho,z) + \frac{1}{\rho}\tilde{u}_\rho(\rho,z) + \eta\,\tilde{u}_{zz}(\rho,z) - \ell(\rho,z)\,\tilde{u}(\rho,0), \tag{3.45}$$

with the following boundary conditions:

$$\tilde{u}(1,z) = 0 \tag{3.46}$$

$$\tilde{u}_\rho(0,z) = 0 \tag{3.47}$$

$$\tilde{u}_z(\rho,1) = 0 \tag{3.48}$$

$$\tilde{u}_z(\rho,0) = -\,\ell_a\tilde{u}(\rho,0). \tag{3.49}$$

The observer design problem consists of determining the observer parameters $\ell(\rho,z)$ and ℓ_a such that the estimation error asymptotically converges to zero at the all points in the domain. We look for an integral transformation of the form

$$\tilde{u}(\rho,z) = \tilde{w}(\rho,z) - \int_\rho^1 \int_0^z P(\rho,\xi_1,z,\xi_2)\,\tilde{w}(\xi_1,\xi_2)\,\xi_1\,d\xi_2 d\xi_1, \tag{3.50}$$

to transform the error dynamics into the following exponentially stable target system:

$$\tilde{w}_t(\rho,z) = \tilde{w}_{\rho\rho}(\rho,z) + \frac{1}{\rho}\tilde{w}_\rho(\rho,z) + \eta\,\tilde{w}_{zz}(\rho,z), \tag{3.51}$$

with the following boundary conditions:

$$\tilde{w}(1,z) = 0 \tag{3.52}$$

$$\tilde{w}_\rho(0,z) = 0 \tag{3.53}$$

$$\tilde{w}_z(\rho,1) = 0 \tag{3.54}$$

$$\tilde{w}_z(\rho,0) = 0. \tag{3.55}$$

We start differentiating the integral transformation (3.50) with respect to ρ as follows:

$$\begin{aligned}
\tilde{u}_\rho(\rho,z) =& \tilde{w}_\rho(\rho,z) - \frac{d}{d\rho}\int_\rho^1 \int_0^z P(\rho,\xi_1,z,\xi_2)\tilde{w}(\xi_1,\xi_2)\,\xi_1 d\xi_2 d\xi_1 \\
=& \tilde{w}_\rho(\rho,z) - \int_0^z \left(\frac{d}{d\rho}\int_\rho^1 P(\rho,\xi_1,z,\xi_2)\tilde{w}(\xi_1,\xi_2)\,\xi_1 d\xi_1\right) d\xi_2 \\
=& \tilde{w}_\rho(\rho,z) \\
& - \int_0^z \left(-P(\rho,\rho,z,\xi_2)\tilde{w}(\rho,\xi_2)\,\rho + \int_\rho^1 P_\rho(\rho,\xi_1,z,\xi_2)\tilde{w}(\xi_1,\xi_2)\,\xi_1 d\xi_1\right) d\xi_2
\end{aligned}$$

which results in

$$\begin{aligned}
\tilde{u}_\rho(\rho,z) =& \tilde{w}_\rho(\rho,z) + \int_0^z P(\rho,\rho,z,\xi_2)\tilde{w}(\rho,\xi_2)\,\rho d\xi_2 \\
& - \int_0^z \int_\rho^1 P_\rho(\rho,\xi_1,z,\xi_2)\tilde{w}(\xi_1,\xi_2)\,\xi_1 d\xi_1 d\xi_2.
\end{aligned} \tag{3.56}$$

Differentiating (3.56) with respect to ρ gives

$$\begin{aligned}
\tilde{u}_{\rho\rho}(\rho,z) =& \tilde{w}_{\rho\rho}(\rho,z) \\
& + \int_0^z \frac{d}{d\rho}\left(P(\rho,\rho,z,\xi_2)\tilde{w}(\rho,\xi_2)\,\rho\right) d\xi_2 \\
& - \int_0^z \frac{d}{d\rho}\left(\int_\rho^1 P_\rho(\rho,\xi_1,z,\xi_2)\tilde{w}(\xi_1,\xi_2)\,\xi_1 d\xi_1\right) d\xi_2
\end{aligned}$$

and

$$\begin{aligned}
\tilde{u}_{\rho\rho}(\rho,z) =& \tilde{w}_{\rho\rho}(\rho,z) + \int_0^z \tilde{w}(\rho,\xi_2)\,\rho\frac{d}{d\rho}P(\rho,\rho,z,\xi_2)\,d\xi_2 \\
& + \int_0^z P(\rho,\rho,z,\xi_2)\tilde{w}_\rho(\rho,\xi_2)\,\rho\,d\xi_2 + \int_0^z P(\rho,\rho,z,\xi_2)\tilde{w}(\rho,\xi_2)d\xi_2 \\
& - \int_0^z \left(-P_\rho(\rho,\rho,z,\xi_2)\tilde{w}(\rho,\xi_2)\rho + \int_\rho^1 P_{\rho\rho}(\rho,\xi_1,z,\xi_2)\tilde{w}(\xi_1,\xi_2)\,\xi_1\,d\xi_1\right) d\xi_2
\end{aligned}$$

which results in

$$\begin{aligned}\tilde{u}_{\rho\rho}(\rho,z) = \tilde{w}_{\rho\rho}(\rho,z) &+ 2\int_0^z P_\rho(\rho,\rho,z,\xi_2)\tilde{w}(\rho,\xi_2)\,\rho\,d\xi_2 \\ &+ \int_0^z P_{\xi_1}(\rho,\rho,z,\xi_2)\tilde{w}(\rho,\xi_2)\,\rho\,d\xi_2 \\ &+ \int_0^z P(\rho,\rho,z,\xi_2)\tilde{w}_\rho(\rho,\xi_2)\,\rho\,d\xi_2 \\ &+ \int_0^z P(\rho,\rho,z,\xi_2)\tilde{w}(\rho,\xi_2)d\xi_2 \\ &- \int_0^z \int_\rho^1 P_{\rho\rho}(\rho,\xi_1,z,\xi_2)\tilde{w}(\xi_1,\xi_2)\,\xi_1\,d\xi_1 d\xi_2.\end{aligned} \tag{3.57}$$

Now we differentiate the integral transformation (3.50) with respect to z as follows:

$$\begin{aligned}\tilde{u}_z(\rho,z) =& \tilde{w}_z(\rho,z) - \frac{d}{dz}\int_\rho^1\int_0^z P(\rho,\xi_1,z,\xi_2)\tilde{w}(\xi_1,\xi_2)\,\xi_1 d\xi_2 d\xi_1 \\ =& \tilde{w}_z(\rho,z) - \int_\rho^1 \left(\frac{d}{dz}\int_0^z P(\rho,\xi_1,z,\xi_2)\tilde{w}(\xi_1,\xi_2)\,d\xi_2\right)\xi_1 d\xi_1 \\ =& \tilde{w}_z(\rho,z) \\ &- \int_\rho^1 \left(P(\rho,\xi_1,z,z)\tilde{w}(\xi_1,z) + \int_0^z P_z(\rho,\xi_1,z,\xi_2)\tilde{w}(\xi_1,\xi_2)\,d\xi_2\right)\xi_1 d\xi_1\end{aligned}$$

which results in:

$$\begin{aligned}\tilde{u}_z(\rho,z) =& \tilde{w}_z(\rho,z) - \int_\rho^1 P(\rho,\xi_1,z,z)\tilde{w}(\xi_1,z)\,\xi_1\,d\xi_1 \\ &- \int_0^z\int_\rho^1 P_z(\rho,\xi_1,z,\xi_2)\tilde{w}(\xi_1,\xi_2)\,\xi_1 d\xi_1 d\xi_2.\end{aligned} \tag{3.58}$$

Differentiating again with respect to z we have

$$\begin{aligned}\tilde{u}_{zz}(\rho,z) = \tilde{w}_{zz}(\rho,z) &- \int_\rho^1 \frac{d}{dz}\left(P(\rho,\xi_1,z,z)\tilde{w}(\xi_1,z)\right)\,\xi_1\,d\xi_1 \\ &- \int_\rho^1 \left(\frac{d}{dz}\int_0^z P_z(\rho,\xi_1,z,\xi_2)\tilde{w}(\xi_1,\xi_2)\,d\xi_2\right)\,\xi_1 d\xi_1\end{aligned}$$

and

$$\begin{aligned}\tilde{u}_{zz}(\rho,z) = \tilde{w}_{zz}(\rho,z) &- \int_\rho^1 \frac{d}{dz}\left(P(\rho,\xi_1,z,z)\right)\,\tilde{w}(\xi_1,z)\,\xi_1\,d\xi_1 \\ &- \int_\rho^1 P(\rho,\xi_1,z,z)\tilde{w}_z(\xi_1,z)\,\xi_1\,d\xi_1 \\ &- \int_\rho^1 \left(P_z(\rho,\xi_1,z,z)\tilde{w}(\xi_1,z) + \int_0^z P_{zz}(\rho,\xi_1,z,\xi_2)\tilde{w}(\xi_1,\xi_2)\,d\xi_2\right)\,\xi_1 d\xi_1\end{aligned}$$

which results in

$$\begin{aligned}\tilde{u}_{zz}(\rho,z) = \tilde{w}_{zz}(\rho,z) &- 2\int_{\rho}^{1} P_z(\rho,\xi_1,z,z)\tilde{w}(\xi_1,z)\,\xi_1\,d\xi_1 \\ &- \int_{\rho}^{1} P_{\xi_2}(\rho,\xi_1,z,z)\tilde{w}(\xi_1,z)\,\xi_1\,d\xi_1 \\ &- \int_{\rho}^{1} P(\rho,\xi_1,z,z)\tilde{w}_z(\xi_1,z)\,\xi_1\,d\xi_1 \\ &- \int_{\rho}^{1}\int_{0}^{z} P_{zz}(\rho,\xi_1,z,\xi_2)\tilde{w}(\xi_1,\xi_2)\,\xi_1\,d\xi_2 d\xi_1.\end{aligned} \tag{3.59}$$

Next we differentiate the integral transformation (3.50) with respect to temporal variable t as follows:

$$\tilde{u}_t(\rho,z) = \tilde{w}_t(\rho,z) - \int_{\rho}^{1}\int_{0}^{z} P(\rho,\xi_1,z,\xi_2)\tilde{w}_t(\xi_1,\xi_2)\,\xi_1\,d\xi_2 d\xi_1, \tag{3.60}$$

Using (3.51) in (3.60), we get:

$$\begin{aligned}\tilde{u}_t(\rho,z) = \tilde{w}_t(\rho,z) &\\ - \int_{\rho}^{1}\int_{0}^{z} P(\rho,\xi_1,z,\xi_2)\tilde{w}_{\xi_1\xi_1}(\xi_1,\xi_2)\,\xi_1\,d\xi_2 d\xi_1 &\qquad (3.61)\\ - \int_{\rho}^{1}\int_{0}^{z} P(\rho,\xi_1,z,\xi_2)\tilde{w}_{\xi_1}(\xi_1,\xi_2)\,d\xi_2 d\xi_1 &\qquad (3.62)\\ - \eta\int_{\rho}^{1}\int_{0}^{z} P(\rho,\xi_1,z,\xi_2)\tilde{w}_{\xi_1\xi_1}(\xi_1,\xi_2)\,\xi_1\,d\xi_2 d\xi_1. &\qquad (3.63)\end{aligned}$$

We separately calculate (3.61), (3.62) and (3.63). To calculate (3.61), we integration by part,

$$\begin{aligned}&\int_{\rho}^{1}\int_{0}^{z} P(\rho,\xi_1,z,\xi_2)\tilde{w}_{\xi_1\xi_1}(\xi_1,\xi_2)\,\xi_1\,d\xi_2 d\xi_1 = \\ &\qquad \int_{0}^{z}\left(\int_{\rho}^{1} P(\rho,\xi_1,z,\xi_2)\tilde{w}_{\xi_1\xi_1}(\xi_1,\xi_2)\,\xi_1\,d\xi_1\right)d\xi_2 \\ &= \int_{0}^{z}\Big(\big(P(\rho,\xi_1,z,\xi_2)\xi_1\tilde{w}_{\xi_1}(\xi_1,\xi_2)\,\Big|_{\rho}^{1} \\ &\quad - \int_{\rho}^{1}\frac{d}{d\xi_1}\big(P(\rho,\xi_1,z,\xi_2)\xi_1\,\big)\tilde{w}_{\xi_1}(\xi_1,\xi_2)\,d\xi_1\Big)d\xi_2 \\ &= \int_{0}^{z}\Big(P(\rho,1,z,\xi_2)\tilde{w}_{\xi_1}(1,\xi_2) - P(\rho,\rho,z,\xi_2)\rho\tilde{w}_{\xi_1}(\rho,\xi_2) \\ &\quad - \int_{\rho}^{1} P_{\xi_1}(\rho,\xi_1,z,\xi_2)\tilde{w}_{\xi_1}(\xi_1,\xi_2)\,\xi_1\,d\xi_1 - \int_{\rho}^{1} P(\rho,\xi_1,z,\xi_2)\tilde{w}_{\xi_1}(\xi_1,\xi_2)\,d\xi_1\Big)d\xi_2\end{aligned} \tag{3.64}$$

Again by using integration by parts we have,

$$\begin{aligned}
&\int_\rho^1 P_{\xi_1}(\rho,\xi_1,z,\xi_2)\tilde{w}_{\xi_1}(\xi_1,\xi_2)\,\xi_1\,d\xi_1 \\
&\quad= \Big(P_{\xi_1}(\rho,\xi_1,z,\xi_2)\xi_1\tilde{w}(\xi_1,\xi_2)\,\Big|_\rho^1 - \int_\rho^1 \frac{d}{d\xi_1}\Big(P_{\xi_1}(\rho,\xi_1,z,\xi_2)\xi_1\Big)\tilde{w}(\xi_1,\xi_2)\,d\xi_1 \\
&\quad= P_{\xi_1}(\rho,1,z,\xi_2)\tilde{w}(1,\xi_2) - P_{\xi_1}(\rho,\rho,z,\xi_2)\,\rho\,\tilde{w}(\rho,\xi_2) \\
&\quad- \int_\rho^1 P_{\xi_1\xi_1}(\rho,\xi_1,z,\xi_2)\xi_1\,\tilde{w}(\xi_1,\xi_2)\,d\xi_1 - \int_\rho^1 P_{\xi_1}(\rho,\xi_1,z,\xi_2)\tilde{w}(\xi_1,\xi_2)\,d\xi_1
\end{aligned} \tag{3.65}$$

and

$$\begin{aligned}
&\int_\rho^1 P(\rho,\xi_1,z,\xi_2)\tilde{w}_{\xi_1}(\xi_1,\xi_2)\,d\xi_1 \\
&\qquad=\Big(P(\rho,\xi_1,z,\xi_2)\tilde{w}(\xi_1,\xi_2)\,\Big|_\rho^1 \\
&\qquad\quad- \int_\rho^1 \frac{d}{d\xi_1}\Big(P_{\xi_1}(\rho,\xi_1,z,\xi_2)\Big)\,\tilde{w}(\xi_1,\xi_2)\,d\xi_1 \\
&\qquad=P(\rho,1,z,\xi_2)\tilde{w}(1,\xi_2) - P(\rho,\rho,z,\xi_2)\,\tilde{w}(\rho,\xi_2) \\
&\qquad\quad- \int_\rho^1 P_{\xi_1}(\rho,\xi_1,z,\xi_2)\tilde{w}(\xi_1,\xi_2)\,d\xi_1
\end{aligned} \tag{3.66}$$

Now by using (3.65) and (3.66) in (3.64) we have

$$\begin{aligned}
&\int_\rho^1\int_0^z P(\rho,\xi_1,z,\xi_2)\tilde{w}_{\xi_1\xi_1}(\xi_1,\xi_2)\,\xi_1\,d\xi_2 d\xi_1 \\
&\quad= \int_0^z \Big(P(\rho,1,z,\xi_2)\tilde{w}_{\xi_1}(1,\xi_2) - P(\rho,\rho,z,\xi_2)\rho\tilde{w}_{\xi_1}(\rho,\xi_2)\Big)d\xi_2 \\
&\quad- \int_0^z \Big(P_{\xi_1}(\rho,1,z,\xi_2)\tilde{w}(1,\xi_2) - P_{\xi_1}(\rho,\rho,z,\xi_2)\,\rho\,\tilde{w}(\rho,\xi_2) \\
&\quad- \int_\rho^1 P_{\xi_1\xi_1}(\rho,\xi_1,z,\xi_2)\xi_1\,\tilde{w}(\xi_1,\xi_2)\,d\xi_1 - \int_\rho^1 P_{\xi_1}(\rho,\xi_1,z,\xi_2)\tilde{w}(\xi_1,\xi_2)\,d\xi_1\Big)d\xi_2 \\
&\quad- \int_0^z \Big(P(\rho,1,z,\xi_2)\tilde{w}(1,\xi_2) - P(\rho,\rho,z,\xi_2)\,\tilde{w}(\rho,\xi_2) \\
&\quad- \int_\rho^1 P_{\xi_1}(\rho,\xi_1,z,\xi_2)\tilde{w}(\xi_1,\xi_2)\,d\xi_1\Big)d\xi_2
\end{aligned} \tag{3.67}$$

And finally we arrive to:

$$\begin{aligned}
&\int_\rho^1 \int_0^z P(\rho,\xi_1,z,\xi_2)\tilde{w}_{\xi_1\xi_1}(\xi_1,\xi_2)\,\xi_1\,d\xi_2 d\xi_1 \\
&\qquad = \int_0^z P(\rho,1,z,\xi_2)\Big(\tilde{w}_{\xi_1}(1,\xi_2)-\tilde{w}(1,\xi_2)\Big)d\xi_2 \\
&\qquad + \int_0^z P(\rho,\rho,z,\xi_2)\Big(-\tilde{w}_{\xi_1}(\rho,\xi_2)\rho+\tilde{w}(\rho,\xi_2)\Big)d\xi_2 \\
&\qquad - \int_0^z P_{\xi_1}(\rho,1,z,\xi_2)\tilde{w}(1,\xi_2)d\xi_2 + \int_0^z P_{\xi_1}(\rho,\rho,z,\xi_2)\tilde{w}(\rho,\xi_2)\,\rho\,d\xi_2 \\
&\qquad + \int_0^z \int_\rho^1 \Big(P_{\xi_1\xi_1}(\rho,\xi_1,z,\xi_2)\xi_1 + 2P_{\xi_1}(\rho,\xi_1,z,\xi_2)\Big)\tilde{w}(\xi_1,\xi_2)d\xi_1 d\xi_2
\end{aligned} \tag{3.68}$$

To calculate the second part, (3.62), we integration by part,

$$\begin{aligned}
\int_\rho^1 \int_0^z P(\rho,\xi_1,z,\xi_2)\tilde{w}_{\xi_1}(\xi_1,\xi_2)\,d\xi_2 d\xi_1 &= \int_0^z \left(\int_\rho^1 P(\rho,\xi_1,z,\xi_2)\tilde{w}_{\xi_1}(\xi_1,\xi_2)\,d\xi_1\right) d\xi_2 \\
&= \int_0^z \left(\Big(P(\rho,\xi_1,z,\xi_2)\tilde{w}(\xi_1,\xi_2)\,\Big|_\rho^1 - \int_\rho^1 \frac{d}{d\xi_1}\Big(P(\rho,\xi_1,z,\xi_2)\Big)\tilde{w}(\xi_1,\xi_2)\,d\xi_1\right) d\xi_2 \\
&= \int_0^z P(\rho,1,z,\xi_2)\tilde{w}(1,\xi_2)d\xi_2 \\
&- \int_0^z P(\rho,\rho,z,\xi_2)\tilde{w}(\rho,\xi_2)d\xi_2 \\
&- \int_0^z \int_\rho^1 P_{\xi_1}(\rho,\xi_1,z,\xi_2)\tilde{w}(\xi_1,\xi_2)\,d\xi_1 d\xi_2
\end{aligned} \tag{3.69}$$

To calculate the third part, (3.63), we write,

$$\begin{aligned}
&\eta \int_\rho^1 \int_0^z P(\rho,\xi_1,z,\xi_2)\tilde{w}_{\xi_2\xi_2}(\xi_1,\xi_2)\,\xi_1\,d\xi_2 d\xi_1 \\
&\qquad = \eta \int_\rho^1 \left(\int_0^z P(\rho,\xi_1,z,\xi_2)\tilde{w}_{\xi_2\xi_2}(\xi_1,\xi_2)\,d\xi_2\right)\xi_1\,d\xi_1
\end{aligned} \tag{3.70}$$

But we have

$$\begin{aligned}
&\int_0^z P(\rho,\xi_1,z,\xi_2)\tilde{w}_{\xi_2\xi_2}(\xi_1,\xi_2)\,d\xi_2 \\
&\quad= \Big(P(\rho,\xi_1,z,\xi_2)\tilde{w}_{\xi_2}(\xi_1,\xi_2)\,\Big|_0^z - \int_0^z P_{\xi_2}(\rho,\xi_1,z,\xi_2)\tilde{w}_{\xi_2}(\xi_1,\xi_2)\,d\xi_2 \\
&\quad= \Big(P(\rho,\xi_1,z,\xi_2)\tilde{w}_{\xi_2}(\xi_1,\xi_2)\,\Big|_0^z - \Big(P_{\xi_2}(\rho,\xi_1,z,\xi_2)\tilde{w}(\xi_1,\xi_2)\,\Big|_0^z \\
&\quad+ \int_0^z P_{\xi_2\xi_2}(\rho,\xi_1,z,\xi_2)\tilde{w}(\xi_1,\xi_2)\,d\xi_2 \\
&\quad= P(\rho,\xi_1,z,z)\tilde{w}_{\xi_2}(\xi_1,z) - P(\rho,\xi_1,z,0)\tilde{w}_{\xi_2}(\xi_1,0) \\
&\quad- P_{\xi_2}(\rho,\xi_1,z,z)\tilde{w}(\xi_1,z) + P_{\xi_2}(\rho,\xi_1,z,0)\tilde{w}(\xi_1,0) \\
&\quad+ \int_0^z P_{\xi_2\xi_2}(\rho,\xi_1,z,\xi_2)\tilde{w}(\xi_1,\xi_2)\,d\xi_2
\end{aligned} \tag{3.71}$$

So by using (3.71) in (3.70) we finally arrive to

$$\begin{aligned}
\eta\int_\rho^1\int_0^z P(\rho,\xi_1,z,\xi_2)\tilde{w}_{\xi_2\xi_2}(\xi_1,\xi_2)\,\xi_1\,d\xi_2 d\xi_1 \\
&= \eta\int_\rho^1 P(\rho,\xi_1,z,z)\tilde{w}_{\xi_2}(\xi_1,z)\xi_1\,d\xi_1 \\
&- \eta\int_\rho^1 P(\rho,\xi_1,z,0)\tilde{w}_{\xi_2}(\xi_1,0)\xi_1\,d\xi_1 \\
&- \eta\int_\rho^1 P_{\xi_2}(\rho,\xi_1,z,z)\tilde{w}(\xi_1,z)\xi_1\,d\xi_1 \\
&+ \eta\int_\rho^1 P_{\xi_2}(\rho,\xi_1,z,0)\tilde{w}(\xi_1,0)\xi_1\,d\xi_1 \\
&+ \eta\int_\rho^1\int_0^z P_{\xi_2\xi_2}(\rho,\xi_1,z,\xi_2)\tilde{w}(\xi_1,\xi_2)\,\xi_1\,d\xi_2\,d\xi_1
\end{aligned} \tag{3.72}$$

Now, using (3.68), (3.69) and (3.72), (3.60) can be simplified and written as

follows:

$$
\begin{aligned}
\tilde{u}_t(\rho,z) &= \tilde{w}_t(\rho,z) \\
&\quad - \int_0^z P(\rho,1,z,\xi_2)\tilde{w}_{\xi_1}(1,\xi_2)d\xi_2 \\
&\quad + \int_0^z P(\rho,\rho,z,\xi_2)\tilde{w}_{\xi_1}(\rho,\xi_2)\rho d\xi_2 \\
&\quad + \int_0^z P_{\xi_1}(\rho,1,z,\xi_2)\tilde{w}(1,\xi_2)d\xi_2 \\
&\quad - \int_0^z P_{\xi_1}(\rho,\rho,z,\xi_2)\tilde{w}(\rho,\xi_2)\,\rho\,d\xi_2 \\
&\quad - \int_0^z \int_\rho^1 \Big(P_{\xi_1\xi_1} + \frac{1}{\xi_1}P_{\xi_1} + \eta P_{\xi_2\xi_2}\Big)\tilde{w}(\xi_1,\xi_2)\xi_1 d\xi_1 d\xi_2 \\
&\quad - \eta \int_\rho^1 P(\rho,\xi_1,z,z)\tilde{w}_{\xi_2}(\xi_1,z)\xi_1\,d\xi_1 \\
&\quad + \eta \int_\rho^1 P(\rho,\xi_1,z,0)\tilde{w}_{\xi_2}(\xi_1,0)\xi_1\,d\xi_1 \\
&\quad + \eta \int_\rho^1 P_{\xi_2}(\rho,\xi_1,z,z)\tilde{w}(\xi_1,z)\xi_1\,d\xi_1 \\
&\quad - \eta \int_\rho^1 P_{\xi_2}(\rho,\xi_1,z,0)\tilde{w}(\xi_1,0)\xi_1\,d\xi_1.
\end{aligned}
\tag{3.73}
$$

From (3.50) we have

$$
\tilde{u}(\rho,0) = \tilde{w}(\rho,0). \tag{3.74}
$$

Subtracting (3.51) from (3.45) and using (3.52), (3.53), (3.54), (3.55) and (3.74) we obtain,

$$
\begin{aligned}
&\int_0^z \int_\rho^1 \big(P_{\xi_1\xi_1} + \frac{1}{\xi_1}P_{\xi_1} + \eta P_{\xi_2\xi_2}\big)\tilde{w}(\xi_1,\xi_2)\,\xi_1\,d\xi_1 d\xi_2 \\
&\quad - \int_0^z \int_\rho^1 \big(P_{\rho\rho} + \frac{1}{\rho}P_\rho + \eta P_{zz}\big)\tilde{w}(\xi_1,\xi_2)\,\xi_1\,d\xi_1 d\xi_2 \\
&\quad + \int_0^z P(\rho,1,z,\xi_2)\tilde{w}_{\xi_1}(1,\xi_2)d\xi_2 \\
&\quad + \eta \int_\rho^1 P_{\xi_2}(\rho,\xi_1,z,0)\tilde{w}(\xi_1,0)\xi_1\,d\xi_1 \\
&\quad + 2\int_0^z \Big(\rho\frac{d}{d\rho}P(\rho,\rho,z,\xi_2) + P(\rho,\rho,z,\xi_2)\Big)\tilde{w}(\rho,\xi_2)\,d\xi_2 \\
&\quad - 2\eta \int_\rho^1 \frac{d}{dz}P(\rho,\xi_1,z,z)\tilde{w}(\xi_1,z)\,\xi_1\,d\xi_1 \\
&\quad = \ell(\rho)\tilde{w}(\rho,0).
\end{aligned}
\tag{3.75}
$$

Boundary conditions provide two additional conditions. From (3.49) we have

$$\tilde{u}_z(\rho,0) = -\ell_a\,\tilde{u}(\rho,0). \tag{3.76}$$

Setting $z=0$ in (3.58) and using (3.76) we arrive to,

$$\ell_a\,\tilde{w}(\rho,0) = \int_\rho^1 P(\rho,\xi_1,0,0)\tilde{w}(\xi_1,0)\,\xi_1\,d\xi_1. \tag{3.77}$$

Applying transformation (3.50) to boundary condition (3.47) and using (3.53) , we get

$$\tilde{u}_\rho(0,z) = -\int_0^z\int_0^1 P_\rho(0,\xi_1,z,\xi_2)\tilde{w}(\xi_1,\xi_2)\,\xi_1 d\xi_1 d\xi_2 = 0. \tag{3.78}$$

Equation (3.78) provides a new boundary condition for kernel function $P(\rho,\xi_1,z,\xi_2)$,

$$P_\rho(0,\xi_1,z,\xi_2) = 0. \tag{3.79}$$

Applying transformation (3.50) to the boundary condition (3.48) and using (3.54), we get

$$\begin{aligned}\tilde{u}_z(\rho,1) = &-\int_\rho^1 \Big(P(\rho,\xi_1,1,1)\tilde{w}(\xi_1,1)\\ &+\int_0^1 P_z(\rho,\xi_1,1,\xi_2)\tilde{w}(\xi_1,\xi_2)d\xi_2\Big)\,\xi_1 d\xi_1\\ &=0,\end{aligned} \tag{3.80}$$

so we have

$$P(\rho,\xi_1,1,1)\tilde{w}(\xi_1,1) + \int_0^1 P_z(\rho,\xi_1,1,\xi_2)\tilde{w}(\xi_1,\xi_2)d\xi_2 = 0. \tag{3.81}$$

Which provides the following new conditions for kernel function $P(\rho,\xi_1,z,\xi_2)$,:

$$P(\rho,\xi_1,1,1) = 0 \tag{3.82}$$

$$P_z(\rho,\xi_1,1,\xi_2) = 0. \tag{3.83}$$

To eliminate w from the equations, we proceed as follows: using (3.77) in (3.75) we

have,

$$\begin{aligned}
&\int_0^z \int_\rho^1 \big(P_{\xi_1\xi_1} + \frac{1}{\xi_1} P_{\xi_1} + \eta P_{\xi_2\xi_2}\big)\tilde{w}(\xi_1,\xi_2)\,\xi_1\,d\xi_1 d\xi_2 \\
&\quad - \int_0^z \int_\rho^1 \big(P_{\rho\rho} + \frac{1}{\rho} P_\rho + \eta P_{zz}\big)\tilde{w}(\xi_1,\xi_2)\,\xi_1\,d\xi_1 d\xi_2 \\
&\quad + \int_0^z P(\rho,1,z,\xi_2)\tilde{w}_{\xi_1}(1,\xi_2) d\xi_2 \\
&\quad + \eta \int_\rho^1 P_{\xi_2}(\rho,\xi_1,z,0)\tilde{w}(\xi_1,0)\xi_1\,d\xi_1 \\
&\quad + 2\int_0^z \Big(\rho \frac{d}{d\rho} P(\rho,\rho,z,\xi_2) + P(\rho,\rho,z,\xi_2)\Big)\tilde{w}(\rho,\xi_2)\,d\xi_2 \\
&\quad - 2\eta \int_\rho^1 \frac{d}{dz} P(\rho,\xi_1,z,z)\tilde{w}(\xi_1,z)\,\xi_1\,d\xi_1 \\
&\quad + \int_\rho^1 \Big(\eta P_{\xi_2}(\rho,\xi_1,z,0) - \frac{\ell(\rho)}{\ell_a} P(\rho,\xi_1,0,0)\Big)\tilde{w}(\xi_1,0)\,\xi_1\,d\xi_1 \\
&\quad = 0.
\end{aligned} \tag{3.84}$$

Setting every part of (3.84) equal to zero and adding the results to (3.79), (3.82), and (3.83), we arrive to PDE equation describing the kernel function, $P(\rho,\xi_1,z,\xi_2)$.

Observer parameters $\ell(\rho)$ and ℓ_a can be found by setting the last part of (3.84) equal to zero as follows:

$$\frac{\ell(\rho)}{\ell_a} = \frac{\eta\, P_{\xi_2}(\rho,\xi_1,z,0)}{P(\rho,\xi_1,0,0)}. \tag{3.85}$$

We summarize the results in a theorem stating that the observer parameters $\ell(\rho,z)$ and ℓ_a can be defined by the integral kernel $P(\rho,\xi_1,z,\xi_2)$.

Theorem 1. *Consider that the PDE observer error dynamics in 2-D cylindrical coordinates can be defined by* (3.45) *along with the integral transformation* (3.50) *that transforms the error dynamics into* (3.51)*, where $P(\rho,\xi_1,z,\xi_2)$ is the kernel of the integral transformation with $0 \le \rho \le \xi_1 \le 1$ and $0 \le \xi_2 \le z \le 1$. Under these conditions the observer parameters $\ell(\rho,z)$ and ℓ_a can be explicitly obtained from the kernel function, $P(\rho,\xi_1,z,\xi_2)$, and the kernel function itself can be calculated by solving the following PDE equation:*

$$P_{\rho\rho} + \frac{1}{\rho} P_\rho + \eta P_{zz} = P_{\xi_1\xi_1} + \frac{1}{\xi_1} P_{\xi_1} + \eta P_{\xi_2\xi_2}, \tag{3.86}$$

with following boundary conditions:

$$\rho\frac{d}{d\rho}P(\rho,\rho,z,\xi_2)+P(\rho,\rho,z,\xi_2)=0 \tag{3.87}$$

$$\frac{d}{dz}P(\rho,\xi_1,z,z)=0 \tag{3.88}$$

$$P_\rho(0,\xi_1,z,\xi_2)=0 \tag{3.89}$$

$$P_z(\rho,\xi_1,1,\xi_2)=0 \tag{3.90}$$

$$P(\rho,1,z,\xi_2)=0 \tag{3.91}$$

$$P(\rho,\xi_1,1,1)=0. \tag{3.92}$$

Remarks A simple inspection of the PDE (3.86)–(3.92) shows it has four independent variables. Solving this 4-D PDE is, in general, very difficult either analytically or numerically. In the next section, we use a conformal transformation to simplify (3.86) to a 2-D PDE of much simpler solution.

3.4 Transforming the Model Structure

3.4.1 Motivation

We begin by investigating the heat distribution in our problem: Fig. 3.3 shows the heat flux lines and constant temperature lines in our microchip. Heat flux lines and constant temperature lines are the solutions of the orthogonal functions in an infinite series describing the heat distribution in the microchip. Therefore, heat flux lines and constant temperature lines always intersect at 90°angles.

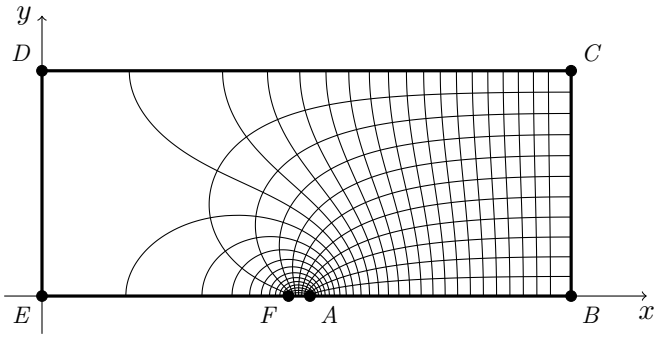

Figure 3.3: Initial geometry

The central idea to our approach consists of finding a transformation that maps the present domain structure into a new one in which the flux lines and the constant

temperature lines are straight lines intersecting at 90°angles. According to the standard results in the theory of complex variables, such transformation is known as *conformal transformation* or *conformal mapping*, [18]. Indeed, conformal mappings are characterized by the angle preserving property, meaning that any two curves before and after the transformation intersect at the same angle. A key element in the process of using the conformal mapping in a heat distribution problem is the fact that the Laplace equation describing the heat distribution is invariant under a conformal mapping, [18].

Since this section heavily relies on results from complex analysis, we introduce the notation used throughout. $\mathbb{C}$ denotes the field of complex numbers. For any $z \in \mathbb{C}$, $\mathbf{Re}(z)$ and $\mathbf{Im}(z)$ denote the real and imaginary parts of z, respectively. The modulus of z is denoted as $|z| = [\mathbf{Re}^2(z) + \mathbf{Im}^2(z)]^{\frac{1}{2}}$. Unless otherwise stated, all the constants have complex values and every function is a real function of a complex-variable. $\{\Omega_z; z_1, z_2, z_3, z_4\}$ denotes a generalized quadrilateral in complex plane where Ω_z is a Jordan region (i.e., bounded by the image of the unit circle under a continuous, one-to-one function) and four points z_1,z_2,z_3 and z_4 are lying in order on the boundary.

Throughout the rest of this section we will make use of standard results in the theory of complex analysis. For completeness, the main definitions and related theorems on conformal mapping are provided in the next section.

3.4.2 Background Material: Conformal Mapping

In this section, we briefly summarize the main relevant definitions and theorems in complex analysis. Let $\mathbb{C}$ represent the field of complex numbers. A set $\Omega \in \mathbb{C}$ is said to be a domain if it is open and connected. A function $f : \mathbb{C} \to \mathbb{C}$ is said to be analytic in a domain Ω if it differentiable at each point in the domain.

Definition 1. *Let Ω and Ω_1 be two domains in $\mathbb{C}$ and let $f : \Omega \to \Omega_1$. Let $\gamma_1(t)$ and $\gamma_2(t)$ in Ω be two differentiable curves defined on the time interval $(-\epsilon, \epsilon)$ and assume that $\gamma_1(t)$ and $\gamma_2(t)$ intersect at $t = 0$. The mapping f is said to preserve angles if the angle formed by the tangents to $\gamma_1(0)$ and $\gamma_2(0)$ is equal to the angle formed by the tangents to $f \circ \gamma_1$ and $f \circ \gamma_2$ at $t = 0$. A Conformal map from Ω to Ω_1 is a one-to-one, onto, differentiable function that preserves angles.*

Theorem 2. *A function $f : \mathbb{C} \to \mathbb{C}$ is conformal in a domain $\Omega \subset \mathbb{C}$ if and only if it is analytic in Ω and $f'(z) \neq 0$ in Ω.*

A central result in the conformal mapping is *Riemann Mapping Theorem* which can be stated as follows:

Theorem 3. *(Riemann Mapping Theorem) Any simply-connected domain $\Omega \subset \mathbb{C}$, whose boundary consists of more than one point, can be mapped conformally onto the unit disc $\mathbb{D}_1 := \{z \in \mathbb{C} : |z| < 1\}$. Moreover, the mapping f is unique provided that $f(z_0) = 0$ and $f'(z_0) > 0$ for $z_0 \in \Omega$ [71].*

In practise, however, the unit disc is not always the target domain. We might be interested in other forms of the target domain. This can be achieved using the chain property:

Corollaries 1. *(Chain Property) Any two simply-connected domains Ω_1 and Ω_2 can be mapped conformally onto each other. The mapping $\Omega_1 \to \Omega_2$ is unique up to the choice of three real parameters.*

The Riemann mapping theorem considers the interior point of the domain but does not provide any information about the boundary points. The question is answered in the next theorem:

Theorem 4. *(Carathéodory-Osgood) Let Ω be a Jordan domain, i.e. a domain bounded by a closed curve, or Jordan curve, and let f be a conformal mapping $f : \Omega \to \mathbb{D}_1$. Then, f can be extended one-to-one continuously to the closure $\bar{\Omega}_1 := \Omega \cup \partial\Omega$ of the domain Ω. Moreover, any three point on $\partial\Omega$ can be mapped on any three preassigned points (of the same orientation) on the unit circle $\partial\mathbb{D}_1$.*

To probe how the Laplace equation is invariance under the conformal mapping, we first recall the definition of harmonic functions:

Definition 2. *A twice continuously differentiable real-valued function $u(x, y) \in C^2(\Omega)$ of two real variables x and y is said to be harmonic in a domain Ω of the xy-plane if it satisfies Laplace equation, i.e. $\nabla^2 u = 0$ [18] throughout Ω.*

Theorem 5. *Suppose that $f(z) = u(x, y) + iy(x, y)$ is an analytic function in a domain Ω. It follows that $u(x, y)$ and $v(x, y)$ are harmonic functions.*

The function $u(\rho, z)$ in (3.103) that describes the heat distribution in a given domain is a harmonic function of the real variables ρ and z. We use these variables to construct a complex function which is analytic.

Central to the theorem 5 is the following theorem which states the invariance of the Laplace equation under conformal mapping.

Theorem 6. *Suppose that an analytic function $w = f(z) = u(x, y) + iy(x, y)$ maps a Domain Ω_z in the z-plane onto a domain Ω_w in the w-plane. If $h(u, v)$ is a harmonic function defined on Ω_w, then the function $H(x, y) = h(u(x, y), v(x, y))$ is a harmonic function in Ω_z.*

The important point about theorem 6 is the fact that the boundary conditions for both of the harmonic functions are of the Dirichlet type. In other words, we have $h = h_0$ on the boundary. In contrast, practical problems can impose boundaries of Neumann type or even of the mixed type. The following theorem provides the necessary result in that case.

Theorem 7. *Suppose that a transformation $w = f(z) = u(x, y) + iy(x, y)$ is conformal on a smooth arc γ, and let Γ be the image of γ under that transformation. If , along Γ, a function $h(u, v)$ satisfies either of the conditions $h = h_0$ or $\frac{dh}{dn} = 0$ where h_0 is a real constant and $\frac{dh}{dn}$ denotes derivatives normal to Γ, then, along γ, the function $H(x, y) = h(u(x, y), v(x, y))$ satisfies the corresponding conditions $H = h_0$ or $\frac{dH}{dN} = 0$ where $\frac{dH}{dN}$ denotes derivatives normal to γ.*

An important aspect of theorem 7 is the fact that it only considers Neumann condition equal to zero. For non-zero Neumann conditions ($\frac{dh}{dn} = cte \neq 0$) we can write $\frac{dh}{dn} = (gradh).n$ and $\frac{dH}{dN} = (gradH).N$ which result it the following equation [18],

$$\|grad\, H(x, y)\| = \|grad\, h(u, v)\| \cdot \|f'(z)\|. \tag{3.93}$$

Next, we introduce a transformation known as Schwarz-Christoffel transformation which helps solve an important class of the boundary value problems that involves regions with polygonal boundaries. The Schwarz-Christoffel transformation provides the formula to map the upper half-plane $\mathbf{Re}\{z\} > 0$ (or the unit disc $|z| < 1$) in the z-plane onto the interior of a given polygon in the w-plane.

Definition 3. *(Schwarz-Christoffel Transformation) Consider a polygon in the w plane having vertices at* $w_1, w_2, \cdots, w_n$ *with corresponding interior angles* $\alpha_1, \alpha_2, \cdots, \alpha_n$, *respectively. Let points* $w_1, w_2, \cdots, w_n$ *be the images of the points* $x_1, x_2, \cdots, x_n$ *on the real axis of the z-plane. A transformation that maps the upper half region of the z-plane onto the interior of the polygon of the w-plane and the real axis onto the boundary of the polygon is given by:*

$$\frac{dw}{dz} = C \prod_{i=1}^{n} (z - x_i)^{\frac{\alpha_i}{\pi} - 1}, \tag{3.94}$$

or in its integral form

$$w = f(z) = C_0 + C \int_{z_0}^{z} \prod_{i=1}^{n} (\zeta - x_i)^{\frac{\alpha_i}{\pi} - 1} d\zeta, \tag{3.95}$$

where C *and* $f(z_0)$ *are complex constant.*

The inverse Schwarz-Christoffel transformation is given by

$$z = f^{[-1]}(w) = z_0 + C' \int_{w_0}^{w} \prod_{i=1}^{n} (\zeta - w_i)^{\frac{\mu_i}{\pi} - 1} d\zeta, \tag{3.96}$$

where $\mu_i = \pi - \alpha_i$. The main practical difficulty with (3.95) is that except in special cases, the prevertices x_i cannot be computed analytically. Three of the prevertices, including the already fixed z_n, may be be chosen arbitrarily. The remaining $n - 3$ prevertices are then determined uniquely and can be obtained by solving a system of nonlinear equations. This is known as the **Schwarz-Christoffel parameter problem**, and in particular, its solution is the first step in calculation of any Schwarz-Christoffel mapping function. Once the parameter problem is solved, the multiplicative constant C can be found, and the mapping function f and its inverse can be computed numerically.

3.4.3 Mapping the System Domain

We are interested in a transformation to map the six vertex $[A, B, C, D, E, F]$ polygon shown in Fig. 3.3 onto a new coordinate system. The *Riemann mapping theorem* ensures that a mapping function exists taking the initial domain shown in Fig. 3.3 to the simpler domain shown in Fig. 3.5, [2].

The six segments that define this polygon, namely $[AB]$, $[BC]$, $[CD]$, $[DE]$, $[EF]$, and $[FA]$ intersect at points B, C, D, and E, with 90° angles and at points F

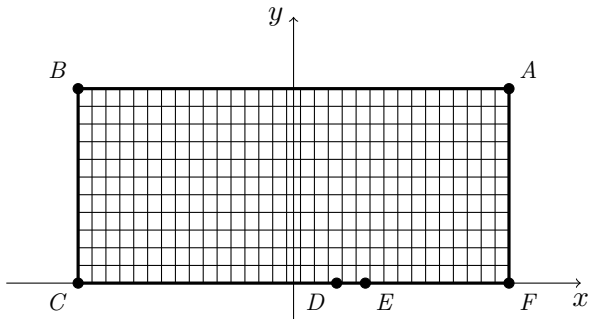

Figure 3.4: Auxiliary geometry

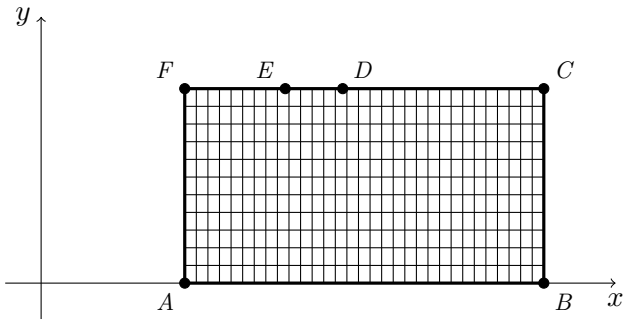

Figure 3.5: Final geometry

and A with 180° angles. To this end, we break down the problem into the following two steps:

1. find the mapping f_1 which transforms the initial geometry shown in Fig. 3.3 to the auxiliary geometry shown in Fig. 3.4.

2. find the mapping f_2 which transforms the auxiliary geometry to the final geometry depicted in Fig. 3.5.

The initial geometry is a generalized quadrilateral defined by $Q := \{\Omega_w; A, B, C, F\}$ resembling the domain of system (3.31)–(3.36). The auxiliary geometry, defined by $R := \{\Omega_z; \tilde{a}+i\tilde{b}, -\tilde{a}+i\tilde{b}, -\tilde{a}, \tilde{a}\}$, is a rectangle symmetrically placed about the y-axis in z-plane depicted in Fig. 3.4.

The first step itself can be broken down into three steps. We first find the mapping f_{11} which maps Q to upper half plane denoted by H^+. Mapping f_{11} is given by inverse Schwarz-Christoffel transformation [71]:

$$f_{11}(w) = C_0 + C \int_{w_0}^{w} \prod_{i=1}^{6} (\zeta - w_i)^{\frac{\alpha_i}{\pi}} d\zeta, \tag{3.97}$$

where $\alpha_i, i = 1, \cdots, 6$ are the interior angles of w_i vertices in counter-clockwise order, C and C_0 are complex constants and w_0 is the image of the axes center in the target domain. The process of finding unknown parameters in (3.97) is known as Schwarz-Christoffel parameter problem [37].

The mapping f_{11} transforms vertices A,B,C and F into z_1, z_2, z_3 and z_4 which are laid in order on the real axis.

Next we use the Möbius transformation, f_{12}, to reorder z_1, z_2, z_3 and z_4 so that they are placed at $\frac{1}{k}$, $-\frac{1}{k}$, -1 and 1, respectively for some $k \in (0, 1)$. This transformation is essential to the next step.

The next step is to find mapping f_{13} to map the domain represented by H^+ and critical points in $\frac{1}{k}$, $-\frac{1}{k}$, -1 and 1 onto an auxiliary domain R.

This transformation is given by elliptic integral of the first kind [71],

$$f_{13}(z) = \int_0^z \frac{d\zeta}{\sqrt{1-\zeta^2}\sqrt{1-k^2\zeta^2}}, \tag{3.98}$$

where k is uniquely defined by the aspect ratio of the rectangle R. By preassigning k, the aspect ratio of the rectangle R is given by:

$$\frac{\tilde{b}}{2\tilde{a}} = \frac{K(k)}{K'(k)}, \tag{3.99}$$

where $K(k)$ is the complete elliptic integral of the first kind and $K'(k)$ is complete complementary elliptic integral of the first kind, [90]:

$$K(k) = \int_0^1 \frac{d\zeta}{\sqrt{1-\zeta^2}\sqrt{1-k^2\zeta^2}} \tag{3.100}$$

$$K'(k) = \int_0^{\frac{1}{k}} \frac{d\zeta}{\sqrt{1-\zeta^2}\sqrt{1-k^2\zeta^2}}. \tag{3.101}$$

The ratio $\frac{K(k)}{K'(k)}$ for $k \in (0, 1)$ can be found from the table given in [1] or numerical calculation. Therefore, the composition of f_{11}, f_{12} and f_{13} construct mapping f_1,

$$f_1(z) = f_{13} \circ f_{12} \circ f_{11}(z). \tag{3.102}$$

Transformation from auxiliary geometry to final geometry can be easily carried out by the following linear mapping performing rotation, translation and stretching:

$$f_2(z) = \frac{1}{\tilde{b}} z + 1 - \frac{\tilde{a}}{\tilde{b}} + i,$$

where $\tilde{a}$ and $\tilde{b}$ are calculated as $\tilde{a} = 1.7017$ and $\tilde{b} = 2.1079$.

Finally, the mapping $g(z)$ from the initial geometry to the final geometry is given by the composition of the mapping f_2 and the inverse mapping f_1, as follows:

$$g(z) := f_2 \circ f_1(z).$$

Calculation of the forward and inverse Schwarz-Christoffel mappings require certain numerical considerations. These considerations are well implemented it SC Toolbox for MATLAB written by T. A. Driscoll [37, 36], which is our main tool in the numerical calculation of the function $g(z)$. We can now proceed to the design of the PDE backstepping boundary observer in the new coordinate system.

3.5 Observer Design for the Transformed System

The observer synthesis follows the same method that we used in section 3.3 with an important difference that the modified system has a modified geometry which corresponds to a cylindrical domain in three dimensions. This domain is depicted in Fig. 3.6.

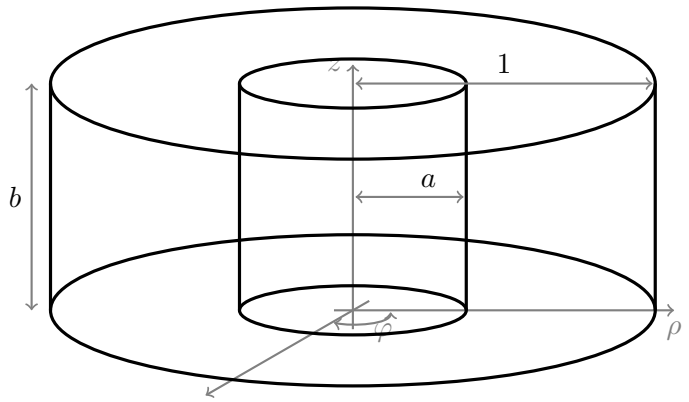

Figure 3.6: Mapped domain structure

The major features that differentiate the domain shown in Fig. 3.6 from the original domain structure are:

- The heating power is applied from the inside boundary and is absorbed through the outside boundary.
- Lower and upper boundaries are isolated,
- A Neumann boundary condition defines the amount of the heat power applied to the domain while the outside boundary is kept at a constant temperature,
- A Dirichlet boundary condition describes the outside boundary of the cylinder.
- The structure is symmetric with respect to both φ and z axes

These conditions result in a PDE equation for the heat distribution problem which is simpler than the equation for heat distribution in the original system.

$$u_t = u_{\rho\rho} + \frac{1}{\rho} u_\rho, \tag{3.103}$$

where $a \leq \rho \leq 1$ and boundary conditions are as follows:

$$u(1) = 0 \tag{3.104}$$

$$u_\rho(a) = \delta U \tag{3.105}$$

$$u(a) = Measurement. \tag{3.106}$$

With these modifications, the resulting PDE backstepping design is much easier than the original problem. We propose the following observer for the system (3.103):

$$\hat{u}_t = \hat{u}_{\rho\rho} + \frac{1}{\rho}\hat{u}_\rho + \ell(\rho)\left(u(a) - \hat{u}(a)\right) \tag{3.107}$$

$$\hat{u}(1) = 0 \tag{3.108}$$

$$\hat{u}_\rho(a) = \delta U + \ell_a\left(u(a) - \hat{u}(a)\right), \tag{3.109}$$

where $\ell(\rho)$, and ℓ_a, are the coefficients to be designed. Define the observer error:

$$\tilde{u}(\rho) = u(\rho) - \hat{u}(\rho), \qquad \rho \in (a, 1) \tag{3.110}$$

which satisfies the following PDE:

$$\tilde{u}_t = \tilde{u}_{\rho\rho} + \frac{1}{\rho}\tilde{u}_\rho - \ell(\rho)\tilde{u}(a) \tag{3.111}$$

$$\tilde{u}(1) = 0 \tag{3.112}$$

$$\tilde{u}_\rho(a) = -\ell_a\tilde{u}(a). \tag{3.113}$$

Equations (3.111)–(3.113) define the observer error dynamics. The coefficients $\ell(\rho)$ and ℓ_a should be designed to stabilize (3.111). We look for an integral transformation of the following form:

$$\tilde{u}(\rho) = \tilde{w}(\rho) - \int_a^\rho P(\rho, \zeta)\tilde{w}(\zeta)\zeta d\zeta, \tag{3.114}$$

that transforms (3.111)–(3.113) into the following exponentially stable target system with desired dynamics:

$$\tilde{w}_t = \tilde{w}_{\rho\rho} + \frac{1}{\rho}\tilde{w}_\rho - \lambda^2\tilde{w} \tag{3.115}$$

$$\tilde{w}(1, z) = 0 \tag{3.116}$$

$$\tilde{w}_\rho(a, z) = 0. \tag{3.117}$$

The function $P(\rho,\zeta)$ is the kernel of the integral equation proposed in (3.114). The parameter λ defines the observer convergence speed. Applying the standard PDE backstepping observer design, we obtain the following result:

Theorem 8. *Consider the PDE observer error dynamic defined by* (3.111) *along with the integral transformation* (3.114) *that transform the error dynamics into* (3.115)–(3.117)*, where* $P(\rho,\zeta)$ *as the kernel of the integral transformation with* $a \leq \zeta \leq \rho \leq 1$*. Then observer parameters* $\ell(\rho)$ *and* ℓ_a *can be explicitly calculated by kernel function,* $P(\rho,\zeta)$*, and the kernel function itself can be calculated by solving the following PDE equation:*

$$P_{\rho\rho}(\rho,\zeta)+\frac{1}{\rho}P_{\rho}(\rho,\zeta)+\lambda^2 P(\rho,\zeta)=P_{\zeta\zeta}(\rho,\zeta)+\frac{1}{\zeta}P_{\zeta}(\rho,\zeta), \tag{3.118}$$

with the following boundary conditions:

$$P(\rho,\rho)=\frac{1}{2}\lambda^2\Big(1-\frac{1}{\rho}\Big) \tag{3.119}$$

$$P(1,\zeta)=0. \tag{3.120}$$

Proof. We start by taking of time derivative of integral transformation (3.114) and substituting w_t with its description in (3.115).

$$\begin{aligned}\tilde{u}_t=&\tilde{w}_t-\int_a^{\rho}P(\rho,\zeta)\Big(\tilde{w}_{\zeta\zeta}+\frac{1}{\zeta}\tilde{w}_{\zeta}-\lambda^2\tilde{w}\Big)\zeta d\zeta\\ =&\tilde{w}_{\rho\rho}+\frac{1}{\rho}\tilde{w}_{\rho}-\lambda^2\tilde{w}\\ &-\int_a^{\rho}P(\rho,\zeta)\zeta\tilde{w}_{\zeta\zeta}d\zeta-\int_a^{\rho}P(\rho,\zeta)\tilde{w}_{\zeta}d\zeta+\int_a^{\rho}P(\rho,\zeta)\lambda^2\zeta\tilde{w}d\zeta.\end{aligned}$$

It follows that

$$\begin{aligned}\int_a^{\rho}P(\rho,\zeta)\zeta\tilde{w}_{\zeta\zeta}d\zeta=&\Big(P(\rho,\zeta)\zeta\tilde{w}_{\zeta}\Big|_a^{\rho}-\int_a^{\rho}\Big(P(\rho,\zeta)+\zeta P_{\zeta}(\rho,\zeta)\Big)\tilde{w}_{\zeta}d\zeta\\ =&\rho P(\rho,\rho)\tilde{w}_{\rho}(\rho)-aP(\rho,a)\tilde{w}_{\rho}(a)-\int_a^{\rho}P(\rho,\zeta)\tilde{w}_{\zeta}d\zeta\\ &-\Big(P_{\zeta}(\rho,\zeta)\zeta\tilde{w}\Big|_a^{\rho}+\int_a^{\rho}\Big(P_{\zeta}(\rho,\zeta)+\zeta P_{\zeta\zeta}(\rho,\zeta)\Big)\tilde{w}d\zeta\\ =&\rho P(\rho,\rho)\tilde{w}_{\rho}(\rho)-\int_a^{\rho}P(\rho,\zeta)\tilde{w}_{\zeta}d\zeta\\ &-\rho P_{\zeta}(\rho,\rho)\tilde{w}(\rho)+aP_{\zeta}(\rho,a)\tilde{w}(a)\\ &+\int_a^{\rho}\Big(P_{\zeta}(\rho,\zeta)+\zeta P_{\zeta\zeta}(\rho,\zeta)\Big)\tilde{w}d\zeta,\end{aligned}$$

which results the following equation for $\tilde{u}_t$,

$$\begin{aligned}\tilde{u}_t =&\tilde{w}_{\rho\rho} + \frac{1}{\rho}\tilde{w}_\rho - \lambda^2\tilde{w} - \rho P(\rho,\rho)\tilde{w}_\rho(\rho)\\ &+ \rho P_\zeta(\rho,\rho)\tilde{w}(\rho) - aP_\zeta(\rho,a)\tilde{w}(a)\\ &- \int_a^\rho \Big(P_\zeta(\rho,\zeta) + \zeta P_{\zeta\zeta}(\rho,\zeta) - \lambda^2\zeta P(\rho,\zeta)\Big)\tilde{w}d\zeta.\end{aligned} \tag{3.121}$$

For calculation of $\tilde{u}_\rho$, we take derivative of both sides of (3.114). The next step is calculating $\tilde{u}_\rho$.

$$\begin{aligned}\tilde{u}_\rho(\rho) &= \tilde{w}_\rho(\rho) - \frac{d}{d\rho}\int_a^\rho P(\rho,\zeta)\tilde{w}(\zeta)\zeta d\zeta\\ &= \tilde{w}_\rho(\rho) - \rho P(\rho,\rho)\tilde{w}(\rho) - \int_a^\rho P_\rho(\rho,\zeta)\tilde{w}(\zeta)\zeta d\zeta.\end{aligned} \tag{3.122}$$

We can use (3.122) to find the value of $\tilde{u}_\rho(\rho)$ at $\rho = a$

$$\begin{aligned}\tilde{u}_\rho(a) &= \tilde{w}_\rho(a) - aP(a,a)\tilde{w}(a) - \int_a^a P_\rho(a,\zeta)\tilde{w}(\zeta)\zeta d\zeta\\ &= -aP(a,a)\tilde{w}(a).\end{aligned} \tag{3.123}$$

But from (3.113) and the fact that $\tilde{u}(a) = \tilde{w}(a)$, we have

$$\tilde{u}_\rho(a) = -\ell_a\tilde{u}(a) = -\ell_a\tilde{w}(a). \tag{3.124}$$

So we obtain the relation between the observer parameter ℓ_a and the observer kernel function $P(\rho,\zeta)$ as follows:

$$\ell_a = aP(a,a). \tag{3.125}$$

The next step is calculating $\tilde{u}_{\rho\rho}$. To find $\tilde{u}_{\rho\rho}$, we take derivative of (3.122):

$$\begin{aligned}\tilde{u}_{\rho\rho}(\rho) =&\tilde{w}_{\rho\rho}(\rho) - \frac{d}{d\rho}\Big(\rho P(\rho,\rho)\tilde{w}(\rho)\Big) - \frac{d}{d\rho}\int_a^\rho P_\rho(\rho,\zeta)\tilde{w}(\zeta)\zeta d\zeta\\ =&\tilde{w}_{\rho\rho}(\rho) - P(\rho,\rho)\tilde{w}(\rho) - \rho P(\rho,\rho)\tilde{w}_\rho(\rho)\\ &- \rho\tilde{w}(\rho)\frac{d}{d\rho}P(\rho,\rho) - \rho P_\rho(\rho,\rho)\tilde{w}(\rho)\\ &- \int_a^\rho P_{\rho\rho}(\rho,\zeta)\tilde{w}(\zeta)\zeta d\zeta.\end{aligned} \tag{3.126}$$

Now by substituting the equation for $\tilde{u}_t$, $\tilde{u}_\rho$ and $\tilde{u}_{\rho\rho}$ which are calculated in

(3.121), (3.122) and (3.126) in (3.111), the equation (3.111) becomes:

$$\begin{aligned}
&\tilde{w}_{\rho\rho}+\frac{1}{\rho}\tilde{w}_\rho-\lambda^2\tilde{w}-\rho P(\rho,\rho)\tilde{w}_\rho(\rho)+\rho P_\zeta(\rho,\rho)\tilde{w}(\rho)-aP_\zeta(\rho,a)\tilde{w}(a)\\
&\quad-\int_a^\rho\Big(P_\zeta(\rho,\zeta)+\zeta P_{\zeta\zeta}(\rho,\zeta)-\lambda^2\zeta P(\rho,\zeta)\Big)\tilde{w}d\zeta\\
&=\tilde{u}_{\rho\rho}+\frac{1}{\rho}\tilde{u}_\rho-\ell(\rho)\tilde{u}(a)\\
&=\tilde{w}_{\rho\rho}(\rho)-P(\rho,\rho)\tilde{w}(\rho)-\rho P(\rho,\rho)\tilde{w}_\rho(\rho)-\rho\tilde{w}(\rho)\frac{d}{d\rho}P(\rho,\rho)\\
&\quad-\rho P_\rho(\rho,\rho)\tilde{w}(\rho)-\int_a^\rho P_{\rho\rho}(\rho,\zeta)\tilde{w}(\zeta)\zeta d\zeta\\
&\quad+\frac{1}{\rho}\tilde{w}_\rho(\rho)-P(\rho,\rho)\tilde{w}(\rho)-\int_a^\rho\frac{1}{\rho}P_\rho(\rho,\zeta)\tilde{w}(\zeta)\zeta d\zeta\\
&\quad-\ell(\rho)\tilde{u}(a).
\end{aligned}\tag{3.127}$$

Replacing $\tilde{u}(a)$ with $\tilde{w}(a)$ and rearranging (3.127) we arrive to the following equation:

$$\begin{aligned}
&\Big(\ell(\rho)-aP_\zeta(\rho,a)\Big)\tilde{w}(a)\\
&+2\Big(\rho\frac{d}{d\rho}P(\rho,\rho)+P(\rho,\rho)-\frac{1}{2}\lambda^2\Big)\tilde{w}(\rho)\\
&+\int_a^\rho\Big(P_{\rho\rho}(\rho,\zeta)+\frac{1}{\rho}P_\rho(\rho,\zeta)-P_{\zeta\zeta}(\rho,\zeta)-\frac{1}{\zeta}P_\zeta(\rho,\zeta)+\lambda^2P(\rho,\zeta)\Big)\tilde{w}(\zeta)\zeta d\zeta=0.
\end{aligned}\tag{3.128}$$

From the equation 3.128 it would appear that the kernel function $P(\rho,\zeta)$ has to satisfy the following PDE

$$\begin{aligned}
P_{\rho\rho}(\rho,\zeta)+\frac{1}{\rho}P_\rho(\rho,\zeta)+\lambda^2P(\rho,\zeta)&=P_{\zeta\zeta}(\rho,\zeta)+\frac{1}{\zeta}P_\zeta(\rho,\zeta)\\
\rho\frac{d}{d\rho}P(\rho,\rho)+P(\rho,\rho)&=\frac{1}{2}\lambda^2.
\end{aligned}\tag{3.129}$$

The boundary condition introduced in (3.129) can be written as follows:

$$\frac{d}{d\rho}(\rho P(\rho,\rho))=\frac{1}{2}\lambda^2.\tag{3.130}$$

It is easy to see that the solution of (3.130) has a solution as follow:

$$P(\rho,\rho)=\frac{1}{2}\lambda^2+\frac{c}{\rho}\,,\tag{3.131}$$

where c is a constant to be defined. It is easy to see that (3.128) also provide the relation between output injection function $\ell(\rho)$ and kernel function $P(\rho,\zeta)$ as follows:

$$\ell(\rho)=aP_\zeta(\rho,a).\tag{3.132}$$

An additional boundary condition comes by substituting $\rho = 1$ in (3.114):

$$\tilde{u}(1) = \tilde{w}(1) - \int_a^1 P(1,\zeta)\tilde{w}(\zeta)\zeta d\zeta, \tag{3.133}$$

that results the following boundary condition:

$$P(1,\zeta) = 0, \tag{3.134}$$

which also means

$$P(1,1) = 0. \tag{3.135}$$

By using (3.135) in (3.131), we find the constant c,

$$c = -\frac{1}{2}\lambda^2. \tag{3.136}$$

Combining (3.129), (3.131), (3.136) and (3.134), the PDE equation that describes the kernel function $P(\rho,\zeta)$ is obtain as follows:

$$P_{\rho\rho}(\rho,\zeta) + \frac{1}{\rho}P_\rho(\rho,\zeta) + \lambda^2 P(\rho,\zeta) = P_{\zeta\zeta}(\rho,\zeta) + \frac{1}{\zeta}P_\zeta(\rho,\zeta),$$

with following boundary conditions:

$$P(\rho,\rho) = \frac{1}{2}\lambda^2\Big(1 - \frac{1}{\rho}\Big)$$
$$P(1,\zeta) = 0.$$

The domain for kernel function $P(\rho,\zeta)$ is described by

$$a \leq \rho \leq 1$$
$$a \leq \zeta \leq \rho.$$

□

Exponential stability of the target system (3.115)–(3.117) and invertibility of the transformation (3.114) imply exponential stability of (3.111) [111].

The domain of the PDE equation describing the integral kernel function is depicted in Fig. 3.7. Boundary conditions are shown at each boundary. The relation between observer parameters $\ell(\rho)$ and ℓ_a with bottom boundary and point at $\rho = \zeta = a$ are given as well. The observer parameter ℓ_a can be obtained from

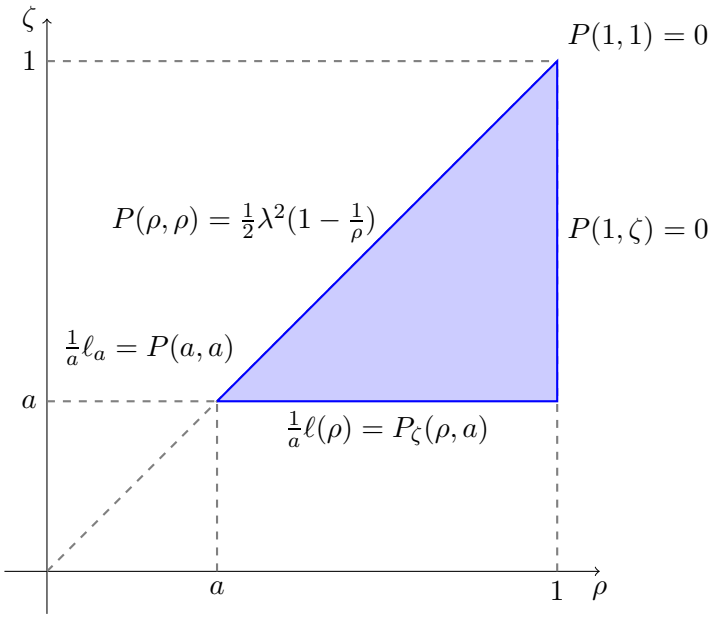

Figure 3.7: Domain of the observer kernel function, $P(\rho,\zeta)$

(3.125) and the boundary condition (3.119) as follows:

$$\ell_a = \frac{1}{2}\lambda^2\Big(a-1\Big). \tag{3.137}$$

To complete the design we need to find the observer output injection parameter $\ell(\rho)$, given in (3.132). For that, however, we need the kernel function $P(\rho,\zeta)$ which requires solving the PDE equation (3.118). Since we do not have an analytical solution, we proceed with a numerical approach. The process of development of a numerical method to solve (3.118) and to calculate the observer parameters are discussed in detail in the next chapter.

3.6 Summary

In this chapter we considered the observer design problem for the PCR-LOC microchip described using partial differential equations. In the first place, we proposed an extension of the backstepping approach to observer design for two dimensional parabolic PDE systems. The extension is made possible thanks to the introduction of a conformal transformation that significantly affects the boundary conditions and that reduces the two-dimensional problem to one in one-dimension that has a simpler solution. We showed that the use of the conformal transformation technique, significantly reduces the calculation burden and makes it possible to design a PDE backstepping boundary observer in a complex cylindrical domain structure.

Simulating the PDE observer is not trivial and needs developing numerical techniques to solve for the kernel function and to calculate the coupled PDE system consisted of main system and the observer. The next chapter addresses the development of the numerical techniques and simulation of the PDE observer.

Chapter 4

Simulation

4.1 Introduction

The process of simulation of the PDE observer and controller designs are neither as simple nor as well developed as their ODE counterparts. A brief introduction of available numerical methods for PDE equations can be found in a paper by Tadmor [113]. To be able to simulate the results of PDE backstepping boundary observer design discussed in Chapter 3, some preliminary results are necessary:

- Full definition of the observer, requires the solution of observer kernel function $P(\rho, \zeta)$ and hence arriving to $\ell(\rho)$ and ℓ_a.
- Simulation of the interconnected system, composed of the PCR model and the PDE backstepping boundary observer requires the development of a numerical technique.
- A precise characterization experiment in addition to a customized signal processing technique is required to verify the simulation results.

In this chapter, the required steps to evaluate the PDE backstepping boundary observer design are presented and the results are discussed in detail.

4.2 Observer Kernel Calculation

At the first step, we need to calculate the observer kernel function which defines the observer parameters. To this end, we use the Finite Difference (FD) method. To

proceed, we first uniformly discretize the domain space to N points ($N-1$ sections),

$$\Delta\rho = \Delta\zeta = h = \frac{(1-a)}{N-1}. \tag{4.1}$$

Let matrix $\bar{P}_{(N)\times(N)}$ stands for discretized $P(\rho,\zeta)$,

$$\bar{P}_{ij} = P(\bar{\rho}_i, \bar{\zeta}_j), \qquad 1 \le i,j \le N$$

where each element $\bar{P}_{ij}$ of the matrix $\bar{P}$ corresponds to the $P(\bar{\rho}_i,\bar{\zeta}_j)$ and, $\bar{\rho}_i = 1-(i-1)h$ and $\bar{\zeta}_j = 1-(j-1)h$ are the elements of the discretized ρ and ζ axes,

$$\bar{\rho} = [1 \ (1-h) \ (1-2h) \cdots (1-(N-1)h)]_{1\times N}$$
$$\bar{\zeta} = [1 \ (1-h) \ (1-2h) \cdots (1-(N-1)h)]_{1\times N}.$$

From (4.1), it is clear that $(1-(N-1)h) = a$.

The partial derivatives can be calculated using central-difference approximation as follows:

$$\begin{aligned}
P_\rho(\bar{\rho}_i,\bar{\zeta}_j) &\simeq \frac{1}{2h}\Big(P(\bar{\rho}_{i+1},\bar{\zeta}_j) - P(\bar{\rho}_{i-1},\bar{\zeta}_j)\Big)\\
P_{\rho\rho}(\bar{\rho}_i,\bar{\zeta}_j) &\simeq \frac{1}{h^2}\Big(P(\bar{\rho}_{i+1},\bar{\zeta}_j) - 2P(\bar{\rho}_i,\bar{\zeta}_j) + P(\bar{\rho}_{i-1},\bar{\zeta}_j)\Big)\\
P_\zeta(\bar{\rho}_i,\bar{\zeta}_j) &\simeq \frac{1}{2h}\Big(P(\bar{\rho}_i,\bar{\zeta}_{j+1}) - P(\bar{\rho}_i,\bar{\zeta}_{j-1})\Big)\\
P_{\zeta\zeta}(\bar{\rho}_i,\bar{\zeta}_j) &\simeq \frac{1}{h^2}\Big(P(\bar{\rho}_i,\bar{\zeta}_{j+1}) - 2P(\bar{\rho}_i,\bar{\zeta}_j) + P(\bar{\rho}_i,\bar{\zeta}_{j-1})\Big).
\end{aligned} \tag{4.2}$$

The central-difference approximation has an error of $O(h^2)$ [44]. Substituting the partial derivatives in (3.118) with their approximations in (4.2) and representing them as the elements of matrix $\bar{P}$, we have

$$(1+\frac{h}{2\bar{\rho}_i})\bar{P}_{i+1,j} + (1-\frac{h}{2\bar{\rho}_i})\bar{P}_{i-1,j} + \lambda^2h^2\bar{P}_{i,j} = (1-\frac{h}{2\bar{\zeta}_j})\bar{P}_{i,j-1} + (1+\frac{h}{2\bar{\zeta}_j})\bar{P}_{i,j+1}. \tag{4.3}$$

Equation (4.3) can be rearranged to arrive to the following equation to calculate $\bar{P}_{i,j+1}$,

$$\bar{P}_{i,j+1} = \beta_1\bar{P}_{i+1,j} + \beta_2\bar{P}_{i-1,j} + \beta_3\bar{P}_{i,j} + \beta_4\bar{P}_{i,j-1}, \tag{4.4}$$

where $2 \le i \le j \le N-1$ and the coefficients β_1, β_2, β_3 and β_4 are as follows:

$$\begin{aligned}
\beta_1 &= \frac{(1+\frac{h}{2\bar{\rho}_i})}{(1+\frac{h}{2\bar{\zeta}_j})} \qquad \beta_2 = \frac{(1-\frac{h}{2\bar{\rho}_i})}{(1+\frac{h}{2\bar{\zeta}_j})}\\
\beta_3 &= \frac{\lambda^2h^2}{(1+\frac{h}{2\bar{\zeta}_j})} \qquad \beta_4 = -\frac{(1-\frac{h}{2\bar{\zeta}_j})}{(1+\frac{h}{2\bar{\zeta}_j})}.
\end{aligned} \tag{4.5}$$

Boundary conditions (3.119) and (3.120), define boundary points in $\bar{P}_{1,j}$ and $\bar{P}_{i,i}$ as follows:

$$\bar{P}_{1,j} = 0 \tag{4.6}$$

$$\bar{P}_{i,i} = \frac{1}{2}\lambda^2(1 - \frac{1}{1-(i-1)h}), \tag{4.7}$$

where $1 \leq i, j \leq N$. A most important decision here is to define out of boundary values in such a way that numerical calculations are stable. Instability in numerical calculation of the kernel function was reported in [8, 10, 14]. By properly defining the out of boundary values, the numerical calculation can be rendered stable [62]. This idea can be summarized as follows:

$$\bar{P}_{i+1,i} = \bar{P}_{i,i} = \frac{1}{2}\lambda^2(1 - \frac{1}{1-(i-1)h}). \tag{4.8}$$

$\bar{P}$ can be calculated using the recurrence equation (4.4) and the predefined values (4.6), (4.7) and (4.8). The first point to calculate is $\bar{P}_{2,3}$ followed by $\bar{P}_{3,4}$ and continued up to $\bar{P}_{N-1,N}$. Then start again with calculation of $\bar{P}_{2,4}$ followed by $\bar{P}_{2,5}$ and continued upto $\bar{P}_{N-2,N}$. This calculation should be repeated until all the unknown elements of $\bar{P}$ are defined (in total there are $(N-1)(N-2)/2$ unknown elements in matrix $\bar{P}$). We calculated the approximate kernel function $\bar{P}$ using MATLAB and depicted the results in Fig. 4.1. After that all elements of $\bar{P}$ are fully known, we can numerically calculate discretized $\ell(\rho)$. Let $\ell(\bar{\rho}_i)$ stands for value of $\ell(\rho)$ at discretized points $\bar{\rho}_i$ on ρ axis. We use backward difference to calculate the output injection function $\ell(\bar{\rho}_i)$. It is straight forward to see that

$$\ell(\bar{\rho}_i) = \frac{a}{h}\Big(\bar{P}_{i,N} - \bar{P}_{i,N-1}\Big), \quad 1 \leq i \leq N-1 \tag{4.9}$$

For $\ell(\bar{\rho}_N)$, we write:

$$\ell(\bar{\rho}_N) = \ell(a) = \frac{a}{h}\Big(\bar{P}_{N,N} - \bar{P}_{N,N-1}\Big). \tag{4.10}$$

Referring to our technique to define the out of boundary values which is stated in (4.8), for $\bar{P}_{N,N-1}$ we have:

$$\bar{P}_{N,N-1} = \bar{P}_{N-1,N-1}. \tag{4.11}$$

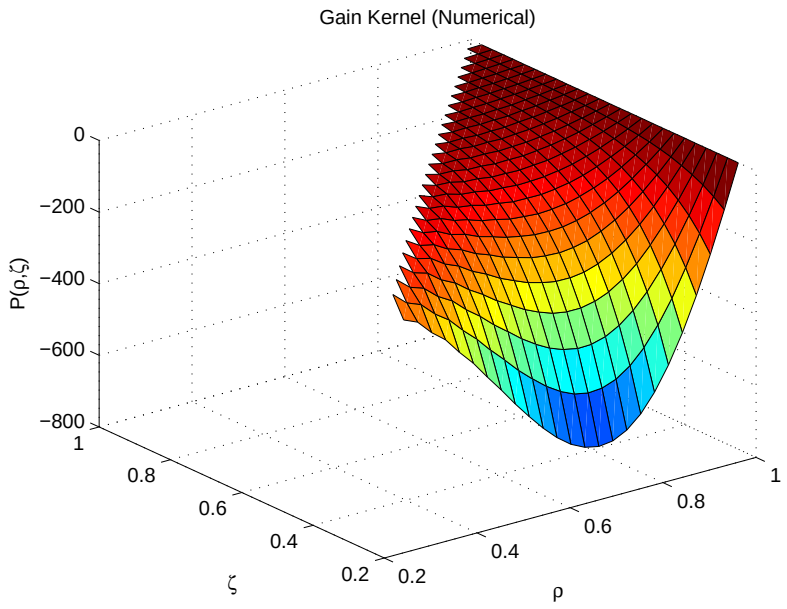

Figure 4.1: Approximate kernel $\bar{P}(\rho, \zeta)$

Using boundary condition (3.119) and (4.11) into (4.10), we have

$$\begin{aligned}
\ell(\bar{\rho}_N) &= \frac{a}{h}\Big(\frac{1}{2}\lambda^2(1-\frac{1}{\bar{\rho}_N}) - \frac{1}{2}\lambda^2(1-\frac{1}{\bar{\rho}_{N-1}})\Big) \\
&= \frac{a\lambda^2}{2h}\Big(\frac{1}{\bar{\rho}_{N-1}} - \frac{1}{\bar{\rho}_N}\Big) \\
&= \frac{a\lambda^2}{2}\Big(\frac{-1}{(1-(N-1)h)(1-(N-2)h)}\Big) \\
&= \frac{-\lambda^2}{2(a+h)}.
\end{aligned} \tag{4.12}$$

We summarize (4.9) and (4.12) as follows:

$$\ell(\bar{\rho}_i) = \begin{cases} \frac{a}{h}(\bar{P}_{i,N} - \bar{P}_{i,N-1}) & 1 \le i \le N-1 \\ \\ \frac{-\lambda^2}{2(a+h)} & i = N. \end{cases} \tag{4.13}$$

The observer output injection function $\ell(\rho)$ for different values of λ is calculated and depicted in Fig. 4.2. Fig. 4.2 illustrates the fact that to have an observer with faster dynamics, a larger output injection gain is needed. The bouncing values of $\ell(\rho)$ close to the activation boundary ($\rho = 0.25$) is due to the error in numerical calculations. Because of the stable numerical calculation, this fluctuation is bounded and does not increase in magnitude as the discretization steps become smaller.

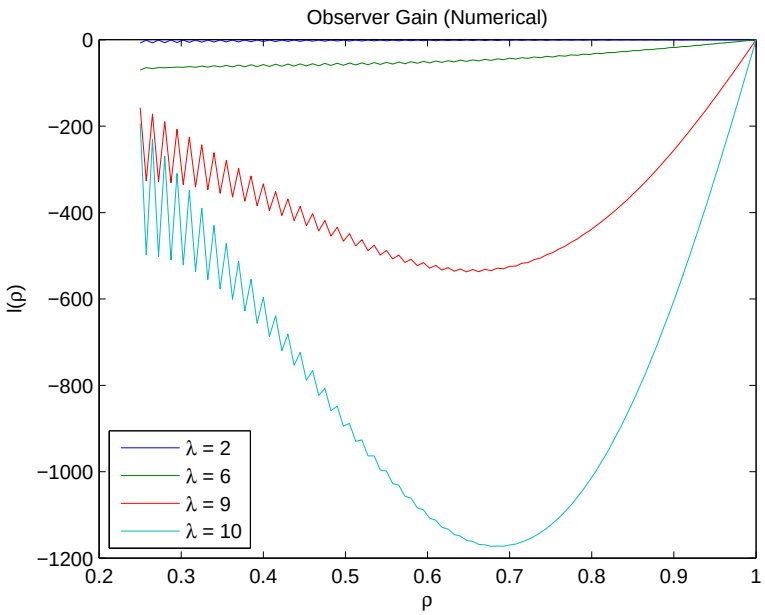

Figure 4.2: Observer parameter $\ell(\rho)$ for different values of λ

4.3 Developing the Numerical Technique

4.3.1 Introduction

We chose the compact difference scheme as the core of our technique. The well-known compact difference scheme has been proved to be capable of resulting in accurate and stable solutions while providing lower computational cost with using minimal stencil width [76, 89, 70]. We step-by-step present how to develop a Sixth-Order accurate discretization technique for a selected PDE backstepping boundary observer which is designed for a thermal system.

4.3.2 Proposed Approach

Interconnection between the observer and the thermal system is depicted in Fig. 4.3. It is clear that, the PDE backstepping observer estimates the heat distribution in the whole domain just by measuring the input actuation signal and the temperature of the actuation boundary layer. In this work, we only discretize the spatial domain for the chosen interconnected PDE problem. The resulting finite dimensional linear system can be easily and accurately simulated in temporal domain using available simulation tools, i.e MATLAB.

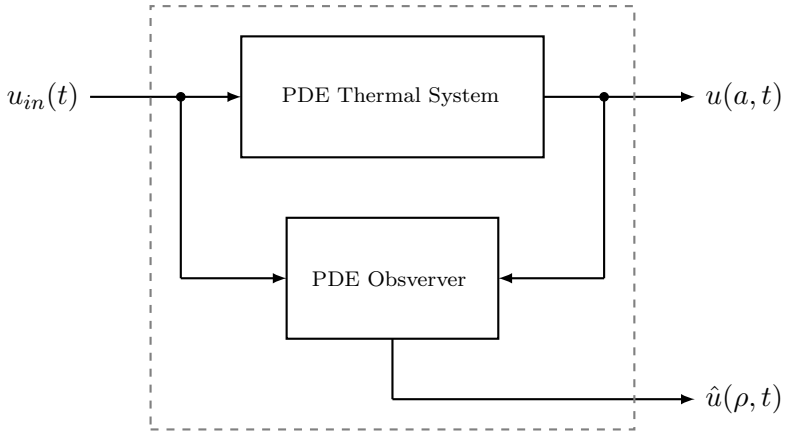

Figure 4.3: Interconnection between the PDE observer and the thermal system

One should note here that if temporal discretization be desired as well, the choosing of a right time discretization step has a great importance. Beside the spatial discretization, the stability of the calculation totally related to the chosen temporal discretization method. Some methods imply a maximum time step to result in stable calculation while some other methods, i.e *Crank-Nicolson* method, unconditionally result in stable calculation.

We begin with discretization of the spatial domain ($a \leq \rho \leq 1$) by defining N equidistant computational grids ρ_j with step size h as follows,

$$\rho_j = a + (j-1)h \quad , \quad h = \frac{1-a}{N-1} \quad , \quad j = 1, \cdots, N \tag{4.14}$$

Next, we define $\hat{U}(j)$ to be the restriction of $\hat{u}(\rho,t)$ to $\rho = \rho_j$

$$\hat{U}(j) = \hat{u}(\rho_j, t) \qquad , \qquad j = 1, \cdots, N \tag{4.15}$$

Similarly, $\hat{U}_\rho(j)$ and $\hat{U}_{\rho\rho}(j)$ are restrictions of $\hat{u}_\rho(\rho_j,t)$ and $\hat{u}_{\rho\rho}(\rho_j,t)$ to $\rho = \rho_j$,

$$\hat{U}_\rho(j) = \hat{u}_\rho(\rho_j,t) \ , \quad \hat{U}_{\rho\rho}(j) = \hat{u}_{\rho\rho}(\rho_j,t) \ , \quad j = 1, \cdots, N \tag{4.16}$$

The indices $j = 2, \cdots, N-1$ correspond to the points in the interior of the computational domain. The indices $j = 1$ and $j = N$ correspond to the points on the boundary of the computational domain where we can apply the Dirichlet and the Neumann conditions to get

$$\hat{U}(1) = \hat{u}(a) \tag{4.17}$$

$$\hat{U}_\rho(1) = \hat{u}_\rho(a,t) = u_{in}(t) + \ell_a \left(u(a) - \hat{u}(a)\right) \tag{4.18}$$

$$\hat{U}(N) = \hat{u}(1,t) = 0. \tag{4.19}$$

collecting all the computational grids in a vector, $\bar{\rho}$,:

$$\bar{\rho} = \begin{bmatrix} \rho_1 \\ \rho_2 \\ \rho_3 \\ \vdots \\ \rho_N \end{bmatrix} = \begin{bmatrix} a \\ a+h \\ a+2h \\ \vdots \\ a+Nh \end{bmatrix} \tag{4.20}$$

we define discrete solution vectors $\hat{U}$, $\hat{U}_\rho$ and $\hat{U}_{\rho\rho}$ to be the vectors consisted of all $\hat{U}(j)$, $\hat{U}_\rho(j)$ and $\hat{U}_{\rho\rho}(j)$,

$$\hat{U} = \begin{bmatrix} \hat{u}(\rho_1) \\ \hat{u}(\rho_2) \\ \vdots \\ \hat{u}(\rho_N) \end{bmatrix}, \ \hat{U}_\rho = \begin{bmatrix} \hat{u}_\rho(\rho_1) \\ \hat{u}_\rho(\rho_2) \\ \vdots \\ \hat{u}_\rho(\rho_N) \end{bmatrix}, \ \hat{U}_{\rho\rho} = \begin{bmatrix} \hat{u}_{\rho\rho}(\rho_1) \\ \hat{u}_{\rho\rho}(\rho_2) \\ \vdots \\ \hat{u}_{\rho\rho}(\rho_N) \end{bmatrix} \tag{4.21}$$

From (4.17), (4.18) and (4.19), it is clear that $\hat{U}(1) = \hat{u}(a)$, $\hat{U}(N) = \hat{u}(1)$ and $\hat{U}_\rho(1) = \hat{u}_\rho(a)$.

4.3.3 Compact Finite Difference Scheme

To reduce the accumulation of errors in calculation of the distributed variables over very long periods of time and far distances, the numerical algorithm must be highly accurate. High-order compact finite difference scheme have been introduced for this purpose.

Generally, high-order finite difference schemes can be classified into two main categories: explicit schemes and Padé-type or compact schemes [77]. Explicit schemes compute the numerical derivatives directly at each grid by using a large stencils, while compact schemes obtain all the numerical derivatives along a grid line using smaller stencils and solving a linear system of equations. Experience has shown that compact schemes are much more accurate than the corresponding explicit scheme of the same order [77]. In this paper, the compact finite difference scheme of six-order is chosen as the core method which can yield excellent accuracy with minimum stencil width. We begin by developing the formulation for first derivatives for interior points of discretized spatial domain.

First Derivatives of Interior Points

To evaluate the first derivatives at the interior nodes, we assume that they can be obtained by solving the following tridiagonal system

$$\alpha f'_{i-1} + f'_i + \alpha f'_{i+1} = b\frac{f_{i+2} - f_{i-2}}{4h} + a\frac{f_{i+1} - f_{i-1}}{2h} \tag{4.22}$$

where $i = 2, \cdots, N-1$ and the unknown coefficients α, a and b are obtained by matching the Tylor expansion up to $\mathcal{O}(h^4)$. α-family of fourth-order tridiagonal schemes (4.22) is obtained with

$$a = \frac{2}{3}(\alpha + 2) \qquad , \qquad b = \frac{1}{3}(4\alpha - 1) \tag{4.23}$$

Also, the truncation error of (4.22) is $-\frac{4}{5!}(3\alpha - 1)h^4 f^{(5)}$. Choosing $\alpha = 0$ gives the explicit fourth-order scheme for the first derivative while by choosing $\alpha = \frac{1}{3}$ the scheme becomes sixth-order accurate [77], in which case $a = \frac{14}{9}$ and $b = \frac{1}{9}$. So we have the following formula

$$\frac{1}{3}f'_{i-1} + f'_i + \frac{1}{3}f'_{i+1} = \frac{1}{h}(-\frac{1}{36}f_{i-2} - \frac{14}{18}f_{i-1} + \frac{14}{18}f_{i+1} + \frac{1}{36}f_{i+2}) \tag{4.24}$$

to calculated the interior points.

First Derivatives of Boundary Points

For nearby boundary grids, the approximation formula for the derivatives of a non-periodic problems can be derived by one-sided schemes [43, 76].

Lets consider that, we are going to discretize the spatial domain in N points. At boundary point 1, a sixth-order formula is [43]:

$$f'_1 + \alpha f'_2 = \frac{1}{h}(c_1 f_1 + c_2 f_2 + \cdots + c_7 f_7) \tag{4.25}$$

where $\alpha = 5$, $c_1 = \frac{-197}{60}$, $c_2 = \frac{-5}{12}$, $c_3 = 5$, $c_4 = \frac{-5}{3}$, $c_5 = \frac{5}{12}$, $c_6 = \frac{-1}{20}$ and $c_7 = 0$.

At boundary point 2, the sixth-order formula is [43]:

$$\alpha f'_1 + f'_2 + \alpha f'_3 = \frac{1}{h}(c_1 f_1 + c_2 f_2 + \cdots + c_7 f_7) \tag{4.26}$$

where $\alpha = \frac{2}{11}$, $c_1 = \frac{-20}{33}$, $c_2 = \frac{-35}{132}$, $c_3 = \frac{34}{33}$, $c_4 = \frac{-7}{33}$, $c_5 = \frac{2}{33}$, $c_6 = \frac{-1}{132}$ and $c_7 = 0$.

At boundary point $N-1$, the sixth-order formula is [43]:

$$\alpha f'_{N-2} + f'_{N-1} + \alpha f'_N = \frac{1}{h}(c_1 f_N + c_2 f_{N-1} + \cdots + c_7 f_{N-6}) \tag{4.27}$$

where $\alpha = \frac{2}{11}$. The remaining coefficients are those given for point 2 with the opposite signs.

At boundary point N, the sixth-order formula is [43]:

$$\alpha f'_{N-1} + f'_N = \frac{1}{h}(c_1 f_N + c_2 f_{N-1} + \cdots + c_7 f_{N-6}) \tag{4.28}$$

where $\alpha = 5$. The remaining coefficients are those given for point 1 with the opposite signs.

Matrix Representation of the Compact Difference Scheme of the Six-Order

Now everything is ready to describe the relation between $\hat{U}_\rho$ and $\hat{U}$ in matrix form using the relation given for the first derivatives at interior and boundary points.

The relation between $\hat{U}_\rho$ and $\hat{U}$ can be given as the following matrix equation:

$$E \cdot \hat{U}_\rho = \frac{1}{h} F \cdot \hat{U} \tag{4.29}$$

where matrix E and F are calculated using (4.24)– (4.28) as follows,

$$E = \begin{bmatrix} 1 & 5 & 0 & & \cdots & & 0 \\ \frac{2}{11} & 1 & \frac{2}{11} & 0 & & & \\ 0 & \frac{1}{3} & 1 & \frac{1}{3} & 0 & & \vdots \\ & \ddots & \ddots & \ddots & \ddots & \ddots & \\ \vdots & & 0 & \frac{1}{3} & 1 & \frac{1}{3} & 0 \\ & & & 0 & \frac{2}{11} & 1 & \frac{2}{11} \\ 0 & & \cdots & & 0 & 5 & 1 \end{bmatrix}_{N \times N} \tag{4.30}$$

and

$$F = \begin{bmatrix} -\frac{197}{60} & -\frac{5}{12} & 5 & -\frac{5}{3} & \frac{5}{12} & -\frac{1}{20} & 0 & \cdots & 0 \\ -\frac{20}{33} & -\frac{35}{132} & \frac{34}{33} & -\frac{7}{33} & \frac{2}{33} & -\frac{1}{132} & 0 & & \\ -\frac{1}{36} & -\frac{14}{18} & 0 & \frac{14}{18} & \frac{1}{36} & 0 & 0 & & \\ 0 & -\frac{1}{36} & -\frac{14}{18} & 0 & \frac{14}{18} & \frac{1}{36} & 0 & & \vdots \\ & \ddots & \ddots & \ddots & \ddots & \ddots & \ddots & \ddots & \\ \vdots & & 0 & -\frac{1}{36} & -\frac{14}{18} & 0 & \frac{14}{18} & \frac{1}{36} & 0 \\ & & 0 & 0 & -\frac{1}{36} & -\frac{14}{18} & 0 & \frac{14}{18} & \frac{1}{36} \\ & & 0 & \frac{1}{132} & -\frac{2}{33} & \frac{7}{33} & -\frac{34}{33} & \frac{35}{132} & \frac{20}{33} \\ 0 & \cdots & 0 & \frac{1}{20} & -\frac{5}{12} & \frac{5}{3} & -5 & \frac{5}{12} & \frac{197}{60} \end{bmatrix}_{N\times N} \tag{4.31}$$

By multiplying both sides of (4.29) to E^{-1}, we have,

$$\hat{U}_\rho = \frac{1}{h} E^{-1} F \hat{U} \doteq A \hat{U} \tag{4.32}$$

The same 6 order first degree compact scheme can be used again to calculate the second order derivatives which results:

$$\hat{U}_{\rho\rho} = A \hat{U}_\rho = A^2 \hat{U} \tag{4.33}$$

4.3.4 Main Results

State-Space Description of The Spatially-Discretized PDE Backstepping Boundary Observer

To this end, the first and second derivatives of estimated heat distribution in discretized spatial domain is calculated in matrix form in (4.29)–(4.33). The next step is to collect the inputs in an input vector and address the boundary conditions and internal interconnection in matrix form.

First, we form the input vector using the observer inputs:

$$U_i = \begin{bmatrix} u_{in} \\ u(a) \end{bmatrix} \tag{4.34}$$

Recalling (4.19), the boundary condition (3.119) implies following condition to vector $\hat{U}$:

$$\hat{U}(N) = \hat{u}(1) = 0$$

In addition, recalling (4.18), the boundary condition (3.120) can be transformed to the following matrix equation for vector $\hat{U}$:

$$\begin{aligned}\hat{U}_\rho(1) &= U_i(1) + \ell_a\, U_i(2) - \ell_a\, \hat{U}(1) \\ &= \begin{bmatrix} 1 & \ell_a \end{bmatrix} \cdot U_i + \begin{bmatrix} -\ell_a & 0_{1\times(N-1)} \end{bmatrix} \cdot \hat{U}\end{aligned} \tag{4.35}$$

The discrete representation of observer output injection function $\ell(\rho)$ is as follows:

$$\bar{\ell} = \begin{bmatrix} \ell(\rho_1) \\ \ell(\rho_2) \\ \vdots \\ \ell(\rho_N) \end{bmatrix}_{N\times 1} \tag{4.36}$$

where $\bar{\ell}(1) = \ell(a)$ and $\bar{\ell}(N) = \ell(1)$.

To include the boundary conditions in the matrix equation, we partition off (4.32) to separate the actuation boundary:

$$\hat{U}_\rho = \begin{bmatrix} A1_{1\times N} \\ A2_{(N-1)\times N} \end{bmatrix} \cdot \hat{U} = \begin{bmatrix} \hat{U}_\rho(1) \\ A2 \cdot \hat{U} \end{bmatrix} \tag{4.37}$$

The equation (4.37) can be rewritten in the following form:

$$\hat{U}_\rho = \begin{bmatrix} 0_{1\times N} \\ A2 \end{bmatrix} \cdot \hat{U} + \begin{bmatrix} 1 \\ 0_{(N-1)\times 1} \end{bmatrix} \cdot \hat{U}_\rho(1) \tag{4.38}$$

Substituting (4.35) into (4.38) and rearranging the result, we have

$$\begin{aligned}\hat{U}_\rho = &\left(\begin{bmatrix} 0_{1\times N} \\ A2 \end{bmatrix} + \begin{bmatrix} 1 \\ 0_{(N-1)\times 1} \end{bmatrix} \cdot \begin{bmatrix} -\ell_a & 0_{1\times(N-1)} \end{bmatrix} \right) \cdot \hat{U} \\ &+ \left(\begin{bmatrix} 1 \\ 0_{(N-1)\times 1} \end{bmatrix} \cdot \begin{bmatrix} 1 & \ell_a \end{bmatrix} \right) \cdot U_i\end{aligned} \tag{4.39}$$

Now the second derivative $\hat{U}_{\rho\rho}$ can be easily described by state vector $\hat{U}$ and input vector U_i using (4.33) and (4.39). we obtain,

$$\begin{aligned}\hat{U}_{\rho\rho} = &A \cdot \left(\begin{bmatrix} 0_{1\times N} \\ A2 \end{bmatrix} + \begin{bmatrix} 1 \\ 0_{(N-1)\times 1} \end{bmatrix} \cdot \begin{bmatrix} -\ell_a & 0_{1\times(N-1)} \end{bmatrix} \right) \cdot \hat{U} \\ &+ A \cdot \left(\begin{bmatrix} 1 \\ 0_{(N-1)\times 1} \end{bmatrix} \cdot \begin{bmatrix} 1 & \ell_a \end{bmatrix} \right) \cdot U_i\end{aligned} \tag{4.40}$$

The term $\frac{1}{\rho}\hat{u}_\rho$ can be written in discrete form as:

$$\begin{bmatrix} \frac{1}{\rho_1} & & \\ & \ddots & \\ & & \frac{1}{\rho_N} \end{bmatrix} \cdot \hat{U}_\rho \tag{4.41}$$

The term $\ell(\rho)(u(a) - \hat{u}(a))$ in discrete form becomes,

$$\left(\bar{\ell} \cdot \begin{bmatrix} 0 & 1 \end{bmatrix}_{1\times 2}\right) \cdot U_i - \left(\bar{\ell} \cdot \begin{bmatrix} 1 & 0_{1\times(N-1)} \end{bmatrix}_{1\times N}\right) \cdot \hat{U} \tag{4.42}$$

Finally by using the (4.39), (4.40) and (4.42) in the observer PDE (3.118), we arrive to the finite dimensional estimation of observer described in (3.118)–(3.120),

$$\hat{U}_t = A_d\,\hat{U} + B_d\,U_i. \tag{4.43}$$

where

$$\begin{aligned} A_d = & \left(A + \begin{bmatrix} \frac{1}{\rho_1} & & \\ & \ddots & \\ & & \frac{1}{\rho_N} \end{bmatrix} \right) \cdot \\ & \left(\begin{bmatrix} 0_{1\times N} \\ A2 \end{bmatrix} + \begin{bmatrix} 1 \\ 0_{(N-1)\times 1} \end{bmatrix} \cdot \begin{bmatrix} -\ell_a & 0_{1\times(N-1)} \end{bmatrix} \right) \\ & - \bar{\ell} \cdot \begin{bmatrix} 1 & 0_{1\times(N-1)} \end{bmatrix} \end{aligned} \tag{4.44}$$

and

$$\begin{aligned} B_d = & \left(A + \begin{bmatrix} \frac{1}{\rho_1} & & \\ & \ddots & \\ & & \frac{1}{\rho_N} \end{bmatrix} \right) \cdot \begin{bmatrix} 1 \\ 0_{(N-1)\times 1} \end{bmatrix} \cdot \begin{bmatrix} 1 & \ell_a \end{bmatrix} \\ & + \left(\bar{\ell} \cdot \begin{bmatrix} 0 & 1 \end{bmatrix} \right) \end{aligned} \tag{4.45}$$

The same technique derived in this section can be more easily apply to describe the finite dimensional estimation of original system (3.31)–(3.35).

4.4 Simulation Results

In the spatial-discretization techniques that we developed in previous section, we only dealt with the normalized system. Both the spatial and the temporal variables

Table 4.1: The parameter values used in the PDE observer simulation

Parameter	Symbol	Value	Unit
Inner radius of the cylinder	a	0.25	mm
Outside radius of the cylinder	r_{out}	1	mm
Thermal diffusivity in domain	κ	6.08×10^{-7}	m^2/s
Cylinder height	z	2	mm

were being scaled in the normalization process. From these arguments one could conclude that to apply the given design technique to the actual system, the aforementioned scaling factors should be considered in the equations. Consequently, the temporal and the spatial variables should be rescaled to their original spaces. To rescale the spatial and the temporal variables, we need to know some physical parameters of the actual system. Table 4.1 shows the physical parameters considered for the simulation.

The input signal is considered as a unit step signal with an amplitude of -114.7063 and an offset of zero which is delayed for one second. The negative sign in the input signal's amplitude implies that the heat flux flow on the actuation boundary is from the outside to the inside. In fact, the values of the input signal is in accordance to applying one watt power to the system. The simulation process is defined for a duration of 2 seconds with 25 points time steps, which results in 0.08-second temporal resolution. Similarly, the same number of the discretization points, $N = 25$, are chosen for the discretization of the spatial variable ρ. The initial condition is given by $u_0(\rho) = \cos(\frac{5}{2}\pi\rho^2)$.

By considering the defined initial condition and by applying the defined input signal, The evolution of heat distribution during the time is simulated and is depicted in Fig. 4.4

As you see, the temperature started to increase after that the input pulse applied at time $= 1s$.

The Fig. 4.5 shows the temperature changes at the actuation boundary.

As it is visible, the initial temperature falls before the input pulse is applied to the system which cause subsequent increase in the temperature at the boundary.

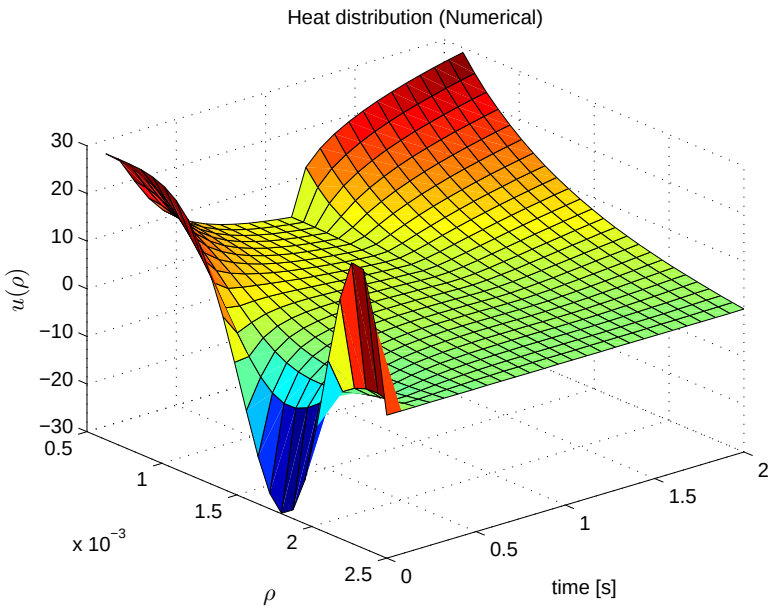

Figure 4.4: Heat distribution in the domain

For the observer system, we used a decay rate faster than the original system by choosing $\lambda = 9$. The output injection function, $\ell(\rho)$, is numerically calculated for the chosen decay rate and is depicted in Fig. 4.6.

Fig. 4.7, shows the result of the simulation for the interconnected structure composed of the observer and the system, originally shown in Fig. 4.3. It is clear that at first, the observer struggled to follow the heat distribution generated by the initial condition. But it quickly converged to the heat distribution in the system and later it provided a fair estimation of the heat-distribution in the system when input pulse applied to the system.

Finally, to evaluate the performance of the designed observer, we calculated the L^2-norm of the estimation error and depicted it in Fig. 4.8.

Specifically, the L^2-norm of the estimation error exponentially converged to zero and the small peak in the estimation error caused by the step input is well damped later.

4.4.1 Verifying with Experimental Results

We used the experimental data that originally collected during the thermal characterization of the PCR-LOC microchip to verify the PDE observer. The temperature

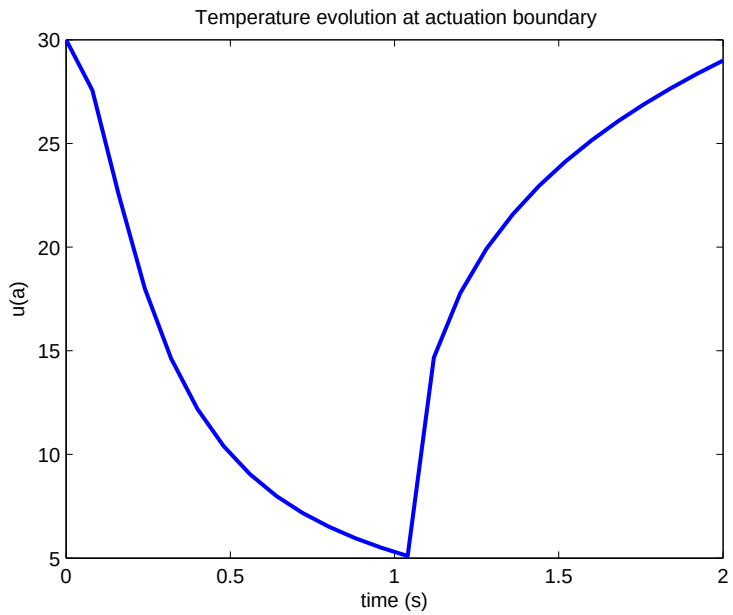

Figure 4.5: Temperature evolution at the actuation boundary

characterization of a microfluidic chip is a challenging task due to the difficulty in the measuring of the temperature without causing significant perturbation [53].

One way of the temperature measurement in the microfluidic systems is by using the thermochromic liquid crystals (TLCs) [53, 23, 97]. The temperature changes are detected by color changes in the TLCs. The color change effects are caused by the interference and the diffraction of the reflected and the scattered light. The TLC color change bandwidth can be customized, but there exists a trade-off between resolution (sensitivity) in the temperature measurement and the range of the temperatures that can be measured [97]. The temperature fluctuations are in the range of 1–2°C. We choose to employ a TLC that changes color over a tight range to ensure a sufficient resolution in the temperature measurement. Color changes in R58C3W TLC is shown in Fig. 4.9. The left figure is when the temperature is out of the bandwidth and the right figure shows the TLC when the temperature is within its bandwidth

In our experiment we used R58C3W TLC (Hallcrest Glenview, IL, USA) with maximum sensitivity at 58°C, corresponding to annealing stage of PCR process in our experiment. The TLC has a milky white color at a room temperature and turns red as the temperature reaches the lowest temperature of its color change

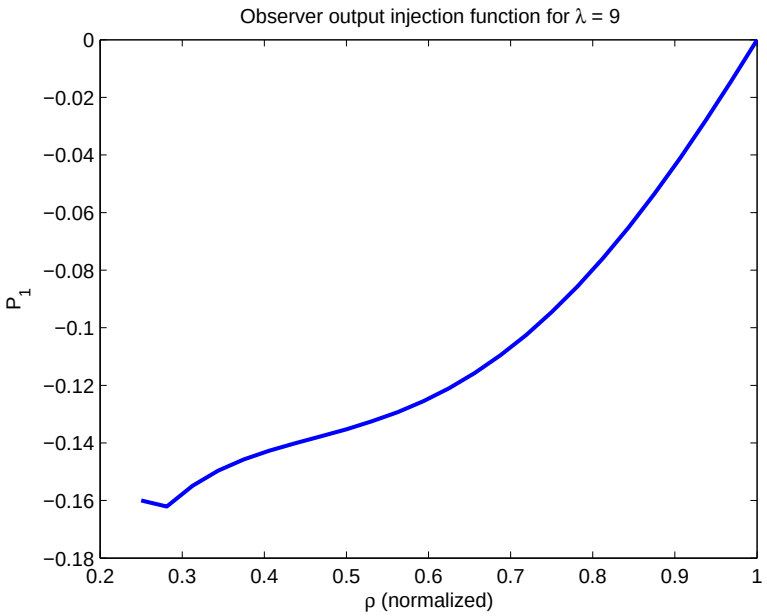

Figure 4.6: Observer parameter $\ell(\rho)$ for $\lambda = 9$

range, green at the second temperature threshold, and blue at the third. When the temperature rises above the color range of the TLCs (about 70°C for the TLCs used here), its color returns to the original milky white. Temperature/hue curve for the R58C3W TLC are measured using precise characterization experiments and then extrapolated and the result is depicted at Fig. 4.10.

We used SPZ-50 optical microscope and L-150R60 fiber optical illuminator with ring light in addition to a 3.1MP CCD camera to perform the experiment and to record the color changes of the TLC during PCR cycling.

The video was originally recorded in RGB color space. To achieve meaningful data from the sequence of the images, we calculated the mean R, G and B values for the image region describing TLC in each frame of the captured video and transformed them to a HSV color space.

We used Blaze Video Decompiler included in Blaze Media software package to extract the frames from the recorded WMV video file.

There have been several approaches to transform RGB to HSV color space [49, 101]. For the purpose of this study, a simplified version of the Hay and Hollingsworth's formulation is used and implemented using the MATLAB function

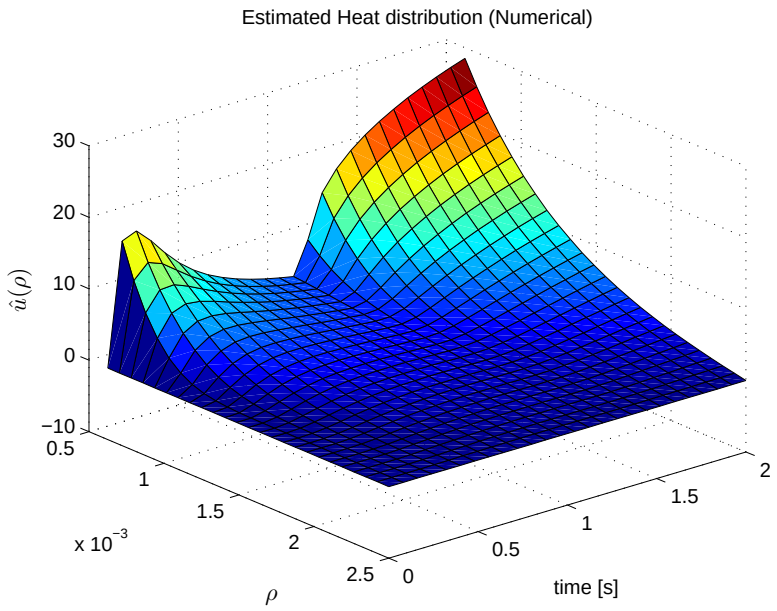

Figure 4.7: Heat distribution estimated by the observer

"rgb2hsv" .

$$
\begin{aligned}
V &= max(R,G,B) \\
S &= \frac{V - min(R,G,B)}{V} \\
H &= \frac{1}{6}\begin{cases} (G-B)\dfrac{1}{S} & \text{if } R > B,G \\ 2 + (B-R)\dfrac{1}{S} & \text{if } G > R,B \\ 4 + (R-G)\dfrac{1}{S} & \text{if } B > R,G \end{cases}
\end{aligned}
\tag{4.46}
$$

where R, G, B, H, S and V are red, green, blue, hue, saturation and intensity values, respectively.

Finally, we used TLC calibration curves to map the hue variations to temperature variations. The results are depicted in Fig. 4.12.

The top graph shows the input current applied to heater ring. A PI controller closed in a loop with the heater temperature reading and receiving cycling reference signal, provided this signal to the heater. Bottom graph presents the observer results compared to the TLC mapped hue readout from inside the chamber. TLC has a very limited bandwidth and only provided valid hue change for temperature from about 50°C to 70°C. For temperatures out of this range it has a constant milky color

The TLC temperature reading within its bandwidth (about 50°C to 70°C) veri-

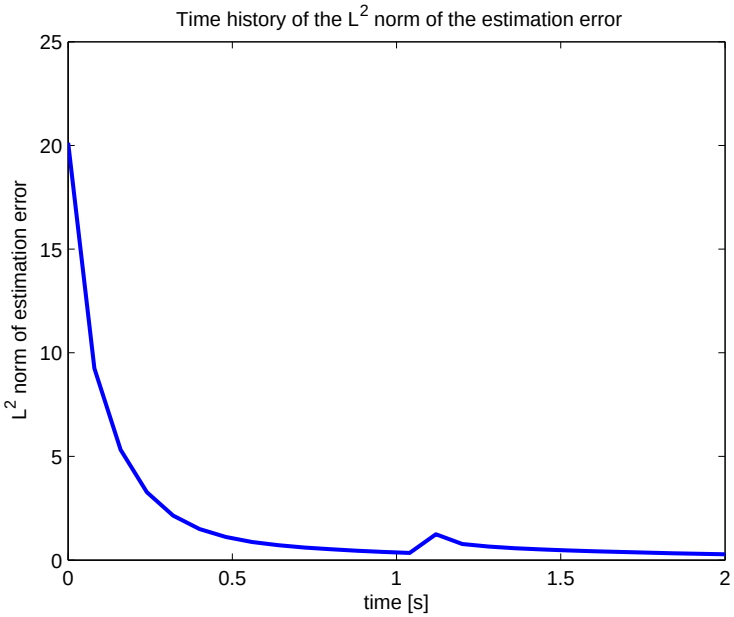

Figure 4.8: Time history of the L^2-norm of the estimation error

fies the accuracy of the observer.

4.5 Summary

In this chapter, the PDE backstepping boundary observer designed in chapter 3 is fully defined after the calculation of the observer kernel function $P(\rho, \zeta)$. Moreover, to enable the simulation of the PDE backstepping boundary observer, a systematic discretization approach for numerical solution of interconnected PDE control system is developed and presented.

The compact finite difference method is used as the core technique for discretization which is known to be able to provide reliable and accurate approximations with low amount of calculation effort. The performance of the designed observer is evaluated through inspection of the L^2-norm after simulation. In addition, the PDE backstepping boundary observer experimentally verified by implementing a TLC sensor inside the reaction chamber and recording and mapping the color change of the TLC sensor.

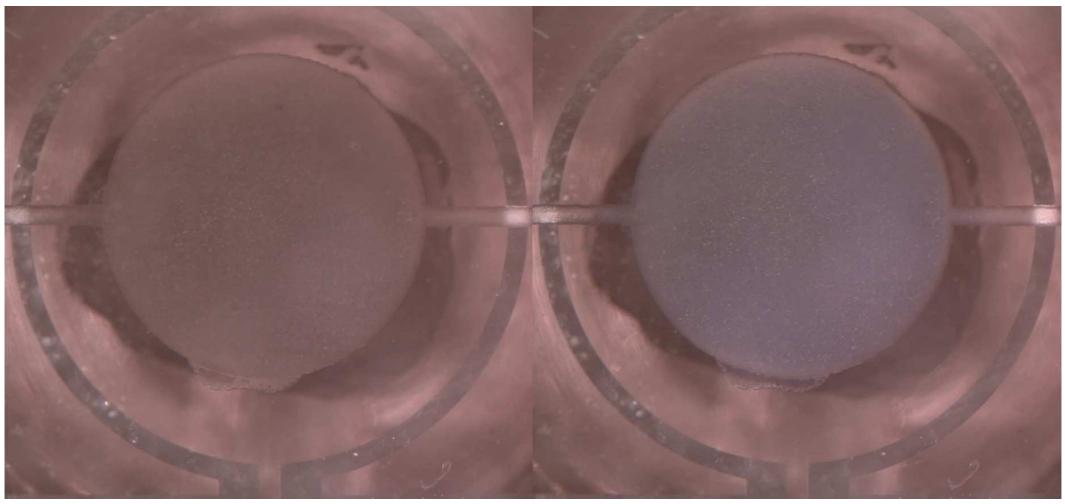

Figure 4.9: Color change in R58C3W TLC

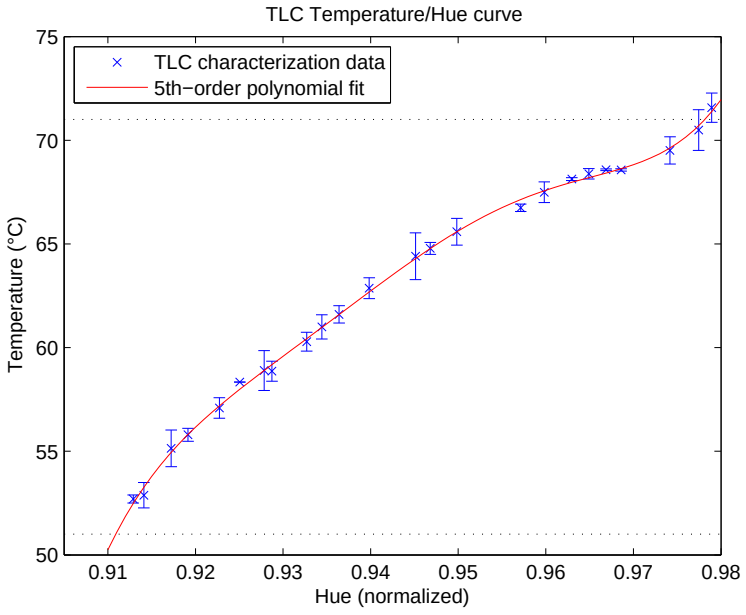

Figure 4.10: Temperature/hue curve for the R58C3W TLC

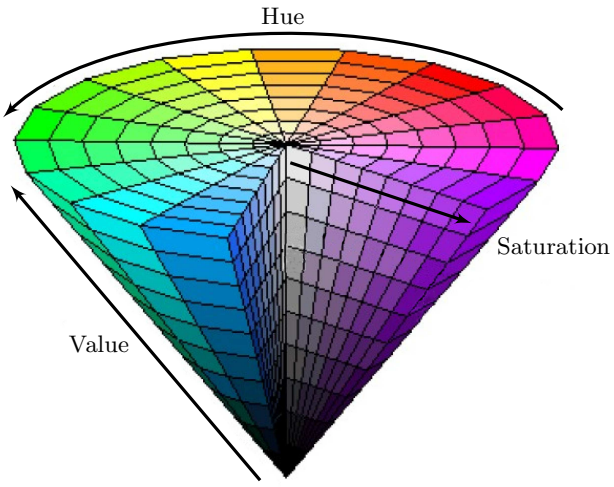

Figure 4.11: Illustration of the HSV color space

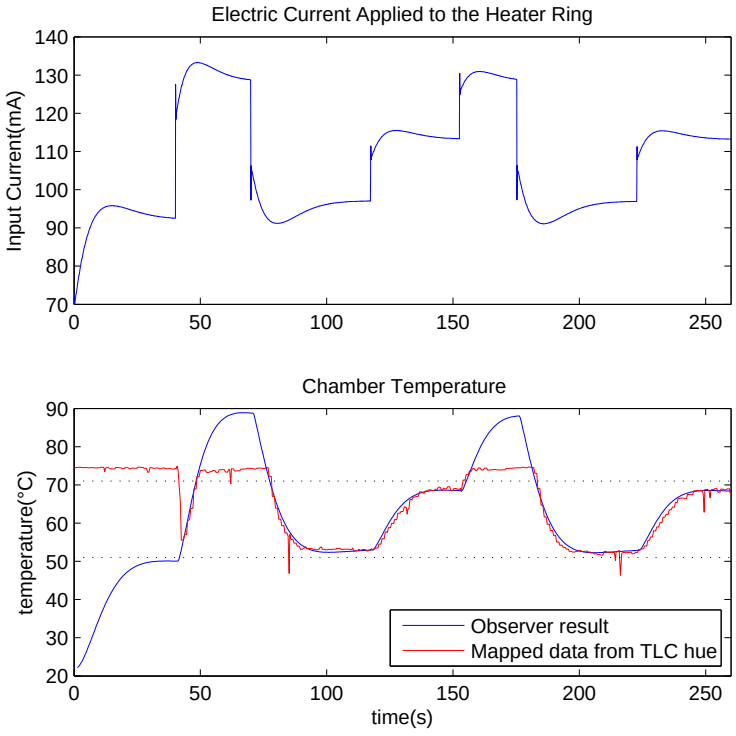

Figure 4.12: Experimental results

Chapter 5

Implementation

5.1 Introduction

In this chapter, we implement our PDE backstepping boundary observer on the PCR-LOC microchip with a controller previously designed using the classical methods. The controller used a simplified model in which nonlinear terms related to the interfacing circuit are compensated.

5.1.1 Experimental Setup

The experimental setup is composed of the PCR mircochip, interfacing circuit, Data Acquisition (DAQ) and power supply modules as shown in Fig. 5.1. The DAQ, USB-6009 by National Instrument, is linked and powered by a laptop computer via a USB serial link. The computer is running real-time control application under Simulink.

Interfacing circuit is connected to Platinum heater via a two-wire connector where it applies actuation signal and at the same time it measures the temperature by sensing platinum heater electric resistance. Interfacing circuit performs required signal conditioning for heater ring actuation and sensing and also for the temperature sensor installed on Heatsink attached to PCR microchip. The conditioned signals are converted to digital values using a DAQ device (National Instrument USB-6009) and are passed to computer via DAQ devices USB connection. Actuation signal comes in the opposite direction where it is converted to analog electric current by

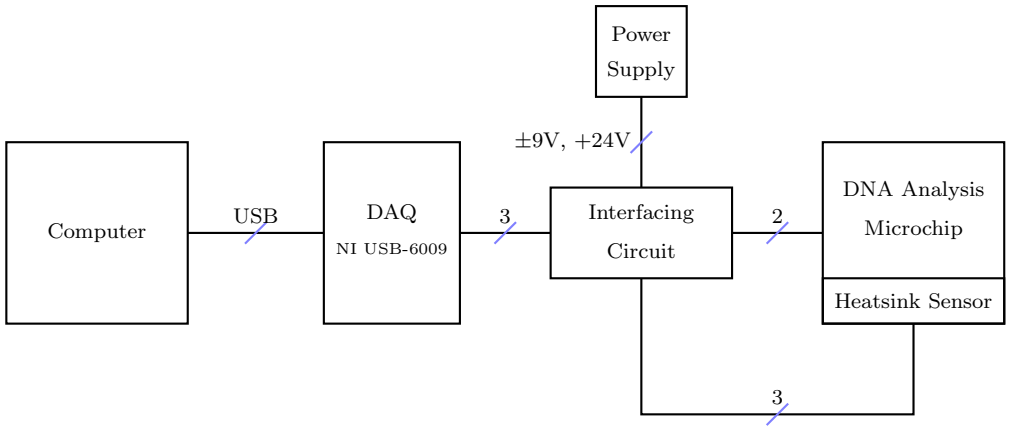

Figure 5.1: Experimental setup

DAQ and it is passed through the heater ring by the electric interfacing circuit.

The electric power for the experiment is provided by an external power supply unit feeding +24V and ±9V to the interfacing module. The interfacing module is connected to the DAQ through three lines, two analog to digital converter (ADC) input channels and one digital to analog converter (DAC) output channel.

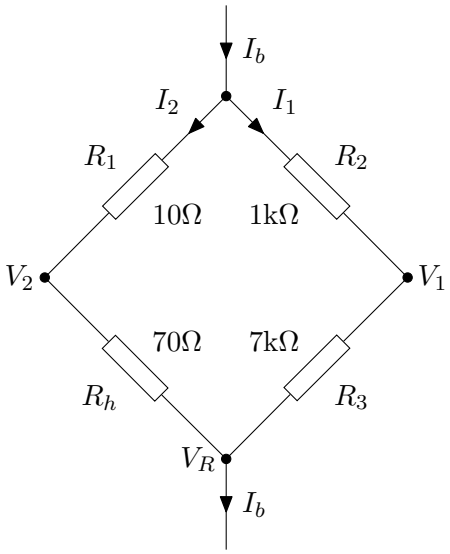

Figure 5.2: Wheatstone bridge circuit

5.2 Interfacing Circuit

The interfacing circuit is present in the form of a printed circuit board (PCB) converting control action signal from DAQ to electric current passing through the thin-film heater on the PCR chip and simultaneously measures the voltage across the heater and handed it DAQ after proper signal conditioning. The control application uses this information to calculate the temperature of the heater in real-time. The interfacing circuit also holds appropriate circuit for measuring the ambient temperature through a solid-state temperature sensor implanted in heatsink.

The core part in interfacing circuit that enables the simultaneous actuation and measurement for collocated control at the boundary is a Wheatstone bridge. The Wheatstone bridge in our design is depicted in Fig. 5.2.

The heater ring has a nominal electrical resistance, R_h, of 70Ω at room temperature, 22°C. Actuation signal is being applied to the heater ring through changing the bridge current, I_b. The Wheatstone bridge resistors R_1, R_2 and R_3 are designed such that about 99% of the bridge current pass through the heater ring. For the electrical current in each leg of the Wheatstone bridge, I_1 and I_2, we have:

$$I_2(R_1 + R_h) = I_1(R_2 + R_3), \tag{5.1}$$

or

$$\frac{I_2}{I_1} = \frac{R_2 + R_3}{R_1 + R_h} \approx 100. \tag{5.2}$$

For the bridge current, I_b, we have:

$$I_b = I_1 + I_2. \tag{5.3}$$

Using (5.2) in (5.3) we arrive to:

$$I_b = I_2(1 + \frac{R_1 + R_h}{R_2 + R_3}) = I_1(1 + \frac{R_2 + R_3}{R_1 + R_h}), \tag{5.4}$$

which results in:

$$\begin{aligned} I_1 &= \frac{R_1 + R_h}{R_1 + R_2 + R_3 + R_h} I_b \\ I_2 &= \frac{R_2 + R_3}{R_1 + R_2 + R_3 + R_h} I_b. \end{aligned} \tag{5.5}$$

The electrical resistance change in the heater ring is measured through measuring the difference voltage on the Wheatstone bridge balanced nodes, V_2 and V_1. For the bridge output voltages we have

$$\begin{aligned} V_2 - V_R &= I_2 R_h \\ V_1 - V_R &= I_1 R_3 \end{aligned} \tag{5.6}$$

Next, by subtracting equations in (5.6), we can eliminate V_R and arrive to:

$$V_2 - V_1 = V_D = I_2 R_h - I_1 R_3, \tag{5.7}$$

where V_D is defined as the difference voltage across the bridge balanced nodes. Using (5.5) in (5.7), we arrive to

$$V_D = V_2 - V_1 = \frac{R_h(R_2 + R_3) - R_3(R_1 + R_h)}{R_1 + R_2 + R_3 + R_h} \times I_b. \tag{5.8}$$

The equation (5.8) describes the relation between the bridge difference voltage, the bridge current and the heater electric resistance. The heater resistance itself is related to heater temperature. The next equation describes the relation between electrical resistance in the heater ring and the heater ring temperature which is a simplified form of the *CallendarVan Dusen* equation:

$$R_h(T) = (1 + \alpha(T - 22))R_h(22) \tag{5.9}$$

where $\alpha = 0.00385$ ohm/ohm/°C is the temperature coefficient of the electrical resistance for the platinum, according to IEC6075 standard, and T is the temperature of the heater ring in °C.

We calibrate the Wheatstone bridge through connecting a 50k potentiometer in parallel with R_3. We tune the potentiometer so that the Wheatstone bridge fully balanced and we have zero difference voltage on the bridge output in the laboratory ambient (the temperature is 22°C or $R_h = R_h(22) = 70\Omega$).

The calibrated Wheatstone bridge implies $V_D = 0$. Using (5.8) we have,

$$R_h(22)(R_2 + R_3) - R_3(R_1 + R_h(22)) = 0, \tag{5.10}$$

or

$$\frac{R_2}{R_3} = \frac{R_1}{R_h(22)} \tag{5.11}$$

Using (5.11) in (5.8), we arrive to the difference voltage equation for the calibrated Wheatstone bridge,

$$V_D = \frac{R_2(R_h(T) - R_h(22))}{R_1 + R_2 + \frac{R_2 R_h(22)}{R_1} + R_h(T)} \times I_b, \tag{5.12}$$

which can also be re-ordered for $R_h(T)$,

$$R_h(T) = \frac{V_D(R_1 + R_2 + \frac{R_2}{R_1}R_h(22)) + R_2 R_h(22) I_b}{R_2 I_b - V_D}. \tag{5.13}$$

The left sides of (5.9) and (5.13) are equal. We arrive to the following results describing the relation between the heater ring temperature and the difference voltage on the Wheatstone bridge,

$$V_D = \frac{R_2 R_h(22)(\alpha(T - 22))}{R_1 + R_2 + R_h(22)(\frac{R_2}{R_1} + 1 + \alpha(T - 22))} \times I_b \tag{5.14}$$

$$T = \frac{V_D(R_1 + R_2 + R_h(22)(\frac{R_2}{R_1} + 1))}{\alpha R_2 R_h(22) I_b - \alpha V_D R_h(22)} + 22. \tag{5.15}$$

By considering the values of the known parameters in (5.14), we can have an approximate relation,

$$V_D \approx 3.32 \times 10^{-2} \times (T - 22) \times I_b, \tag{5.16}$$

which means that for heater temperature change between ambient temperature (22°C) up to 200°C (maximum safe temperature for PDMS) with maximum bridge current of 200mA, we can expect V_D varies from 0 upto 1.18 volt.

This result leads us to select a gain and bias for amplification section of the interfacing circuit. The full design of the interfacing circuit is illustrated in Fig. A.1, available at appendix A.

By selecting a gain of 4.2373 and an offset of 2.5v (provided by the DAQ device), we can have a differential voltage span in $\pm 2.5v$ when heater temperature spans between 22°C and 200°C. This full-scale output voltage is perfect for our DAQ device which has an analog voltage input setting for the range of $\pm 2.5v$.

We chose AD620 instrumentation amplifier, by Analog Devices, as the main amplification stage in the interface circuit design. The gain of the AD620 can be easily adjusted by a resistor, R_G connected to its pin 1 and pin 8. The datasheet of AD620 suggests a gain calculation as follows:

$$R_G = \frac{49.4\text{k}\Omega}{G - 1}. \tag{5.17}$$

Therefore, for $G = 4.2373$, we calculate $R_G = 15.2596\text{k}\Omega$. This resistance can be realized through connecting a 18kΩ resistor and a 100kΩ resistor in parallel (the gain would be $G = 4.2384$).

5.3 Controller Setup

The thermal control system for the PCR-LOC microchip must fulfil very tight specifications associated with the real-world application. These specifications are listed below:

- The heater temperature must not pass the 200°C. This constraint is due to melting points of the PDMS layer which has a direct contact with the heater ring.
- The controller should satisfy a maximum ±1°C on overshoot or undershoot for the chamber's temperature transients. This constraint is required by the DNA amplification protocol.
- The transient time between each temperature stage must be minimized. This is to prevent degradation of the amplification process and to speed-up the overall process duration.

In addition, a distinct property of a PCR-LOC thermal management system is the fact that the thermal cycling is predefined by PCR protocol. In other words, the set-point's trend is available for the whole process time.

From the system properties and the required control specifications, MPC control, also known as receding horizon control, is a good candidate for controlling the PCR-LOC microchip. MPC has the advantage of using a moving time horizon window that has the ability to perform real-time optimization considering both the controlled variables and the fulfilment of the constraints [87, 22, 103].

Moreover, MPC's natural description in discrete form, makes it suitable for the computer simulation and embedded system implementation. However, we cannot ignore the fact that the MPC algorithm is based on numerically solving a constrained optimization problem at each step which requires huge amount of computational resources.

The advantage of the MPC technique for practical applications comes from the fact that measured disturbances, unmeasured disturbances, delay, sampled-data structure, constraints on system's input and output can be easily incorporated in the thesis process.

The major drawbacks of the MPC control is the requirement for a precise model and extensive calculation power demand. The later is due to associated optimization which prevent the implementation in fast systems. Consequently, the MPC control has primarily been applied to systems with slow dynamics.

5.3.1 Inputs and Output Assignment for the Controller

The next step in designing the MPC controller is to identify the measured and unmeasured disturbances, inputs and outputs. The inputs and outputs of the plant should also be grouped in a certain way to be used in the MPC controller design. The diagram in Fig. 5.3 illustrates the input and output assignments of the PCR-LOC model.

Full description of the input and output assignment for each category are as follows:

Measured disturbances

T_{hs}, heatsink temperature, and cte, constant value, are measured disturbances.

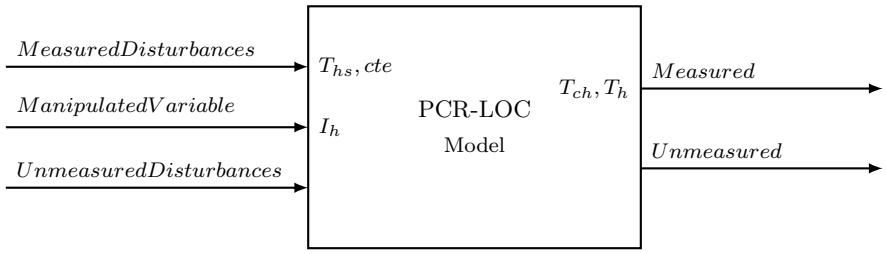

Figure 5.3: Input/output assignment of PCR-LOC model for MPC controller design

The controller cannot adjust them, but uses them for feed-forward compensation. The constant value, *cte* is required to deliver the set-point offset.

Manipulated variables

The controller adjusts I_h, the heater current, in order to achieve its goals.

Unmeasured disturbances

No unmeasured input was considered in our modeling approach.

and the plant outputs are grouped as follows:

Measured outputs

The chamber temperature, T_{ch}, which is provided by the observer is the first measured output. The second measured output is the heater temperature, T_h. The controller uses these inputs to adjust the feedback.

Unmeasured outputs

The controller estimates these based on available measurements and the plant model. The controller can also hold unmeasured outputs at set-points or within constraint boundaries. There is no unmeasured output in our model.

In addition to input and output assignment, the MPC parameters and their associated limitation should be fully defined. In our design, the parameters and constraints which are used in the MPC controller are listed in Table 5.1.

5.3.2 Simulation Results

The block diagram in Fig. 5.4 shows the Simulink design used for the simulation of the thermal management system for PCR-LOC microchip.

Table 5.1: The parameters of MPC Controller

Parameter	**Chosen Value or Range**
Heater temperature	$22°\text{C} \leq T_h \leq 190°\text{C}$
Chamber temperature	$22°\text{C} \leq T_{ch} \leq 96°\text{C}$
Heater current	$0 \leq I_h \leq 200\text{mA}$
Sampling time	$T_S = 0.1\text{s}$
Prediction horizon	25
Control horizon	6

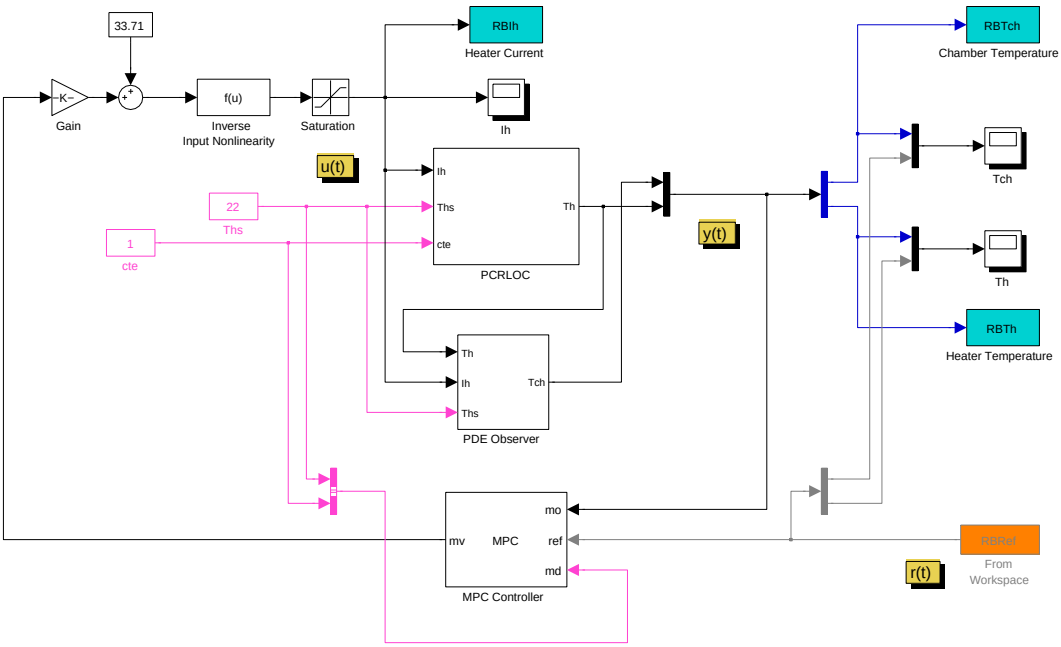

Figure 5.4: MPC control of PCR-LOC, Simulink model

The MPC controller is designed based on the lumped model calculated previously for this device. The PDE backstepping boundary observer is also used to calculate the chamber temperature which is required by MPC controller. The numerical calculation and the simulation of PDE backstepping boundary observer is discussed in detail in the chapter 4. Here, we only focus on MPC controller simulation and the effect of changing MPC weights in final control results.

The results of the MPC control is shown in Fig. 5.5. It is clear that the MPC supervisory control has used the control action on heater current to take the heater temperature close to its constraints so that the transient of chamber temperature speed up as much as possible. The MPC also presents excellent convergent results

for the chamber temperature.

The next simulation, depicted in Fig. 5.6, shows the effect of choosing different weights for plant outputs on MPC controller performance. In addition to affect control performance, it also affect the rendering of the design constraints.

In Fig. 5.6, we kept the chamber temperature weight at one and assigned the weights of 0.5, 0.1 and 0 to the heater temperature. As the weight for heater temperature decrease in comparison to the chamber temperature, the MPC controller performance in tracking the reference chamber temperature improves while the fulfilment of the constraints are no longer guaranteed. Therefore, it is very important to make a logical compromise in choosing the weights in the implementation phase.

5.4 Implementation Results

As explained in section 5.3, the heater and chamber temperatures are considered as measured outputs subject to proper constraint on them to prevent destroying the DNA sample. The chamber temperature is weighted 10 times more than the heater temperature.

The heater current is considered as a manipulated variable with the constraints on its maximum and minimum. The heatsink temperature is considered as a measured disturbance.

We selected a prediction horizon of 25 steps and a control horizon of 6 steps. The simulation of the designed MPC controller on the full PDE model reveals that the MPC controller can provide very good tracking performance as well as keeping the important variables within the required constraints.

Figure 5.7 illustrates interconnection of the MPC controller, the PDE observer and the hardware setup that is used for the implementation. In this block diagram, the interconnection between the MPC controller, the PDE Backstepping boundary observer, the supervisory thermal cycling generator and the hardware setup is illustrated. The design and the implementation of the MPC controller is performed using MPC Control Toolbox in MATLAB.

The next diagram shows the block diagram in Simulink which is used for the implementation of the thermal management system.

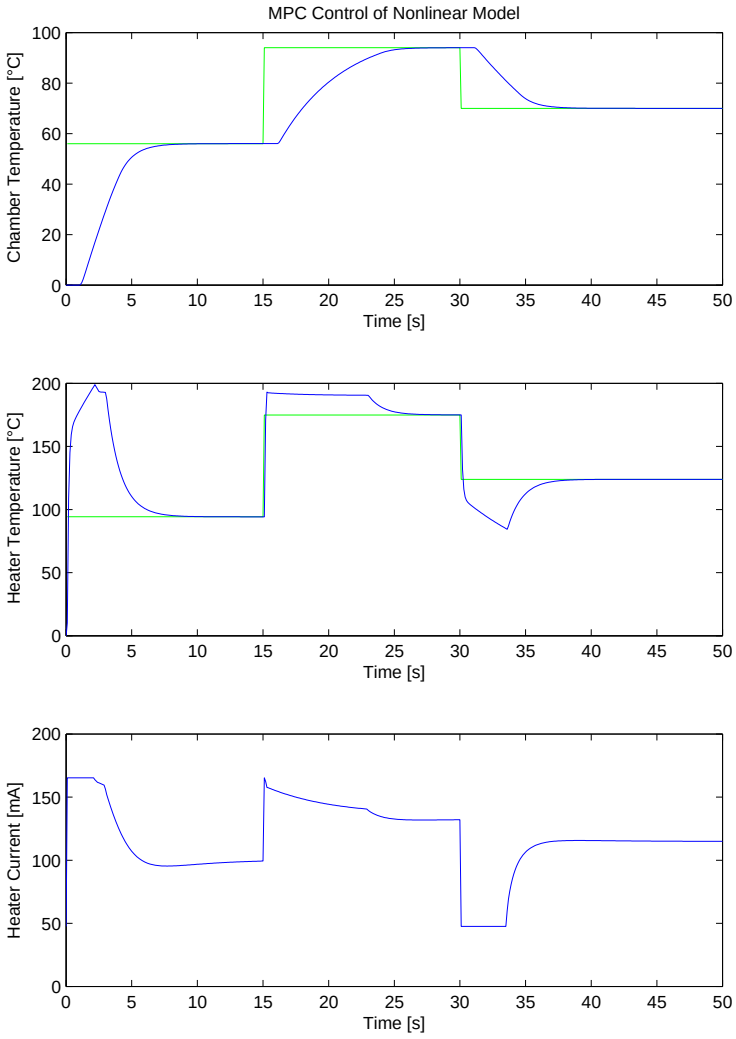

Figure 5.5: MPC control of PCR-LOC, simulation results

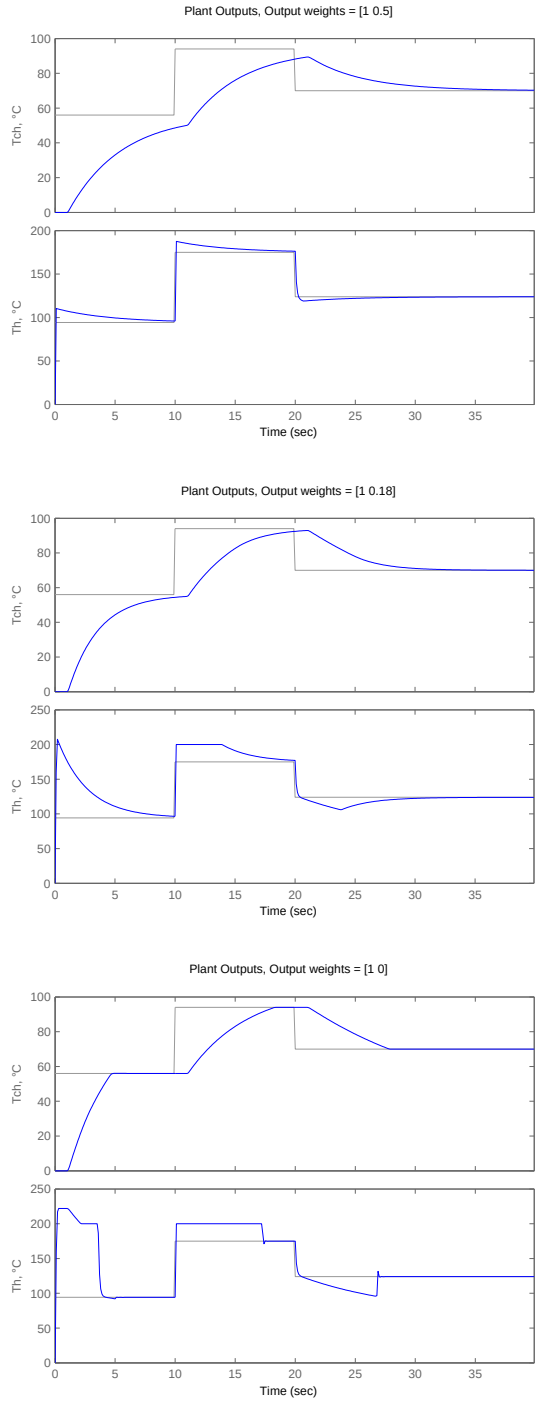

Figure 5.6: Effect of weights on MPC controllers performance

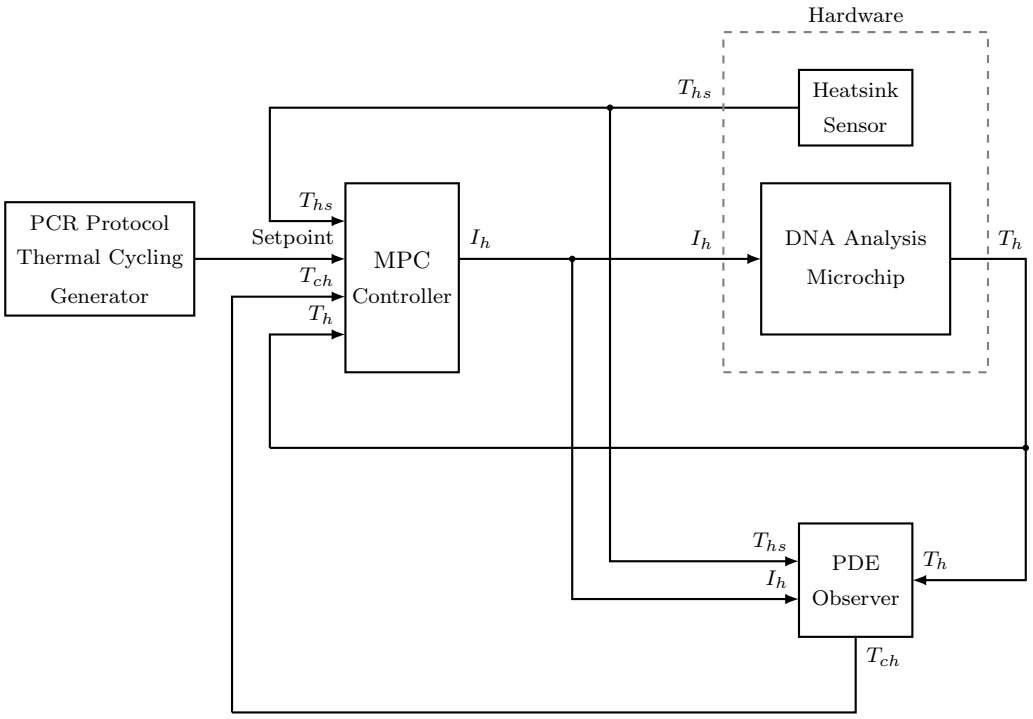

Figure 5.7: Advanced thermal management system for DNA analysis microchip

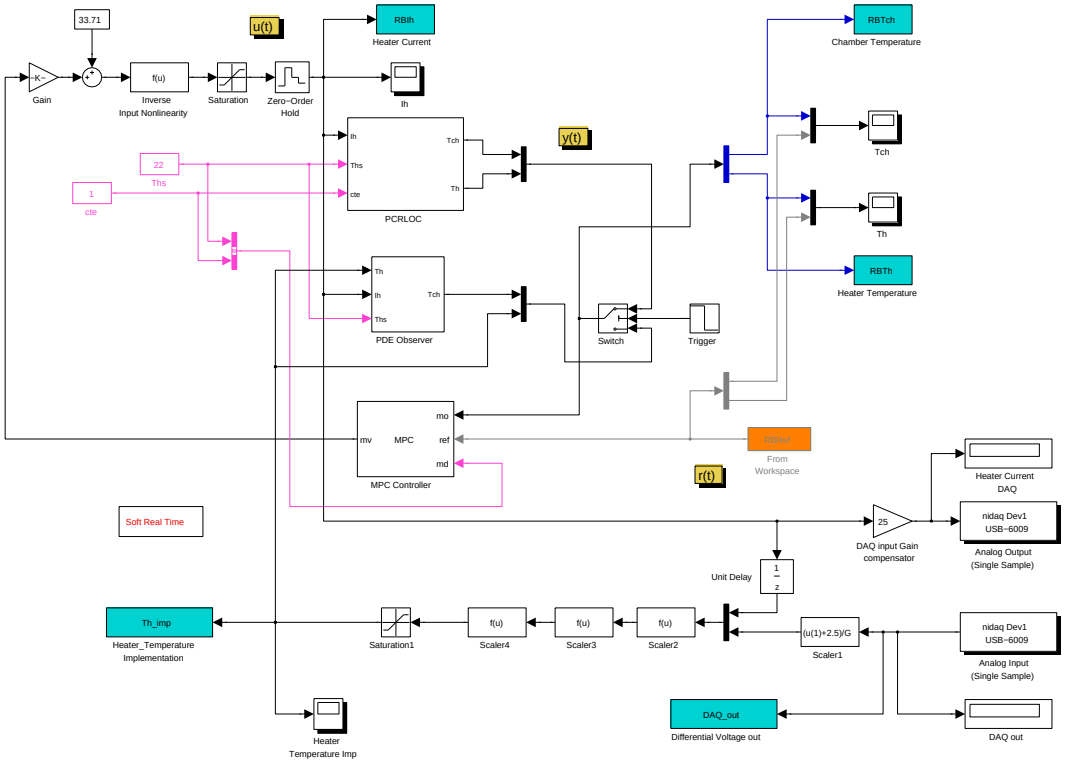

Figure 5.8: MPC control of PCRLOC, Simulink model for implementation

A switching mechanism is used in the implementation which allows the thermal management system controls the microchip in the open-loop mode for 40s before switching it to the closed-loop control mode. This technique is specially helpful in settling down the initial conditions and in preventing undesired control actions at the system start-up.

The results of the implementation are shown in Fig. 5.9.

5.5 Summary

In this chapter, detailed design of the interfacing circuit which is used to implement the PDE backstepping boundary observer is presented. The PDE backstepping boundary observer designed in chapter 3 was put in work with an MPC controller on the the PCR-LOC system.

The measurement of the heater temperature is estimated by the PDE backstepping boundary observer. The complete design is successfully implemented on the PCR-LOC device and the results are presented. The simulation and implementation results verifies the designed observer. The designed and tested setup including the microchip and the interfacing circuitry has the potential of being used as a laboratory setting to test and evaluate various control techniques on the PCR-LOC microchip.

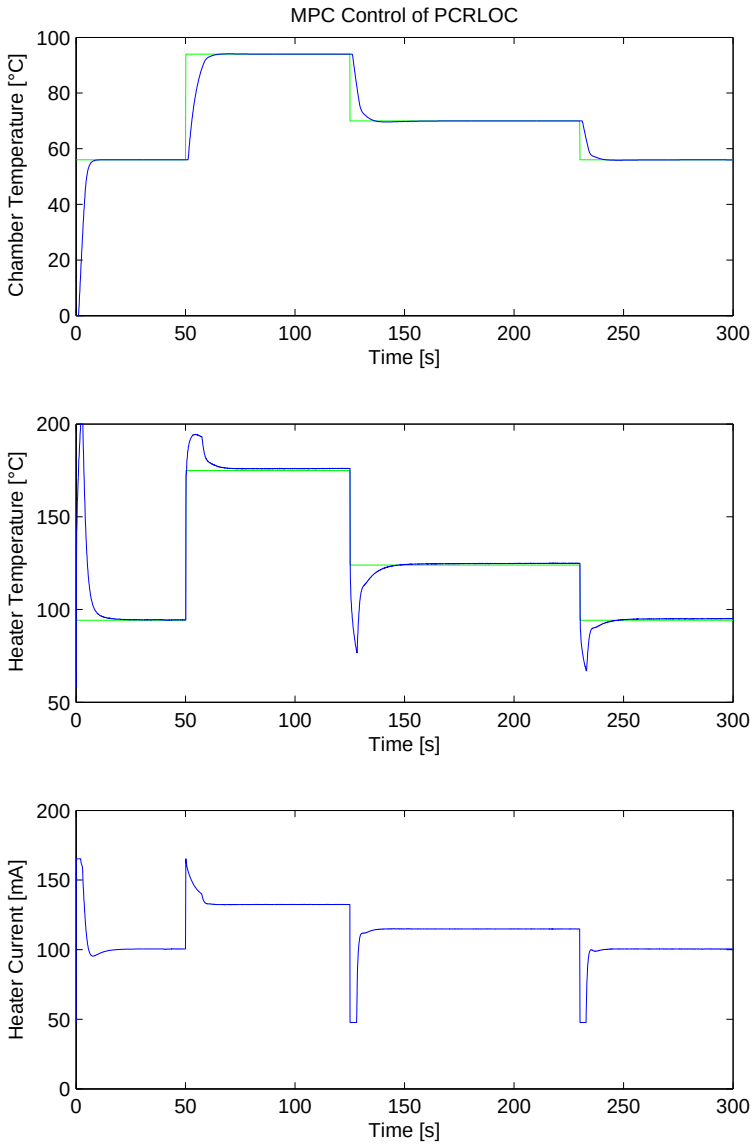

Figure 5.9: MPC implementation, tracking PCR temperatures

Chapter 6

Extension to Controller Design

6.1 Introduction

Controller design for distributed parameter system is a challenging problem. The early attempts to exploit the infinite dimensional characteristic of the PDE systems goes back to 1970's. In [104] a modal analysis was first applied to design controller for PDE systems. The problem of designing high performance controllers for systems with distributed parameter nature followed by works in the area of optimal control by Curtain and Zwart [34] and Bensoussan *et al.* [13], non-linear control by Orlov and Utkin [100] and Christofides [26], using backstepping approach by Krstić and Smyshlyaev [69], and Lyapunov methods by Orlov [99] and Coron *et al.* [29]. A review of the distributed parameter control literature can be found in [88].

Referring to work of Krstić and Smyshlyaev [69], this theory goes in parallel with the work on observer design presented in chapter 3. In this chapter, we provide the theoretical foundation for such extension.

The closed-loop interconnection of the PDE Backstepping boundary controller with the PDE system is illustrated in Fig. 6.1. Clearly, the PDE Backstepping boundary controller not only needs temperature information at the boundaries but also needs temperature information in all the points in the domain. The PDE Backstepping boundary observer designed in chapter 3 can provide these information.

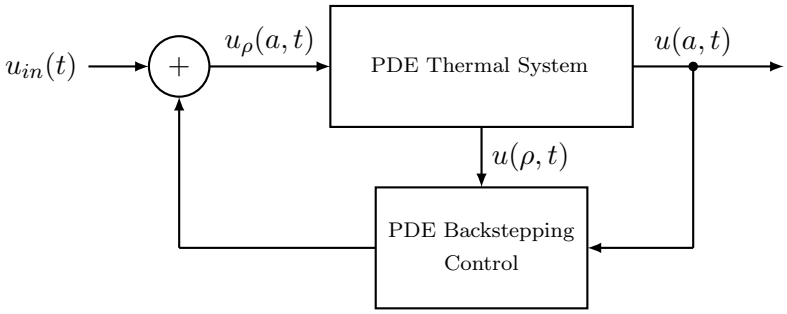

Figure 6.1: Interconnection of a closed-loop PDE system with PDE backstepping controller

6.2 PDE Backstepping Boundary Controller Design

We refer again to the normalized and transformed system that we used for observer design in Chapter 3. The normalized and transformed system in cylindrical coordinate system is given by:

$$u_t = u_{\rho\rho} + \frac{1}{\rho}u_\rho, \tag{6.1a}$$

where $a \leq \rho \leq 1$ and boundary conditions are as follows:

$$u(1) = 0 \tag{6.1b}$$

$$u_\rho(a) = \delta U \tag{6.1c}$$

$$u(a) = Measurement. \tag{6.1d}$$

We look for an integral transformation of the following form:

$$w(\rho) = u(\rho) - \int_1^\rho P(\rho,\zeta)u(\zeta)\zeta d\zeta, \tag{6.2}$$

along with feedback control

$$u_\rho(a) = aP(a,a)u(a) - \int_a^1 P_\rho(a,\zeta)\zeta u(\zeta)d\zeta, \tag{6.3}$$

that transforms (6.1) into the following exponentially stable target system with desired dynamics:

$$w_t = w_{\rho\rho} + \frac{1}{\rho}w_\rho - \lambda^2 w \tag{6.4a}$$

$$w(1) = 0 \tag{6.4b}$$

$$w_\rho(a) = 0. \tag{6.4c}$$

The function $P(\rho,\zeta)$ is the kernel of the integral equation proposed in (6.2). The parameter λ defines the observer convergence speed. The close loop system is illustrated in Fig. 6.1. We extend the standard PDE backstepping control design and obtain the following result:

Theorem 9. *Consider the PDE system defined by* (6.1) *in cylindrical coordinate system along with the integral transformation* (6.2) *and feedback control* (6.3) *that transform the closed-loop PDE system into* (6.4)*, where $P(\rho,\zeta)$ is the kernel of the integral transformation with $a \leq \rho \leq \zeta \leq 1$. The kernel function can be calculated by solving the following PDE equation:*

$$P_{\rho\rho}(\rho,\zeta)+\frac{1}{\rho}P_{\rho}(\rho,\zeta)+\lambda^2 P(\rho,\zeta)=P_{\zeta\zeta}(\rho,\zeta)+\frac{1}{\zeta}P_{\zeta}(\rho,\zeta), \tag{6.5a}$$

with the following boundary conditions:

$$P(\rho,\rho)=\frac{1}{2}\lambda^2\Big(\frac{1}{\rho}-1\Big) \tag{6.5b}$$

$$P(\rho,1)=0. \tag{6.5c}$$

$$\tag{6.5d}$$

Proof. We start by taking of time derivative of integral transformation (6.2) and substituting u_t with its description in (6.1a).

$$\begin{aligned} w_t &= u_t-\int_1^{\rho} P(\rho,\zeta)\Big(u_{\zeta\zeta}+\frac{1}{\zeta}u_{\zeta}\Big)\zeta d\zeta \\ &= u_{\rho\rho}+\frac{1}{\rho}u_{\rho} \\ &\quad -\int_1^{\rho} P(\rho,\zeta)\zeta u_{\zeta\zeta}d\zeta-\int_1^{\rho} P(\rho,\zeta)u_{\zeta}d\zeta. \end{aligned}$$

It follows that

$$\begin{aligned} \int_1^{\rho} P(\rho,\zeta)\zeta u_{\zeta\zeta}d\zeta =& \Big(\zeta P(\rho,\zeta)u_{\zeta}\Big|_1^{\rho}-\int_1^{\rho}\Big(P(\rho,\zeta)+\zeta P_{\zeta}(\rho,\zeta)\Big)u_{\zeta}d\zeta \\ =&\rho P(\rho,\rho)u_{\rho}(\rho)-P(\rho,1)u_{\rho}(1)-\int_1^{\rho} P(\rho,\zeta)u_{\zeta}d\zeta \\ &-\Big(\zeta P_{\zeta}(\rho,\zeta)u\Big|_1^{\rho}+\int_1^{\rho}\Big(P_{\zeta}(\rho,\zeta)+\zeta P_{\zeta\zeta}(\rho,\zeta)\Big)ud\zeta \\ =&\rho P(\rho,\rho)u_{\rho}(\rho)-P(\rho,1)u_{\rho}(1)-\int_1^{\rho} P(\rho,\zeta)u_{\zeta}d\zeta \\ &-\rho P_{\zeta}(\rho,\rho)u(\rho)+P_{\zeta}(\rho,1)u(1) \\ &+\int_1^{\rho}\Big(P_{\zeta}(\rho,\zeta)+\zeta P_{\zeta\zeta}(\rho,\zeta)\Big)ud\zeta. \end{aligned}$$

Using (6.1b), we arrive to the following equation for w_t,

$$\begin{aligned} w_t =& u_{\rho\rho} + \frac{1}{\rho}u_\rho \\ & - \rho P(\rho,\rho)u_\rho(\rho) + P(\rho,1)u_\rho(1) \\ & + \rho P_\zeta(\rho,\rho)u(\rho) \\ & - \int_1^\rho \Big(P_\zeta(\rho,\zeta) + \zeta P_{\zeta\zeta}(\rho,\zeta)\Big)u d\zeta, \end{aligned} \tag{6.6}$$

For calculation of w_ρ, we take derivative of the both sides of (6.2).

$$\begin{aligned} w_\rho(\rho) &= u_\rho(\rho) - \frac{d}{d\rho}\int_1^\rho P(\rho,\zeta)u(\zeta)\zeta d\zeta \\ &= u_\rho(\rho) - \rho P(\rho,\rho)u(\rho) - \int_1^\rho P_\rho(\rho,\zeta)\zeta u(\zeta)d\zeta. \end{aligned} \tag{6.7}$$

We can use (6.7) and (6.4c) to find the value of $u_\rho(\rho)$ at $\rho = a$

$$\begin{aligned} u_\rho(a) &= w_\rho(a) + aP(a,a)u(a) + \int_1^a P_\rho(a,\zeta)\zeta u(\zeta)d\zeta \\ &= aP(a,a)u(a) - \int_a^1 P_\rho(a,\zeta)\zeta u(\zeta)d\zeta. \end{aligned} \tag{6.8}$$

The next step is the calculation of $w_{\rho\rho}$. To find $w_{\rho\rho}$, we take derivative of (6.7):

$$\begin{aligned} w_{\rho\rho}(\rho) =& u_{\rho\rho}(\rho) - \frac{d}{d\rho}\Big(\rho P(\rho,\rho)u(\rho)\Big) - \frac{d}{d\rho}\int_1^\rho P_\rho(\rho,\zeta)\zeta u(\zeta)d\zeta \\ =& u_{\rho\rho}(\rho) - P(\rho,\rho)u(\rho) - \rho P(\rho,\rho)u_\rho(\rho) \\ & - \rho u(\rho)\frac{d}{d\rho}P(\rho,\rho) - \rho P_\rho(\rho,\rho)u(\rho) \\ & - \int_1^\rho P_{\rho\rho}(\rho,\zeta)\zeta u(\zeta)d\zeta. \end{aligned} \tag{6.9}$$

Now by substituting the equation for w_t, w_ρ and $w_{\rho\rho}$ which are calculated in (6.6), (6.7) and (6.9) in (6.4a), the equation (6.4a) becomes:

$$\begin{aligned} & u_{\rho\rho} + \frac{1}{\rho}u_\rho - \rho P(\rho,\rho)u_\rho(\rho) + P(\rho,1)u_\rho(1) + \rho P_\zeta(\rho,\rho)u(\rho) \\ & \quad - \int_1^\rho \Big(P_\zeta(\rho,\zeta) + \zeta P_{\zeta\zeta}(\rho,\zeta)\Big)u d\zeta \\ =& u_{\rho\rho} - P(\rho,\rho)u(\rho) - \rho P(\rho,\rho)u_\rho(\rho) - \rho u(\rho)\frac{d}{d\rho}P(\rho,\rho) - \rho P_\rho(\rho,\rho)u(\rho) \\ & \quad - \int_1^\rho P_{\rho\rho}(\rho,\zeta)\zeta u(\zeta)d\zeta \\ & \quad + \frac{1}{\rho}u_\rho - P(\rho,\rho)u(\rho) - \int_1^\rho \frac{1}{\rho}P_\rho(\rho,\zeta)\zeta u(\zeta)d\zeta \\ & \quad - \lambda^2 u(\rho) + \int_1^\rho \lambda^2 P(\rho,\zeta)u(\zeta)\zeta d\zeta. \end{aligned} \tag{6.10}$$

Rearranging (6.10) we arrive to the following equation:

$$\begin{aligned} &P(\rho,1)u_\rho(1)+\Big(2P(\rho,\rho)+2\rho\frac{d}{d\rho}P(\rho,\rho)+\lambda^2\Big)u(\rho)\\ &+\int_1^\rho\Big(P_{\rho\rho}(\rho,\zeta)+\frac{1}{\rho}P_\rho(\rho,\zeta)-\lambda^2P(\rho,\zeta)-P_{\zeta\zeta}(\rho,\zeta)-\frac{1}{\zeta}P_\zeta(\rho,\zeta)\Big)\zeta u d\zeta \qquad (6.11)\\ =&0. \end{aligned}$$

From the equation 6.11 it would appear that the kernel function $P(\rho,\zeta)$ has to satisfy the following PDE

$$\begin{aligned} P_{\rho\rho}(\rho,\zeta)+\frac{1}{\rho}P_\rho(\rho,\zeta)-\lambda^2P(\rho,\zeta)&=P_{\zeta\zeta}(\rho,\zeta)+\frac{1}{\zeta}P_\zeta(\rho,\zeta)\\ \rho\frac{d}{d\rho}P(\rho,\rho)+P(\rho,\rho)&=-\frac{1}{2}\lambda^2 \qquad (6.12)\\ P(\rho,1)&=0. \end{aligned}$$

The first boundary condition introduced in (6.12) can be written as follows:

$$\frac{d}{d\rho}(\rho P(\rho,\rho))=-\frac{1}{2}\lambda^2. \qquad (6.13)$$

It is easy to see that the solution of (6.13) has a solution as follow:

$$P(\rho,\rho)=\frac{c}{\rho}-\frac{1}{2}\lambda^2\,, \qquad (6.14)$$

where c is a constant to be defined. The constant value in (6.14) can be defined by substituting $\rho=1$ in the last boundary condition in (6.12):

$$P(1,1)=0. \qquad (6.15)$$

By using (6.15) in (6.14), we find the constant c,

$$c=\frac{1}{2}\lambda^2. \qquad (6.16)$$

Combining (6.12), (6.14) and (6.16), the PDE equation that describes the kernel function $P(\rho,\zeta)$ is obtain as follows:

$$P_{\rho\rho}(\rho,\zeta)+\frac{1}{\rho}P_\rho(\rho,\zeta)+\lambda^2P(\rho,\zeta)=P_{\zeta\zeta}(\rho,\zeta)+\frac{1}{\zeta}P_\zeta(\rho,\zeta),$$

with following boundary conditions:

$$\begin{aligned} P(\rho,\rho)&=\frac{1}{2}\lambda^2\Big(\frac{1}{\rho}-1\Big)\\ P(\rho,1)&=0. \end{aligned}$$

The domain for kernel function $P(\rho, \zeta)$ is described by

$$a \leq \rho \leq 1$$

$$\rho \leq \zeta \leq 1.$$

Equations (6.3) and (6.5b) define the feedback control law as follow:

$$u_\rho(a) = \frac{1}{2}\lambda^2(1-a)u(a) - \int_a^1 P_\rho(a,\zeta)\zeta u(\zeta)d\zeta, \tag{6.17}$$

□

The domain of the PDE equation describing the integral kernel function is depicted in Fig. 6.2. Boundary conditions are shown at each boundary.

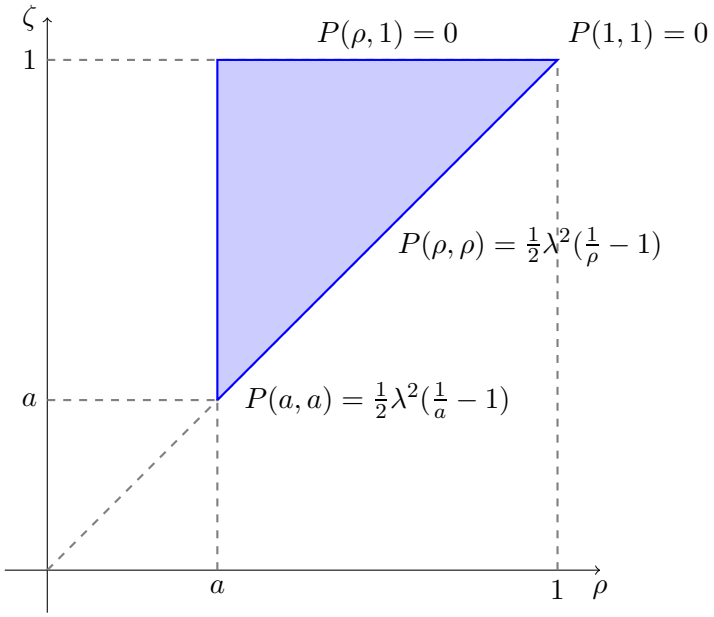

Figure 6.2: Domain of the controller kernel function, $P(\rho, \zeta)$

To complete the design we need to fully define the feedback control, given in (6.3). For that, however, we need the kernel function $P(\rho, \zeta)$ which requires solving the PDE equation (6.5a). Since we do not have an analytical solution, we proceed with a numerical approach similar to the one that we used for numerical calculation of the observer kernel.

6.2.1 Stability of the Closed-Loop System

In previous section, we designed a PDE Backstepping boundary controller based on an integral transformation that transforms the original system to an exponentially

stable target system. To show that the stability of the target system (6.4) implies the stability of the closed-loop plant (6.1) with feedback control (6.17), we need to show that the transformation (6.2) is invertible. We write an inverse transformation as follows:

$$u(\rho) = w(\rho) - \int_1^\rho K(\rho,\zeta)w(\zeta)\zeta d\zeta, \tag{6.18}$$

where $K(\rho,\zeta)$ is the transformation kernel.

Theorem 10. *Given the direct transformation* (6.2) *and the inverse transformation* (6.18)*, the integral kernels* $P(\rho,\zeta)$ *and* $K(\rho,\zeta)$ *satisfy*

$$K(\rho,\zeta) = -P(\rho,\zeta) - \int_\rho^\zeta P(\rho,\gamma)K(\gamma,\zeta)\gamma d\gamma, \tag{6.19}$$

Proof. Substituting (6.18) in (6.2), we get

$$\begin{aligned} w(\rho) =& w(\rho) - \int_1^\rho K(\rho,\zeta)w(\zeta)\zeta d\zeta \\ &- \int_1^\rho P(\rho,\zeta)\Big[w(\zeta) - \int_1^\zeta K(\zeta,\gamma)w(\gamma)\gamma d\gamma\Big]\zeta d\zeta \\ =& w(\rho) - \int_1^\rho K(\rho,\zeta)w(\zeta)\zeta d\zeta \\ &- \int_1^\rho P(\rho,\zeta)w(\zeta)\zeta d\zeta + \int_1^\rho \int_1^\zeta P(\rho,\zeta)K(\zeta,\gamma)w(\gamma)\gamma\zeta d\gamma d\zeta \end{aligned} \tag{6.20}$$

Recalling the following formula for changing the order of integration:

$$\int_1^\rho \int_1^\zeta f(\rho,\zeta,\gamma)d\gamma d\zeta = \int_1^\rho \int_\gamma^\rho f(\rho,\zeta,\gamma)d\zeta d\gamma \tag{6.21}$$

Using (6.21) in (6.20), we arrive to:

$$\int_1^\rho K(\rho,\zeta)w(\zeta)\zeta d\zeta + \int_1^\rho P(\rho,\zeta)w(\zeta)\zeta d\zeta - \int_1^\rho \int_\gamma^\rho P(\rho,\zeta)K(\zeta,\gamma)w(\gamma)\gamma\zeta d\zeta d\gamma = 0,$$

which can be written as

$$\int_1^\rho \zeta w(\zeta)\Big[K(\rho,\zeta) + P(\rho,\zeta) - \int_\zeta^\rho P(\rho,\gamma)K(\gamma,\zeta)\gamma d\gamma\Big]d\zeta. \tag{6.22}$$

Since (6.22) has to hold for all $w(\zeta)$, we have

$$K(\rho,\zeta) = -P(\rho,\zeta) - \int_\rho^\zeta P(\rho,\gamma)K(\gamma,\zeta)\gamma d\gamma. \tag{6.23}$$

□

Calculation of the inverse transformation kernel $K(\rho,\zeta)$ follows the same steps that are use in calculation of the kernel $P(\rho,\zeta)$. Exponential stability of the target system (6.4) and invertability of the transformation (6.2) imply exponential stability of the closed-loop system [111].

6.3 Analysis and Discussion

In this chapter, we design a boundary controller capable of changing the dynamics of the PDE system (6.1).

Backstepping design is a valid approach but in this case the results of this approach lead to very aggressive control actions due to controllers attempt to speed up the distributed parameter systems dynamics. The PDE backstepping approach is primary powerful in stabilization and it is not a suitable controller for our case due to the number of constraint involved in thermal control problem of the PCR-LOC microchip. A proper approach in this case should be able to directly incorporate input constraints.

The design work-flow presented in this chapter can be used as a guide line in PDE backstepping boundary control design in cylindrical coordinate system. The class of PDE systems defined in cylindrical coordinate system are mostly connected to the systems that feature circular symmetry in their structural design.

Chapter 7

Summary and Future Work

In this project, we had the unique opportunity to adopt, develop and implement distributed parameter system's control results on an important application in medical devices. An important future of this project was the successful implementation of a PDE backstepping boundary observer in a real world application. A quick look at the literature on the distributed parameter systems analysis and control reveals that the available results hardly get to the simulations step let alone the implementation.

We tackled the observer design problem by resorting the use of a conformal transformation that converted the original two-dimensional problem into an equivalent problem in one-dimension for which a solution is calculated. Our approach is novel and can be extended to many classes of the PDE systems with different application.

The advanced thermal management system, including the PDE backstepping boundary observer and a MPC controller were implemented through Simulink DAQ toolbox and an interfacing circuit. The control loop designed to execute the experiment under an update rate of 0.1 second.

7.1 Directions for Future Works

The results of this thesis can be generalized and extended to many applications. The important directions for future work would be as follows:

- Extension to non-harmonic functions

  Harmonic functions, i.e. solutions of Laplace's equation, has been the central point of interest in conformal mapping. Bazant in [11] noted that there are some other equations that are also conformally invariant. For example, steady-states of various nonlinear diffusion equations, the advection-diffusion equations for potential flows and Nernst-Plank equations for bulk electrochemical transport. The extension of our results to non-harmonic functions can open doors for various applications.

- Integration with distributed MPC

  A framework for MPC control of distributed parameter systems is recently developed by Dubljevic. MPC control considered for parabolic PDEs with boundary actuation [39] and state and actuation constraints [40, 38]. These results need that the measurement of the PDE states be available. The PDE backstepping boundary observer can provide an estimation of the spatially distributed PDE states

- Extension to new applications

  A very nice extension of this work could be its application in controlling and optimizing the efficiency of industrial burners. In [115] it was shown that conformal mapping has potential application in analysis and active control of flame formation. Employing our method in PDE backstepping boundary observer design has the potential of pushing the current technology for industrial burners one step forward.

Appendix A

Interfacing Circuit Schematic & PCB

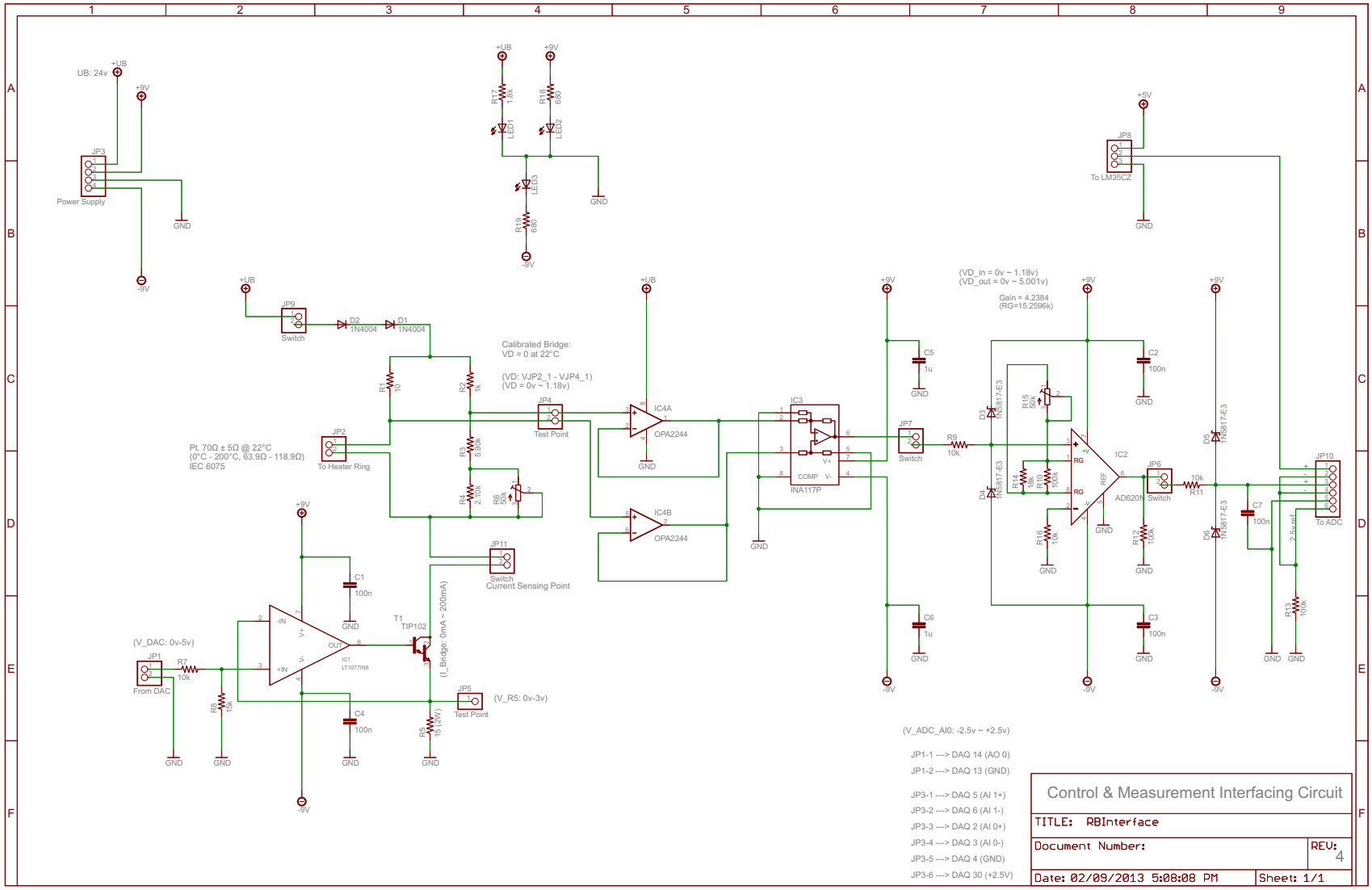

Figure A.1: Interfacing circuit schematic

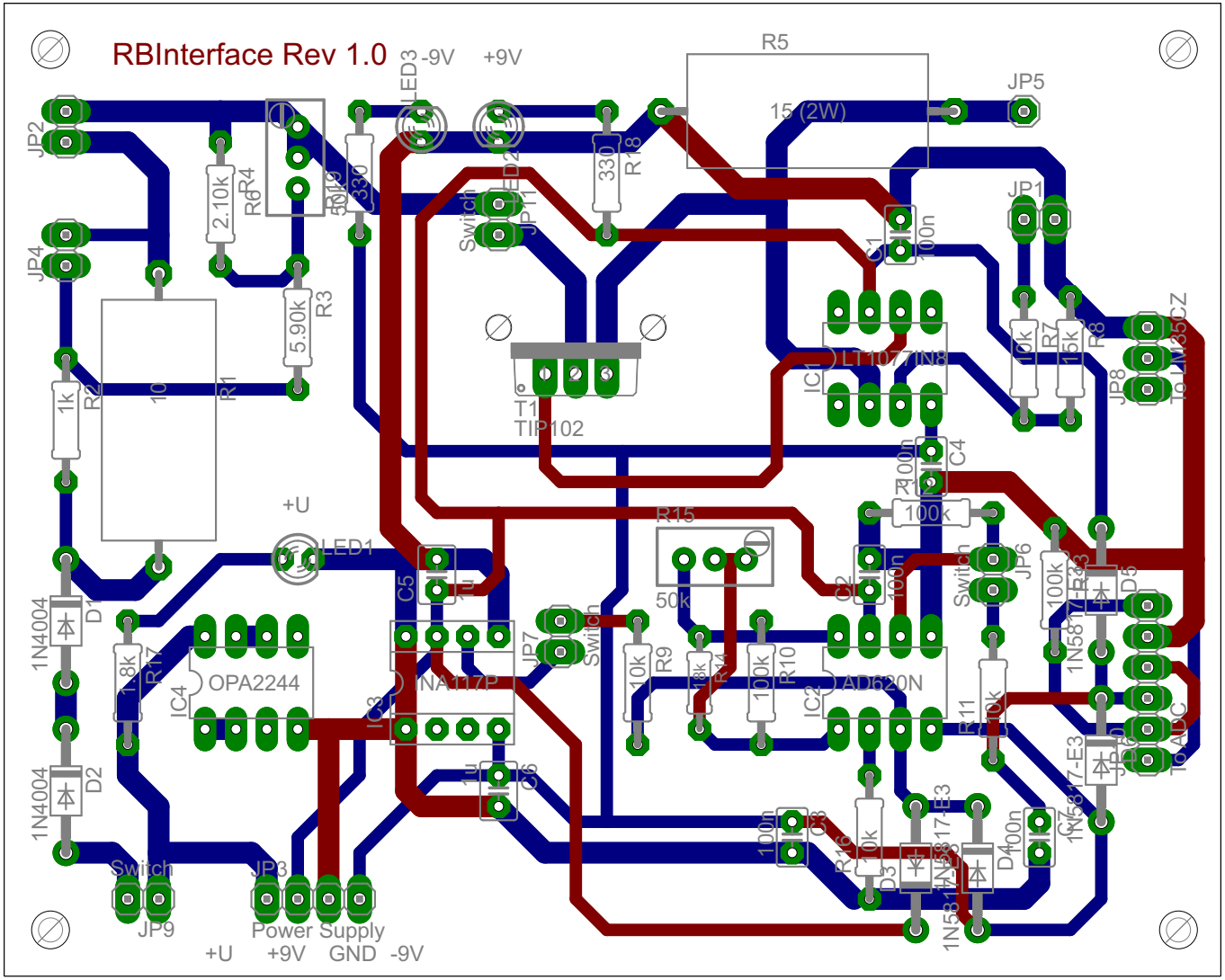

Figure A.2: Interfacing circuit printed circuit board

Bibliography

[1] M. Abramowitz and I. Stegun. *Handbook of Mathematical Functions: With Formulas, Graphs, and Mathematical Tables*. Dover Publications, 1965.

[2] L. Ahlfors. *Complex analysis: an introduction to the theory of analytic functions of one complex variable*. International series in pure and applied mathematics. McGraw-Hill, 1979.

[3] M. Athans. Toward a practical theory for distributed parameter systems. *IEEE Transactions on Automatic Control*, 15(2):245–247, 1970.

[4] G. Avalos and I. Lasiecka. Differential riccati equation for the active control of a problem in structural acoustics. *Journal of Optimization Theory and Applications*, 91(3):695–728, 1996.

[5] T. Bailey and J. E. Hubbard. Distributed piezoelectric-polymer active vibration control of a cantilever beam. *Journal of Guidance, Control, and Dynamics*, 8(5), 2012.

[6] M. Balas. Active control of flexible systems. *Journal of Optimization Theory and Applications*, 25(3):415 – 436, 1978.

[7] M. J. Balas. Feedback control of linear diffusion processes. *International Journal of Control*, 29(3):523 – 533, 1979.

[8] A. Balogh and M. Krstić. Infinite dimensional backstepping-style feedback transformations for a heat equation with an arbitrary level of instability. *European Journal of Control*, 8(2):165–175, 2002.

[9] A. Balogh and M. Krstić. Infinite dimensional backstepping for nonlinear parabolic PDEs. *Unsolved problems in mathematical systems and control theory*, page 153, 2004.

[10] A. Balogh and M. Krstić. Stability of partial difference equations governing control gains in infinite-dimensional backstepping. *Systems & Control Letters*, 51(2):151–164, 2004.

[11] M. Z. Bazant. Conformal mapping of some non-harmonic functions in transport theory. *Proceedings: Mathematical, Physical and Engineering Sciences*, 460(2045):pp. 1433–1452, 2004.

[12] N. Bekiaris-Liberis, M. Jankovic, and M. Krstic. Adaptive stabilization of lti systems with distributed input delay. *International Journal of Adaptive Control and Signal Processing*, 27(1-2):46–65, 2013.

[13] A. Bensoussan, M. Delfour, G. Da Prato, and S. Mitter. *Representation and control of infinite dimensional systems*. Birkhauser, 1992.

[14] D. Bošković, A. Balogh, and M. Krstić. Backstepping in infinite dimension for a class of parabolic distributed parameter systems. *Mathematics of Control, Signals, and Systems (MCSS)*, 16(1):44–75, 2003.

[15] D. Bošković and M. Krstić. Backstepping control of chemical tubular reactors. *Computers and Chemical Engineering*, 26(7-8):1077–1085, 2002.

[16] D. M. Bošković and M. Krstić. Nonlinear stabilization of a thermal convection loop by state feedback. *Automatica*, 37(12):2033 – 2040, 2001. Boundary control;.

[17] D. M. Bošković and M. Krstić. Stabilization of a solid propellant rocket instability by state feedback. *International Journal of Robust and Nonlinear Control*, 13(5):483 – 495, 2003. Backstepping design;.

[18] J. Brown and R. Churchill. *Complex variables and applications*. Churchill-Brown series. McGraw-Hill Higher Education, seventh edition, 2004.

[19] J. Brown and R. Churchill. *Fourier series and boundary value problems*. McGraw-Hill, 7th edition, 2008.

[20] M. Burns, B. Johnson, S. Brahmasandra, K. Handique, J. Webster, M. Krishnan, T. Sammarco, P. Man, D. Jones, D. Heldsinger, et al. An Integrated Nanoliter DNA Analysis Device. *Science*, 282(5388):484, 1998.

[21] A. G. Butkovskii. *Distributed Control Systems*. Elsevier Science Ltd, 1969.

[22] E. F. Camacho, C. Bordons, E. F. Camacho, and C. Bordons. *Model predictive control*. Springer London, 2nd edition, 2004.

[23] A. Chaudhari, T. Woudenberg, M. Albin, and K. Goodson. Transient liquid crystal thermometry of microfabricated PCR vessel arrays. *Journal of Microelectromechanical Systems*, 7(4):345–355, 1998.

[24] M. Cheng, V. Radisavljevic, and W. Su. Output-feedback boundary control of an uncertain heat equation with noncollocated observation: A sliding-mode approach. In *the 5th IEEE Conference on Industrial Electronics and Applications (ICIEA)*, pages 2187–2192. IEEE, 2010.

[25] H. Choi, P. Moin, and J. Kim. Active turbulence control for drag reduction in wall-bounded flows. *Journal of Fluid Mechanics*, 262:75–75, 1994.

[26] P. D. Christofides. *Nonlinear and robust control of PDE systems, methods and applications to transport-reaction processes*. Birkhauser, 2001.

[27] O. Cifdaloz, A. A. Rodriguez, and J. M. Anderies. Control of distributed parameter systems subject to convex constraints: Applications to irrigation systems and hypersonic vehicles. In *the 47th IEEE Conference on Decision and Control (CDC)*, pages 865–870. IEEE, 2008.

[28] D. Colton. The solution of initial-boundary value problems for parabolic equations by the method of integral operators. *Journal of Differential Equations*, 26:181–190, 1977.

[29] J.-M. Coron, B. d'Andrea Novel, and G. Bastin. A strict lyapunov function for boundary control of hyperbolic systems of conservation laws. *IEEE Transac-*

tions on Automatic Control, 52(1):2 – 11, 2007. Boundary control;Hyperbolic systems;Conservation laws;Riemann invariants;.

[30] R. Curtain. Finite-dimensional compensator design for parabolic distributed systems with point sensors and boundary input. *IEEE Transactions on Automatic Control*, 27(1):98–104, 1982.

[31] R. Curtain, M. Demetriou, and K. Ito. Adaptive observers for structurally perturbed infinite dimensional systems. In *Proceedings of the 36th IEEE Conference on Decision and Control (CDC)*, volume 1, pages 509–514. IEEE, 1997.

[32] R. Curtain, M. Demetriou, and K. Ito. Adaptive observers for slowly time varying infinite dimensional systems. In *Proceedings of the 37th IEEE Conference on Decision and Control (CDC)*, volume 4, pages 4022–4027. IEEE, 1998.

[33] R. Curtain, M. Demetriou, and K. Ito. Adaptive compensators for perturbed positive real infinite-dimensional systems. *International Journal of Applied Mathematics and Computer Science*, 13(4):441–452, 2003.

[34] R. Curtain and H. Zwart. *An introduction to infinite-dimensional linear systems theory*. Springer, 1995.

[35] M. Demetriou and K. Ito. Adaptive observers for a class of infinite dimensional systems. In *Proc. 13th World Congress, IFAC, San Francisco, CA*, pages 409–413, 1996.

[36] T. Driscoll. Schwarz-Christoffel Toolbox User's Guide: Version 2.3. *Department of Mathematical Sciences, Ewing Hall, University of Delaware, Newark, DE*, 19716, 2005.

[37] T. Driscoll and L. Trefethen. *Schwarz-Christoffel Mapping*, volume 8 of *Cambridge Monographs on Applied and Computational Mathematics*. Cambridge University Press, Cambridge, UK, 2002.

[38] S. Dubljevic. Model predictive control of Kuramoto–Sivashinsky equation with state and input constraints. *Chemical Engineering Science*, 65(15):4388–4396, 2010.

[39] S. Dubljevic and P. Christofides. Predictive control of parabolic PDEs with boundary control actuation. *Chemical engineering science*, 61(18):6239–6248, 2006.

[40] S. Dubljevic, N. H. El-Farra, P. Mhaskar, and P. D. Christofides. Predictive control of parabolic PDEs with state and control constraints. *International Journal of robust and nonlinear control*, 16(16):749–772, 2006.

[41] A. El Jai and M. Amouroux. Sensors and observers in distributed parameter systems. *International Journal of Control*, 47(1):333–347, 1988.

[42] A. Fursikov. *Optimal Control of Distributed Systems: Theory and Applications*. American Mathematical Society, 2000.

[43] D. Gaitonde and M. Visbal. High-order schemes for navier-stokes equations: algorithm and implementation into fdl3di. Technical Report AFRL-VA-WP-TR-1998-3060, Air Force Research Laboratory, Wright-Patterson Air Force Base, Ohio, 1998.

[44] C. Gerald and P. Wheatley. *Applied numerical analysis*. Addison-Wesley World Student Series. Addison-Wesley Pub. Co., 1989.

[45] B. Giordano, J. Ferrance, S. Swedberg, A. Hühmer, and J. Landers. Polymerase Chain Reaction in Polymeric Microchips: DNA Amplification in Less Than 240 Seconds. *Analytical Biochemistry*, 291(1):124–132, 2001.

[46] R. Gressang and G. Lamont. Observers for systems characterized by semigroups. *IEEE Transactions on Automatic Control*, 20(4):523–528, 1975.

[47] A. Griffiths, S. Wessler, R. Lewontin, and S. Carroll. *Introduction to Genetic Analysis*. W. H. Freeman, 2008.

[48] J. Hathout, A. Annaswamy, M. Fleifil, and A. Ghoniem. A model-based active control design for thermoacoustic instability. *Combustion science and technology*, 132(1-6):99–138, 1998.

[49] J. Hay and D. Hollingsworth. Calibration of micro-encapsulated liquid crystals using hue angle and a dimensionless temperature. *Experimental thermal and fluid science*, 18(3):251–257, 1998.

[50] J.-W. He, R. Glowinski, R. Metcalfe, A. Nordlander, and J. Periaux. Active control and drag optimization for flow past a circular cylinder: I. oscillatory cylinder rotation. *Journal of Computational Physics*, 163(1):83–117, 2000.

[51] V. N. Hoang. Thermal management strategies for microfluidic devices. Master's thesis, University of Alberta, 2008.

[52] P. Huerre and P. A. Monkewitz. Local and global instabilities in spatially developing flows. *Annual Review of Fluid Mechanics*, 22(1):473–537, 1990.

[53] A. Iles, R. Fortt, and A. de Mello. Thermal optimisation of the Reimer–Tiemann reaction using thermochromic liquid crystals on a microfluidic reactor. *Lab on a Chip*, 5(5):540–544, 2005.

[54] M. Imran and A. Bhattacharyya. Thermal response of an on-chip assembly of RTD heaters, sputtered sample and microthermocouples. *Sensors and Actuators A: Physical*, 121(2):306–320, 2005.

[55] A. Jelfreys, V. Wilson, and S. Thein. Individual-specific fingerprints of human DNA. *Nature*, 316:4, 1985.

[56] J. Jiang, G. Kaigala, H. Marquez, and C. Backhouse. Nonlinear controller designs for thermal management in pcr amplification. *IEEE Transactions on Control Systems Technology*, (99):1–20, 2012.

[57] G. Kaigala. *Genetic Analysis Using Lab-on-a-Chip Technologies*. PhD thesis, University of Alberta, 2009.

[58] G. Kaigala, M. Behnam, A. Bidulock, C. Bargen, R. Johnstone, D. Elliott, and C. Backhouse. A scalable and modular lab-on-a-chip genetic analysis instrument. *The Analyst*, 135:1606–1617, 2010.

[59] G. Kaigala, M. Behnam, C. Bliss, M. Khorasani, S. Ho, J. McMullin, D. Elliott, and C. Backhouse. Inexpensive, universal serial bus-powered and fully portable

lab-on-a-chip-based capillary electrophoresis instrument. *IET, Nanobiotechnology*, 3(1):1–7, 2009.

[60] G. Kaigala, V. Hoang, A. Stickel, J. Lauzon, D. Manage, L. Pilarski, and C. Backhouse. An inexpensive and portable microchip-based platform for integrated RT–PCR and capillary electrophoresis. *The Analyst*, 133(3):331–338, 2008.

[61] G. Kaigala, R. Huskins, J. Preiksaitis, X. Pang, L. Pilarski, and C. Backhouse. Automated screening using microfluidic chip-based PCR and product detection to assess risk of BK virus-associated nephropathy in renal transplant recipients. *Electrophoresis*, 27(19):3753–3763, 2006.

[62] R. B. Khosroushahi and H. J. Marquez. Stable finite difference calculations in backstepping boundary controller design problems. *FEGRS2011*, 2011.

[63] S. Kitamura, H. Sakairi, and M. Nishimura. Observers for distributed parameter diffusion systems. *Electr. Engng Jap.*, 92:142149, 1972.

[64] G. Kreisselmeier. The generation of adaptive law structures for globally convergent adaptive observers. *IEEE Transactions on Automatic Control*, 24(3):510–513, 1979.

[65] A. J. Krener and W. Kang. Locally convergent nonlinear observers. *SIAM Journal on Control and Optimization*, 42:155, 2003.

[66] M. Krstic. *Delay compensation for nonlinear, adaptive, and PDE systems*. Birkhauser Boston, MA, 2009.

[67] M. Krstic and N. Bekiaris-Liberis. Control of nonlinear delay systems: A tutorial. In *the 51st IEEE Conference on Decision and Control (CDC)*, pages 5200–5214. IEEE, 2012.

[68] M. Krstic, A. A. Siranosian, A. Balogh, and B.-Z. Guo. Control of strings and flexible beams by backstepping boundary control. In *American Control Conference, 2007. ACC'07*, pages 882–887. IEEE, 2007.

[69] M. Krstić and A. Smyshlyaev. *Boundary control of PDEs: A course on backstepping designs*. Society for Industrial Mathematics, 2008.

[70] W. Kwok, R. Moser, and J. Jiménez. A critical evaluation of the resolution properties of b-spline and compact finite difference methods. *Journal of Computational Physics*, 174(2):510–551, 2001.

[71] P. K. Kythe. *Computational conformal mapping*. Birkhauser Boston, 1998.

[72] E. Lagally, J. Scherer, R. Blazej, N. Toriello, B. Diep, M. Ramchandani, G. Sensabaugh, L. Riley, and R. Mathies. Integrated portable genetic analysis microsystem for pathogen/infectious disease detection. *Analytical Chemistry*, 76(11):3162–3170, 2004.

[73] E. Lagally and H. Soh. Integrated genetic analysis microsystems. *Critical Reviews in Solid State and Materials Sciences*, 30(4):207–233, 2005.

[74] I. Lasiecka. *Mathematical control theory of coupled PDEs*. Society for Industrial & Applied Mathematics, 2002.

[75] I. Lasiecka and R. Triggiani. *Control theory for partial differential equations: continuous and approximation theories*. Cambridge University Press, 2000.

[76] S. Lele. Compact finite difference schemes with spectral-like resolution. *Journal of Computational Physics*, 103(1):16–42, 1992.

[77] J. Li and Y. Chen. *Computational partial differential equations using MATLAB*, volume 17. Chapman & Hall/CRC, 2009.

[78] T. C. Lieuwen, V. Yang, and F. K. Lu. *Combustion instabilities in gas turbine engines: operational experience, fundamental mechanisms and modeling*. American Institute of Aeronautics and Astronautics, 2005.

[79] J. Lilly. Finite-dimensional adaptive observers applied to distributed parameter systems. *IEEE Transactions on Automatic Control*, 38(3):469–474, 1993.

[80] J. L. Lions. *Optimal control of systems governed by partial differential equations*. Berlin, Springer-Verlag, 1971.

[81] X. Litrico and V. Fromion. Analytical approximation of open-channel flow for controller design. *Applied Mathematical Modelling*, 28(7):677–695, 2004.

[82] P. Liu, T. Seo, N. Beyor, K. Shin, J. Scherer, and R. Mathies. Integrated portable polymerase chain reaction-capillary electrophoresis microsystem for rapid forensic short tandem repeat typing. *Analytical Chemistry*, 79(5):1881–1889, 2007.

[83] W. Liu. Boundary feedback stabilization of an unstable heat equation. *SIAM Journal on Control and Optimization*, 42(3):1033 – 1043, 2004. Heat equations;Boundary control;Control law;Boundary feedback stabilization;.

[84] Y. Liu, A. and L. Lapidus. Observer theory for distributed-parameter systems. *International Journal of Systems Science*, 7(7):731–742, 1976.

[85] D. G. Luenberger. Observing the state of a linear system. *IEEE Transactions on Military Electronics*, 8(2):74–80, 1964.

[86] H. Mabuchi and N. Khaneja. Principles and applications of control in quantum systems. *International Journal of Robust and Nonlinear Control*, 15(15):647–667, 2005.

[87] J. Maciejowski. *Predictive Control: With Constraints*. Pearson Education. Prentice Hall PTR, 2002.

[88] L. Markus. Introduction to the theory of distributed control systems. *Distributed parameter control systems, Lecture Notes in Pure and Appl. Math*, 1991.

[89] K. Mattsson, M. Svärd, and M. Shoeybi. Stable and compact finite difference schemes. *Center for turbulence reserch annual report*, pages 211–222, 2006.

[90] H. McKean and V. Moll. *Elliptic Curves: Function Theory, Geometry, Arithmetic*. Cambridge University Press, 1999.

[91] R. J. Meagher, A. V. Hatch, R. F. Renzi, and A. K. Singh. An integrated microfluidic platform for sensitive and rapid detection of biological toxins. *Lab on a Chip*, 8(12):2046–2053, 2008.

[92] R. Miranda, I. Chairez, and J. Moreno. Observer design for a class of parabolic pde via sliding modes and backstepping. In *Variable Structure Systems (VSS), 2010 11th International Workshop on*, pages 215–220. IEEE, 2010.

[93] K. B. Mullis, H. A. Erlich, N. Arnheim, G. T. Horn, R. K. Saiki, and S. J. Scharf. Process for amplifying, detecting, and/or-cloning nucleic acid sequences, US Patent 4683195, 1987.

[94] K. B. Mullis et al. The unusual origin of the polymerase chain reaction. *Scientific American*, 262(4):56–61, 1990.

[95] F. B. Myers and L. P. Lee. Innovations in optical microfluidic technologies for point-of-care diagnostics. *Lab on a Chip*, 8(12):2015–2031, 2008.

[96] P. Ngatchou, M. Holl, C. Fisher, M. Saini, J. Dong, T. Ren, W. Pence, D. Cunningham, S. Moody, D. Donaldson, et al. A real-time pcr analyzer compatible with high-throughput automated processing of 2-μl reactions in glass capillaries. *IEEE Transactions on Automation Science and Engineering*, 3(2):141–151, 2006.

[97] J. Noh, S. Sung, M. Jeon, S. Kim, L. Lee, and S. Woo. In situ thermal diagnostics of the micro-PCR system using liquid crystals. *Sensors and Actuators A: Physical*, 122(2):196–202, 2005.

[98] M. Northrup, M. Ching, R. White, and R. Watson. DNA amplification with a microfabricated reaction chamber. *Transducers*, 93:924, 1993.

[99] Y. V. Orlov. Discontinuous unit feedback control of uncertain infinite-dimensional systems. *IEEE Transactions on Automatic Control*, 45(5):834–843, 2000.

[100] Y. V. Orlov and V. Utkin. Sliding mode control in indefinite-dimensional systems. *Automatica*, 23(6):753–757, 1987.

[101] W. Pratt. *Digital Image Processing: PIKS Scientific Inside: 4th (fourth) edition*. Wiley & Sons, Inc., 2007.

[102] L. Rade and B. Westergren. *Mathematics Handbook for Science and Engineering*. Springer, 2004.

[103] J. Rawlings and D. Mayne. *Model Predictive Control: Theory and Design*. Nob Hill Publishing, 2009.

[104] W. Ray. *Advanced process control*. McGraw-Hill Companies, 1981.

[105] J.-P. Richard. Time-delay systems: an overview of some recent advances and open problems. *Automatica*, 39(10):1667–1694, 2003.

[106] M. Roper, C. Easley, and J. Landers. Advances in polymerase chain reaction on microfluidic chips. *Analytical Chemistry*, 77(12):3887–3894, 2005.

[107] T. Seidman. Two results on exact boundary control of parabolic equations. *Applied Mathematics and Optimization*, 11(1):145–152, 1984.

[108] J. Shah, S. Sundaresan, J. Geist, D. Reyes, J. Booth, M. Rao, and M. Gaitan. Microwave dielectric heating of fluids in an integrated microfluidic device. *Journal of Micromechanics and Microengineering*, 17(11):2224–2230, 2007.

[109] A. Smyshlyaev and M. Krstić. Closed-form boundary state feedbacks for a class of 1-D partial integro-differential equations. *IEEE Transactions on Automatic Control*, 49(12):2185 – 2202, 2004.

[110] A. Smyshlyaev and M. Krstić. Backstepping observers for a class of parabolic PDEs. *Systems and Control Letters*, 54(7):613 – 625, 2005.

[111] A. Smyshlyaev and M. Krstić. *Adaptive control of parabolic PDEs*. Princeton University Press, 2010.

[112] C. Sozzi, E. Alessi, L. Boncagni, C. Galperti, C. Marchetto, S. Nowak, W. Bin, A. Botrugno, A. Bruschi, S. Cirant, et al. A real-time system for data acquisition, elaboration and actuator's control for magnetohydrodynamics instabilities in the ftu tokamak. In *the 51st IEEE Annual Conference on Decision and Control (CDC)*, pages 4353–4358. IEEE, 2012.

[113] E. Tadmor. A review of numerical methods for nonlinear partial differential equations. *Bulletin of the American Mathematical Society*, 49, 2012.

[114] Y. Tanaka, M. Slyadnev, A. Hibara, M. Tokeshi, and T. Kitamori. Non-contact photothermal control of enzyme reactions on a microchip by using a compact diode laser. *Journal of Chromatography A*, 894(1):45–51, 2000.

[115] Y. Wang, G. Haller, A. Banaszuk, and G. Tadmor. Closed-loop lagrangian separation control in a bluff body shear flow model. *Physics of Fluids*, 15:2251, 2003.

[116] J. West, B. Karamata, B. Lillis, J. P. Gleeson, J. Alderman, J. K. Collins, W. Lane, A. Mathewson, and H. Berney. Application of magnetohydrodynamic actuation to continuous flow chemistry. *Lab on a Chip*, 2(4):224–230, 2002.

[117] P. Wilding, M. Shoffner, and L. Kricka. PCR in a silicon microstructure. *Clin Chem*, 40(9):1815–8, 1994.

[118] I. Yaz, V. Bakke, and E. Yaz. Receding window observer and dynamic feedback control of discrete infinite dimensional systems. In *Proceedings of the 30th IEEE Conference on Decision and Control (CDC)*, pages 3031–3032. IEEE, 1991.

[119] D. Yoon, Y. Lee, Y. Lee, H. Cho, S. Sung, K. Oh, J. Cha, and G. Lim. Precise temperature control and rapid thermal cycling in a micromachined PCR chip. *Journal of Micromechanics and Microengineering*, 12:813–823, 2002.

[120] C. Zhang and D. Xing. Miniaturized PCR chips for nucleic acid amplification and analysis: latest advances and future trends. *Nucleic acids research*, 2007.

[121] Y. Zhang and P. Ozdemir. Microfluidic DNA amplification–A review. *Analytica Chimica Acta*, 638(2):115–125, 2009.